J. Webster (ed.), *Wiley Encyclopedia of Electrical and Electronics Engineering*

OPTOELECTRONIC DEVICES

Optoelectronic devices and applications cover a wide range of fields of interest in optical communication and computing. Photodetectors (PDs), optical sources, optical switches, optical waveguides, optical amplifiers, multiplexing, optical control of microwave devices, integrated optics, transmitters, receivers, and optical memory devices are some examples. In this article discussions will be given of all the above devices except optical sources such as lasers and LEDs, which have been included in some other articles.

The word *optoelectronic* stands for conversion of optical energy, which is the basic physical principle for PDs. With the advent of device fabrication technologies such as molecular beam epitaxy (*MBE*), metal–organic chemical vapor deposition (*MOCVD*), and metal–organic vapor phase epitaxy (*MOVPE*), optoelectronic devices have made much progress. In place of electron transport, photon transport can be utilized in system realizations with optoelectronic devices. The all–optical computer is no longer a dream and may be realized in the near future.

Photodetectors

Electron–hole pair generation in a PD occurs due to three processes:

(1) The intrisinic process, where electrons transit from the valence band of the semiconductor to the conduction band due to absorption of radiation. The semiconductors used for this process are both direct- and indirect-bandgap materials. In direct-bandgap semiconductors, where the valence band maximum and conduction band minimum lie on the same wave vector, the transition is easy. The photon energy for this type of transition process is equal to or greater than the bandgap energy (E_g) of the semiconductor (i.e., $hc/\lambda \geq E_g$, where h is the Planck's constant, c is the velocity of light, and λ is the wavelength of the radiation).
(2) The extrinsic process, where there are deep impurity and defect levels in the forbidden gap of the semiconductor and the transition of an electron takes place either from a deep level to the conduction band or from the valence band to an impurity level, leaving the hole behind. In this case the photon energy is less than the bandgap energy of the semiconductor.
(3) The transition between the subband energy levels in quantum wells, which is useful in far infrared regions of radiation spectra.

Figure 1 shows the three basic processes of photodetection.

In addition to electron–hole pair generation in a PD due to absorption of incident photons, there may be gain due to avalanche multiplication followed by carrier transport and interaction with the external circuit supplying the current. PDs, *p–n* junction diodes and avalanche photodiodes (*APDs*) are some common PDs that are well known from early days. In addition, recent technology has given us heterojunction photodiodes, as well as multilayer-structure APDs such as superlattice APDs, staircase APDs, graded-gap APDs, and channel-

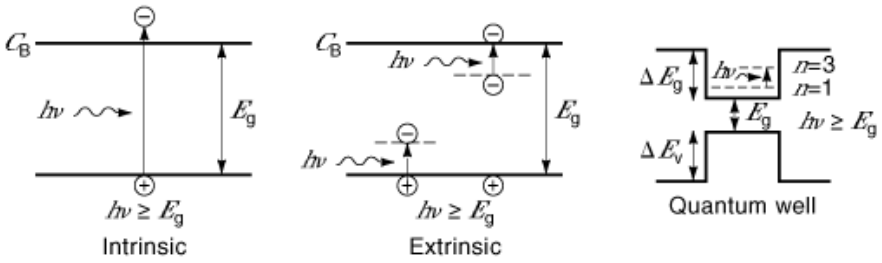

Fig. 1. Basic transition processes.

ing APDs, as low-noise, high-gain, large-bandwidth detectors. Other types include *DOVATT* (double velocity avalanche transit time) photodiodes and metal–semiconductor–metal (*MSM*) PDs. The multiple quantum well (*MQW*) PD is also an important addition to this class.

The PD parameters we need to study include the quantum efficiency, responsivity, signal-to-noise ratio, and noise equivalent power.

The quantum efficiency is defined as the number of electron–hole pairs generated per photon incident on the photodetector and is expressed as

$$\eta = \frac{I_P/q}{P_i/h\nu} = I_P h\nu/q P_i$$

where I_P is the photocurrent reaching the external circuit, P_i is the incident optical power on the semiconductor surface, and ν is the frequency of the lightwave. η also depends on the absorption coefficient of the material, α, which is defined as the reciprocal of the distance over which the incident radiation is attenuated by a factor e.

The responsivity of the detector is defined as the detector external current or output voltage across a load per unit input power, or

$$R_p = I_p/P_i = \eta q/h\nu \qquad \text{(A/W)}$$

and is proportional to wavelength of radiation.

The signal-to-noise ratio (SNR) is an important figure of merit of a detecting system. The higher the SNR, the better is the receiver system. The SNR for an optical receiver is given by

$$\text{SNR} = \frac{\text{signal power}}{\text{noise power}} = \frac{\langle i_p \rangle^2}{\langle I_{n1} \rangle^2 + \langle i_{n2} \rangle^2}$$

where $\langle i_p \rangle^2$ is the mean squared signal current generated by the incident photons, $\langle l_{nl} \rangle^2$ is the mean squared noise current due to shot noise as a result of absorption of photons, and $\langle i_{n2} \rangle^2$ is the mean squared noise current due to Johnson noise, which is present due to resistive elements. In the case of an APD this may also include the multiplication noise. The expressions for these parameters depend on the type of PD used in the photoreceiver.

The noise equivalent power (NEP) (W/Hz$^{1/2}$) is the minimum detectable power for which SNR = 1. It is the optical power incident on the PD required to produce a signal current equal to $\sqrt{\langle i_{n1} \rangle^2 + \langle i_{n2} \rangle^2}$, divided by the square root of the frequency.

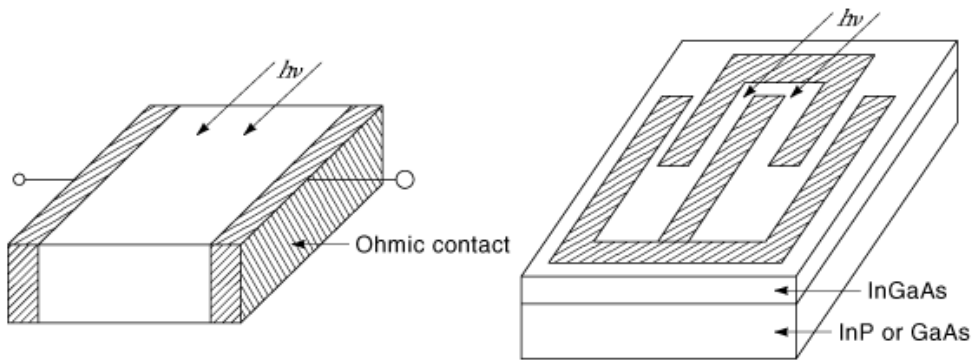

Fig. 2. Photoconductor types.

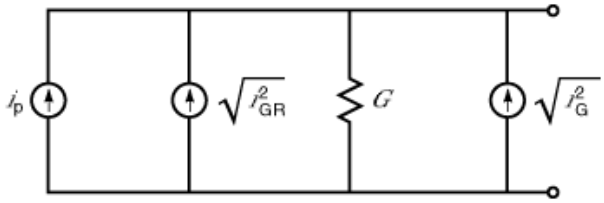

Fig. 3. Noise equivalent circuit of photoconductors.

The speed of response of the PD depends on the time constants (both rise time and fall time) of the detector, which in turn depend on three factors: carrier transport in the PD, namely, diffusion of carriers; drift in the depletion region; and the capacitance of the depletion region. The junction of the device should be shallow to minimize the diffusion effect. In choosing the depletion width, a tradeoff should be made between the minimization of transit time effects and of the RC time constant, where R is the external circuit resistance and C is the depletion layer capacitance.

Photoconductors. A photoconductor is the simplest form of radiation detector, It may consist of a semiconductor slab with an ohmic contact at each end, or there may be interdigitated metallic contacts on the top of a epitaxially grown active layer on a high-resistivity substrate. The thickness of the absorbing region should be large enough to absorb sufficient radiation, but small enough for low noise current. The electron–hole pairs are generated either by intrinsic or by extrinsic processes. The two forms of photoconductors are shown in Fig. 2.

The photocurrtent gain of the photoconductor is given by

$$G = \frac{I_p}{I_{ph}} = \frac{\tau}{t_r}$$

where I_p is the photocurrent flowing between the electrodes, I_{ph} is the primary photocurrent, τ is the carrier lifetime, and t_r is the carrier transit time given by L/v_d, L being the length between two contacts and v_d the carrier drift velocity. The noise equivalent circuit of a photoconductor is shown in Fig. 3, where i_p is the rms signal current, i_{GR} is the generation–recombination current, and i_G is the thermal noise current resulting from

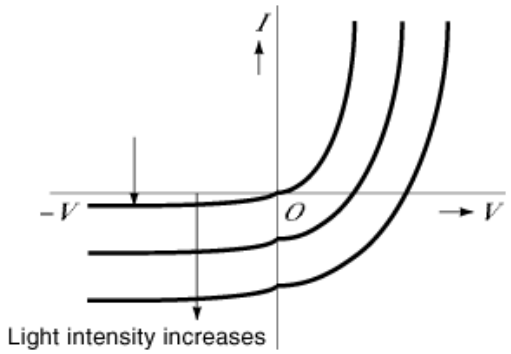

Fig. 4. I–V characteristics of a photodiode.

the conductance G. The SNR is calculated as

$$\begin{aligned} \text{SNR} &= \frac{i_{\text{p}}^2}{i_{\text{GR}}^2 + i_G^2} \\ &= \frac{\eta P_1^2}{8BP_0h\nu}\left(1 + \frac{kTt_{\text{r}}}{q\tau}(1+\omega^2\tau^2)\frac{G}{I_0}\right) \end{aligned}$$

where P_1 is the amplitude of the modulated optical power, P_0 is the dc component of the optical power, B is the bandwidth, I_0 is the dc output current, k is Boltzmann's constant, T is the absolute temperature, and ω is the angular frequency. The NEP is obtained by putting SNR = 1 for unity bandwidth. The detectivity is defined as

$$D^* = \frac{A^{1/2}B^{1/2}}{\text{NEP}} \qquad (\text{m} \cdot \text{Hz}^{1/2}/\text{W})$$

where A is the photoconductor area. Photoconductors made of CdS, PbS, InSb, n-doped Ge, and p-doped Si are used mainly in the infrared region.

Photodiodes. For low-level detection at microwave frequencies a photodiode provides fast response and high SNR. The photodiode is reverse-biased. The high field in the depletion region separates the electrons and holes generated by optical absorption. The depletion is optimized for high speed of response and high quantum efficiency. Typical I–V characteristics of a photodiode are shown in Fig. 4. They indicate that the current of a photodiode increases with light intensity in both reverse and forward bias conditions.

Classes of photodiodes include p–n junction, p–i–n, avalanche, metal–semiconductor (Schottky barrier), MSM, heterojunction, DOVATT, multilayer-structure, and MQW photodiodes. Since the absorption coefficient α is an important parameter for the photodiode characterization, Fig. 5(a, b) show plots of α against wavelength λ in the different ultraviolet to infrared regions. The plots show that α is a strong function of wavelength for a particular semiconductor and the wavelength range over which appreciable photocurrent can be generated is limited.

p–i–n PHOTODIODE. The p–i–n photodiode has an intrinsic layer between a p and an n semiconductor layer, and the width of the i layer can be tailored to achieve fast response and large quantum efficiency. The schematic structure and the energy band diagram of p–i–n diodes are shown in Fig. 6. The surface p-layer thickness is small compared to $1/\alpha$, so that the absorption in the p layer is negligible and most of the

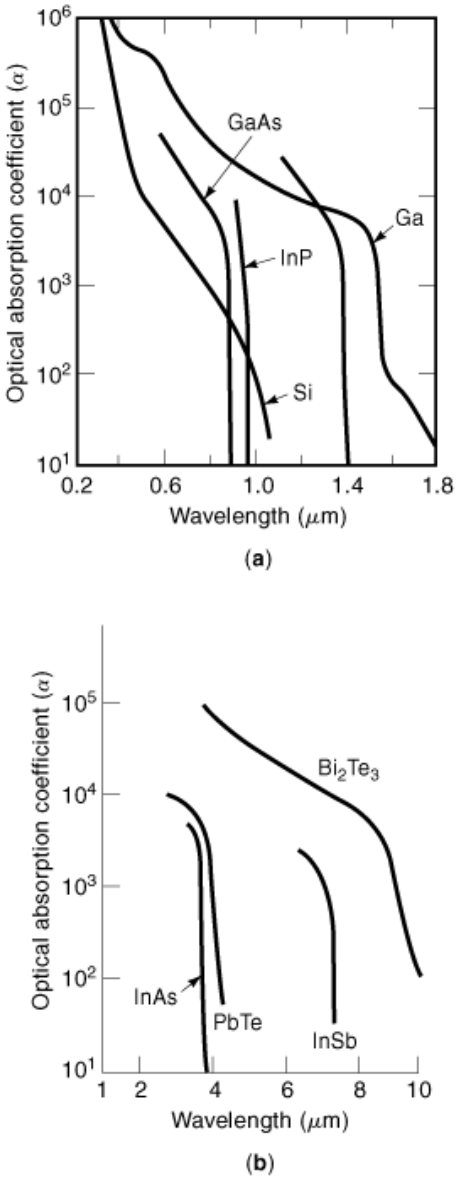

Fig. 5. Optical absorption coefficients of semiconductors.

absorption takes place in the reverse-biased i depletion region. The photoexcitation is provided either through a mesa-etched opening at the top contact or through an etched hole in the substrate, as shown in Fig. 6.

The total current due to electron–hole pair generation in the device is due to both drift and diffusion processes, and is given by

$$J_t = J_{dr} + J_{diff}$$

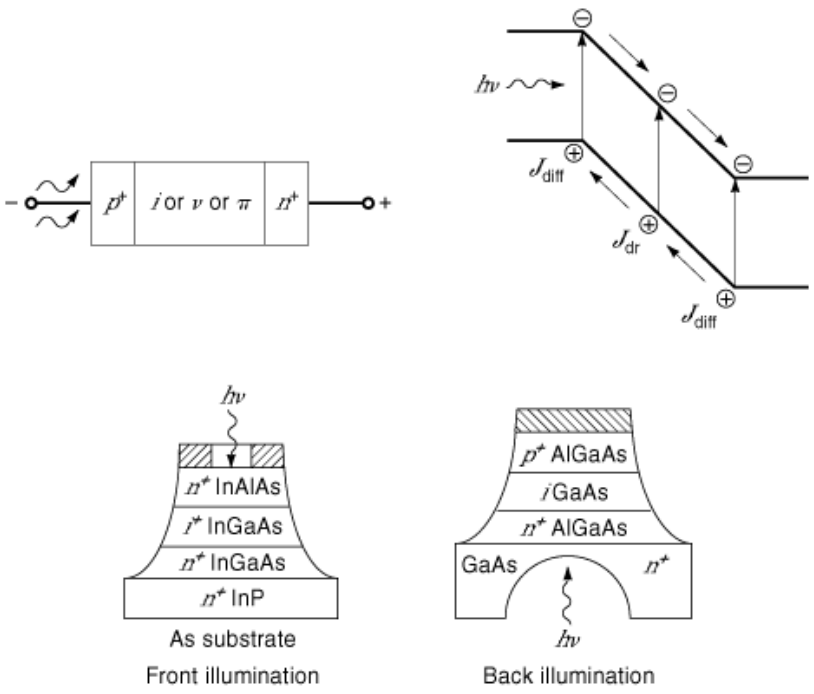

Fig. 6. *p–i–n* photodetector.

where J_{dr} is the drift current density within the depletion region and J_{diff} is the optimal diffusion current density for carriers generated outside the depletion region. The transit time t_{r} of carriers through the depletion region is taken as

$$t_{\mathrm{r}} = 1/2(\text{modulation period})$$

and we set

$$t_{\mathrm{r}} = \tau_{RC}$$

τ_{RC} being the RC time constant of the *p–i–n* diode. The volume generation rate of electron–hole pairs is expressed as

$$G(x) = \phi \propto \exp(- \propto x)$$

where ϕ is the incident photon flux density per unit area and time, given by

$$\phi = P_{\mathrm{i}}(1 - R)/Ah\nu,$$

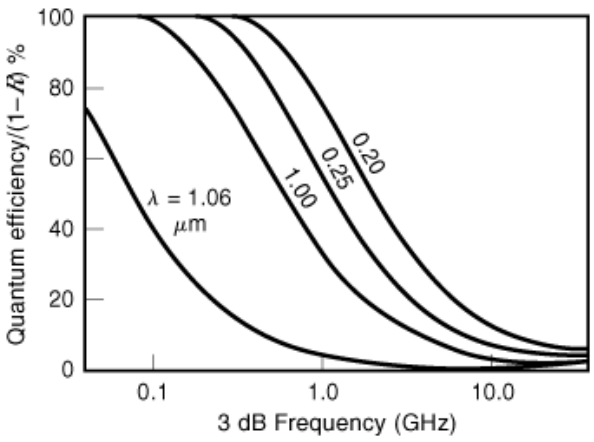

Fig. 7. Internal quantum efficiency as a function of 3 dB frequency and depletion width.

in which R is the reflection coefficient at the surface and A is the device area. The quantum efficiency and the cutoff frequency of the p–i–n diode are expressed as

$$\eta = \frac{\mathcal{J}_t/q}{P_i/Ah\nu} = (1-R)\left(1 - \frac{\exp(-\propto w)}{1+\propto L_p}\right)$$

and

$$f_{3\text{ dB}} \approx \frac{0.4v_s}{w} \approx 0.4\alpha v_s$$

where $w = 1.0/\alpha$ is the depletion layer width and $L_p = \sqrt{D_p\tau_p}$, D_p and τ_p being the diffusion coefficient and lifetime for holes, and v_s is the scattering-limited velocity of carriers.

A plot of the internal quantum efficiency $\eta/(1-R)$ as a function of 3 dB frequency and depletion width for a Si p–i–n photodiode is shown in Fig. 7. The internal quantum efficiency decreases with increasing 3 dB frequency, and at a particular 3 dB frequency it increases with decrease in λ.

Figure 8 shows the frequency response characteristics for an InGaAs p–i–n photodiode as a function of transit angle θ_r (ωt_r) for several depletion widths. The response decreases with increasing transit angle and increases with λ.

The noise equivalent circuit of a p–i–n photodiode is shown in Fig. 9. In this circuit i_{ph} is the ac photocurrent, i_s is the shot noise current, i_J is the Johnson noise current resulting from the resistances, C_j is the depletion capacitance, R_D is the shunt resistance, R_s is the series resistance, R_L is the load resistance, and R_i is the input resistance of the next preamplifier stage of the receiver system. The ac (rms) photocurrent is expressed as

$$i_{ph} = q\eta P_i/\sqrt{2h\nu}$$

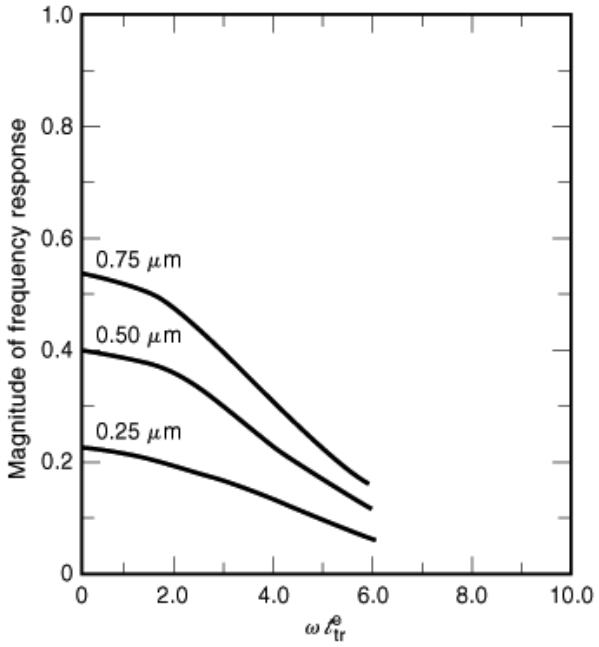

Fig. 8. Frequency response for three depletion widths.

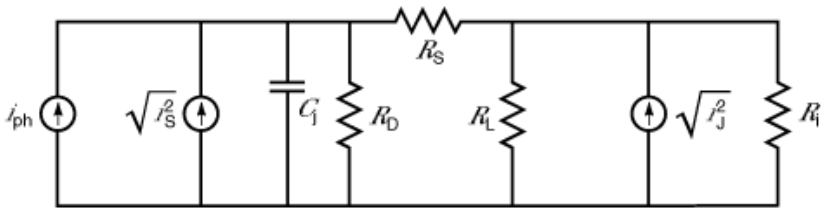

Fig. 9. Noise equivalent circuit of *p–i–n* photodiode.

where $P_i/\sqrt{2}$ is the rms incident optical power. The shot noise current is given by

$$I_S^2 = 2q(I_{ph} + I_B + I_D)/B$$

where I_B is the current due to background radiation, I_D is the thermally generated current (dark current), and B is the bandwidth. The Johnson noise current is given by

$$I_J^2 = 4kTB/R_{eq}$$

where

$$R_{eq} = \left(\frac{1}{R_D} + \frac{1}{R_L} + \frac{1}{R_i}\right)^{-1}$$

R_s is usually very small. The SNR and NEP of the device are given by

$$\text{SNR} = \frac{{}^{1}/_{2}(q\eta P_i/h\nu)^2}{2q(I_{ph} + I_B + I_D)B + 4kTB/R_{eq}}$$

and

$$\text{NEP} = h\nu/q\eta\left(2q(I_{ph} + I_B + I_D) + \frac{4kT}{R_{eq}}\right)^{1/2} \qquad (\text{W/Hz}^{1/2})$$

These equations show that the device is more sensitive to radiation if η and R_{eq} are large and I_B and I_D small.

Avalanche Photodiode. The APD has internal gain due to multiplication. It operates under large reverse bias close to its avalanche breakdown voltage. The simultaneous effects of impact ionization and the transit time of carriers make the device highly sensitive to very low-level radiation intensity, and it is used very effectively in optical communication systems. However, the noise figure of the device is significantly larger than that of other devices.

The time-dependent equations for an APD, governing the generation of carriers (due to both photoabsorption and impact ionization) and the flow of carriers, are

$$\frac{\partial n(x,t)}{\partial t} = g_{op}(x,t) + \alpha_n(x)n(x,t)v_n + \alpha_p(x)p(x,t)v_p + \frac{1}{q}\frac{\partial J_n(x,t)}{\partial x}$$

for electrons, and

$$\frac{\partial p(x,t)}{\partial t} = g_{op}(x,t) + \alpha_n(x)n(x,t)v_n + \alpha_p(x)p(x,t)v_p - \frac{1}{q}\frac{\partial J_p(x,t)}{\partial x}$$

for holes, where α_n and α_p are the ionization rates of carriers, v_n and v_p are the drift velocities, and n and p are the concentrations for electrons and holes respectively. The current densities, which are mainly due to drift, are given by

$$\begin{aligned} J_n(x,t) &= qn(x,t)v_n \\ J_p(x,t) &= qp(x,t)v_p \end{aligned}$$

Since the applied electric field is large, v_n and v_p are assumed to be same as their scattering-limited values. The optical generation rate g_{op} is expressed as

$$g_{op}(x,t) = \alpha\phi\left(t - \frac{x}{c}\right)\exp(-\alpha x)$$

c being the velocity of light.

Both the ionization rates and the drift velocities are functions of applied electric field. Thus the equations are solved numerically for accurate modeling. The experimental ionization rates α_n and α_p can be best fitted

Table 1: Ionization Constants for Different Materials at Room Temperature

	Electrons		Holes		
Semiconductor	$A_n(\text{cm}^{-1})$	$B_n(\text{V}\cdot\text{cm}^{-1})$	$A_p(\text{cm}^{-1})$	$B_p(\text{V}\cdot\text{cm}^{-1})$	m
Si	3.8×10^6	1.75×10^6	2.25×10^7	3.25×10^6	1
Ge	1.55×10^7	1.56×10^6	1.0×10^7	1.28×10^6	1
GaAs	3.5×10^5	6.85×10^5	3.5×10^5	6.85×10^5	2
GaP	4.0×10^5	1.18×10^6	4.0×10^5	1.18×10^6	2

with the following expressions over a wide range of electric field:

$$\alpha_{n,p} = A_{n,p} \exp\left(-\frac{B_{n,p}}{E}\right)^m$$

where A, B, and m are constants that depend on the nature of the material and the temperature. Table 1 shows the values of A, B, and m for different materials at room temperature.

In Si, $\alpha_n = 100\alpha_p$; in Ge, $\alpha_n = 5.0\alpha_p$; and in GaAs, $\alpha_n \approx \alpha_p$. The ionization rates are also related to the multiplication factors M_n and M_p for electrons and holes. If J_i is the total current density injected by either electrons or holes in an APD and J_o is the output current density, then the multiplication factor is defined as

$$M_{n,p} = \frac{J_{on,p}}{J_{in,p}}$$

The common APDs are p–i–n and p^+–n–n^+. The frequency response characteristics of a Si APD are shown in Fig. 10. The structure of the diode can be changed from Read type (p^+–n–i–n^+) to p–i–n by varying the avalanche- and drift-layer widths. The gain increases and bandwidth decreases when the avalanche-layer width increases and the drift-layer width decreases. The gain–bandwidth product is higher for a Read-type APD. The dark current in an APD arises from leakage current, tunneling current, and generation–recombination in the depletion region. Incorporation of a grading (which is most common in Si APDs) can reduce the excessive leakage current from the junction edges. The gain–bandwidth product of an APD can be higher than 100 GHz, enabling the device to detect optical radiation modulated at microwave frequencies.

The Ge APDs is useful in the 1 μm to 1.6 μm wavelength range with high quantum efficiency. However it has a large noise factor, as the electron and hole ionization rates are comparable. A typical Ge APD with guard-ring structure (n^+–p–n^+) shows a dark current 3×10^{-4} A/cm^2 with quantum efficiency 80%. Si lo–hi–lo and hi–lo APDs have also been fabricated, which are similar to lo–hi–lo IMPATT diodes (Fig. 10). The devices exhibit 90% quantum efficiency at 0.9 μm wavelength with comparatively low noise factor for high multiplication gain.

The materials to be chosen for an APD depend on the application. The narrow-bandgap II–IV, III–V, and IV–VI compound semiconductors have become increasingly important for low-noise, high-speed APDs for long-wavelength communication. However, the small bandgap of these devices leads to significant tunneling current. The tunneling current can be eliminated with a structure that provides separate regions for multiplication and absorption: the so-called *SAM* APD (Fig. 11). The heterostructure APD (*HAPD*) has also been investigated for optical fiber communication systems. InP/InGaAsP APDs are useful in the 1.0 μm to 1.6 μm

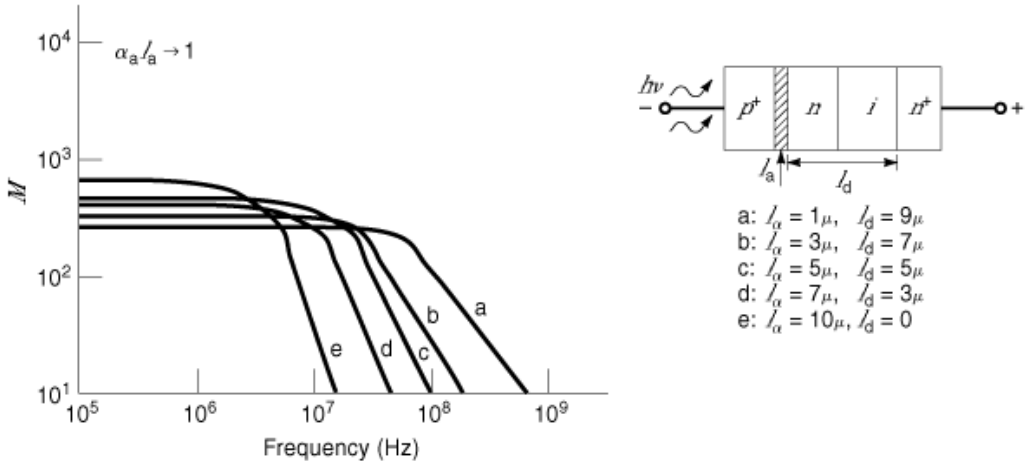

Fig. 10. Multiplication gain versus frequency of a Si APD for different avalanche-layer widths l_a and drift-layer widths l_d.

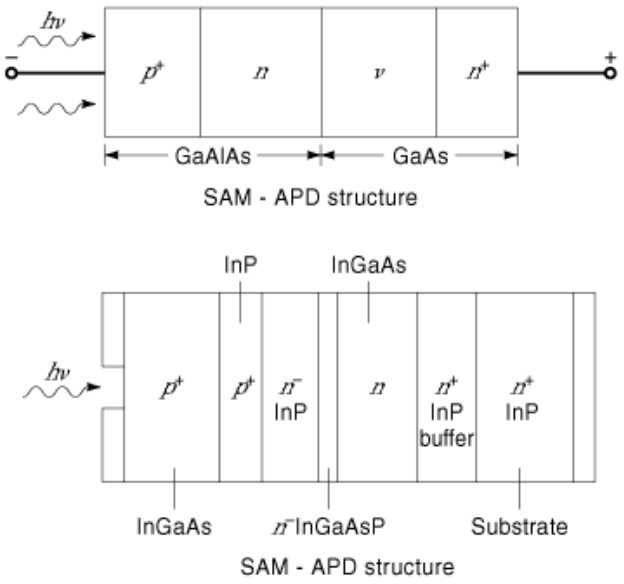

Fig. 11. SAM-APD and SAGM-APD structures.

wavelength range. InAs/InAsSb APDs can be used in the near infrared and far infrared regions. SAM APDs may give longer response times than desired due to accumulation of holes at the valence band discontinuity. This is removed in a separate-absorption graded-multiplication (*SAGM*) APD (Fig. 11). Gain–bandwidth products of more than 100 GHz can be obtained in SAM APDs. Another structure, called the separate-absorption graded-charge multiplication (*SAGCM*) APD, has an additional highly doped narrow region, which decouples the multiplication layer. Thus the thickness and concentration of the layer can be adjusted independently.

DOVATT Photodiode. The DOVATT diode is a heterostructure device useful for generation of microwave power. The structure is p^+–n_1–n_2–n^+ and is shown in Fig 12. The p^+–n_1 is made of lower-bandgap material, the

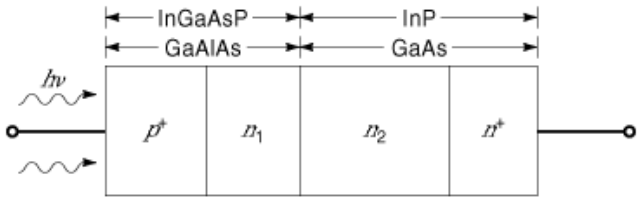

Fig. 12. Schematic structure of a DOVATT photodiode.

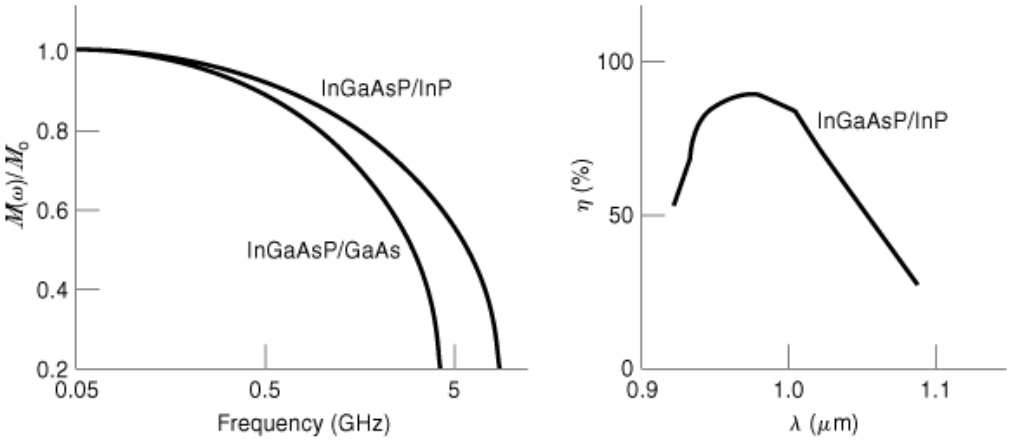

Fig. 13. Normalized gain versus frequency and quantum efficiency versus wavelength for a DOVATT photodiode.

n_2–n^+ is made of higher-bandgap material, and the two are lattice-matched to each other. The materials that have been studied are InGaAsP/InP, InGaAs/GaAs, and InSbAs/InAs. The frequency response characteristics and the quantum efficiency of these devices are shown in Fig. 13. The gain–bandwidth product is well above 100 GHz, and the quantum efficiency is around 75% near 1 μm wavelength for an InP/$In_{0.7}Ga_{0.3}As_{0.64}P_{0.36}$ DOVATT photodiode. For InAs/$InAs_{0.88}Sb_{0.12}$ the corresponding values are 20 GHz and 75% at 3 μm wavelength.

Superlattice Avalanche Photodiode. The large multiplication noise in the APD is an important disadvantage for its use as a detector. This is because in most compound semiconductors $\alpha_n \approx \alpha_p$, resulting a positive feedback effect due to holes. Therefore it is necessary to devise a structure yielding a large ratio α_n/α_p so that only ionization by electrons is favored and not that by holes. This significantly reduces the noise of the device. Using the technique of bandgap engineering (*BGE*), it is possible to radically modify the conventional energy band (*EB*) diagram of a *p*–*n* junction and tailor the high-field transport to a desired application. Many new device concepts have emerged from this new approach. They are basically heterostructures in the intrisinic region of a p^+–*i*–n^+ APD. Alternate layers of width 260 Å to 500 Å, made of lattice-matched higher-bandgap and lower-bandgap materials, are grown epitaxially by MBE or MOCVD techniques. Around 50 or more layers are formed, depending on α_n/α_p. Some of the devices are:

(1) The graded-gap APD, which exploits the difference between the ionization energies and quasistatic fields for electrons and holes in graded-gap materials (in composition).

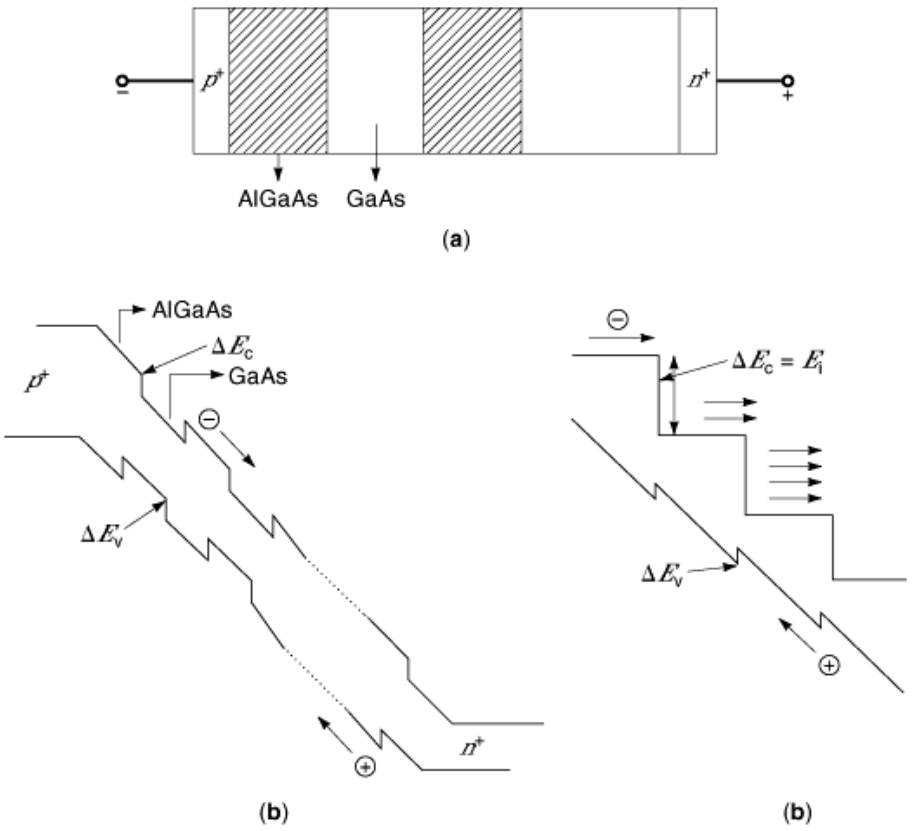

Fig. 14. Typical multilayer heterostructures and EB diagrams: (a) multilayer heterostructure; (b) EBs for superlattice (c) EBs for staircase.

(2) The superlattice and the staircase APD, in which large differences in ionization energies for electrons and holes are created by the asymmetry between conduction and valence band discontinuities in III–V heterojunctions.

(3) The channeling APD, using special separation of electrons and holes in materials of different bandgaps via p–n–p–n structures to enhance α_n/α_p.

The structure and the EB diagram of an $Al_xGa_{1-x}As/GaAs$ superlattice APD are shown in Fig. 14. It consists of a depletion region made up of alternate low-doped layers of $Al_xGa_{1-x}As$ and GaAs sandwiched between p^+ and n^+ regions. A hot electron accelerating in an $Al_xGa_{1-x}As$ layer, when it enters a GaAs layer, gains an energy equal to the conduction band (CB) edge discontinuity ΔE_c. So the electron finds an ionization threshold energy E_i in GaAs that is less by ΔE_c ($E_i = 1.5$ eV) than in the bulk ($E_i = 2.0$ eV). This results in a large increase in effective α_n. That is not so in the case of holes, as the valence band (VB) edge discontinuity $\Delta E_v << \Delta E_c$. Thus for 50 layers, α_n/α_p can be enhanced to 8. This is also verified experimentally. Typical frequency response characteristics are shown in Fig. 15; the gain–bandwidth product GBW is typically 75 GHz at a multiplication gain of 100. GBW increases with the increase in multiplication factor.

A staircase APD is a solid-state equivalent of a photomultiplier tube, which detects optical signals noiselessly. This is because the CB edge discontinuity $\Delta E_c \approx E_i$ (the ionization threshold energy). So when an

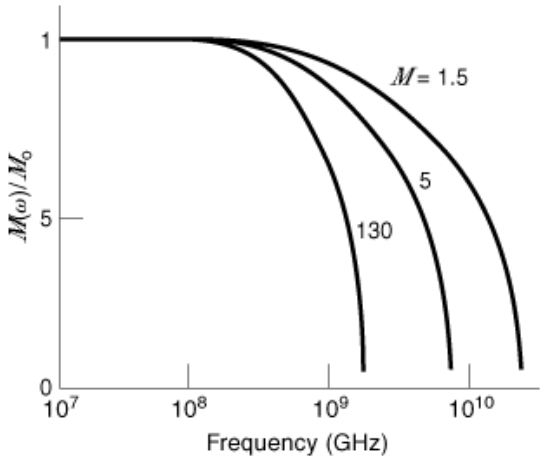

Fig. 15. Normalized gain versus frequency for GaAlAs/GaAs superlattice APD.

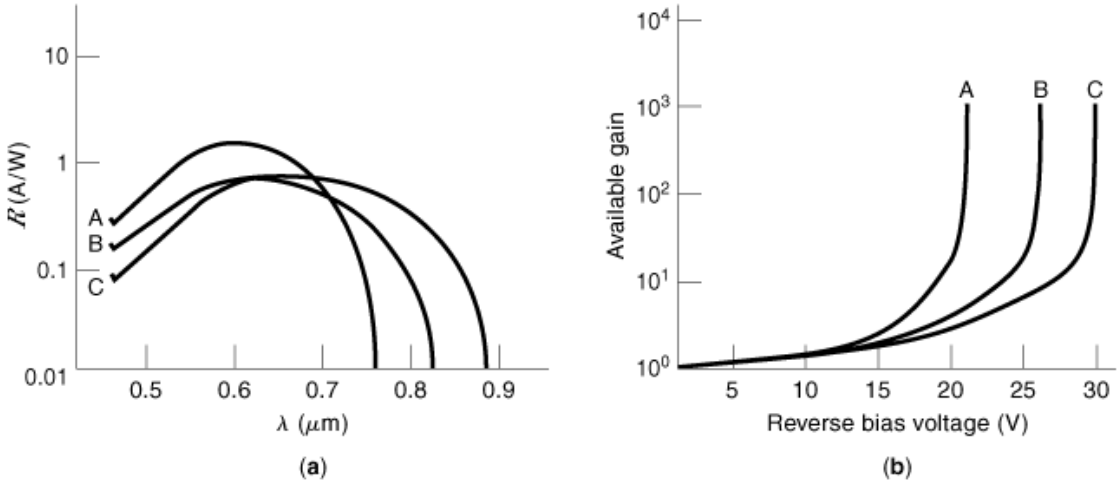

Fig. 16. Typical responsivity and available gain for a GaAs/GaAlAs superlattice photodetector.

electron drops from higher-bandgap to lower-bandgap material, it ionizes without taking further energy from the field. In such devices α_n/α_p more than 100 has been achieved, leading to a gain of more than 1000.

When the layer thickness is small (100 Å or less), enhancement of α is still possible. The superlattice (*SL*) APD also provides tunability of the spectral response. SL APDs with variable size of wells and barriers, typically with 20 to 30 periods, made of GaAs/AlGaAs have the responsivity and gain shown in Fig. 16 (a, b). The plots have been made for three different combinations of layer widths. They indicate that responsivity changes with λ for varyous layer widths and large gain are possible in APDs.

The multilayer heterojunction photodiode is also capable of detecting and demultiplexing two wavelength bands simultaneously.

Noise in Avalanche Photodiodes. The main source of noise in an APD is the multiplication process, which is statistical in nature. When both electrons and holes are responsible for multiplication, the mean squared

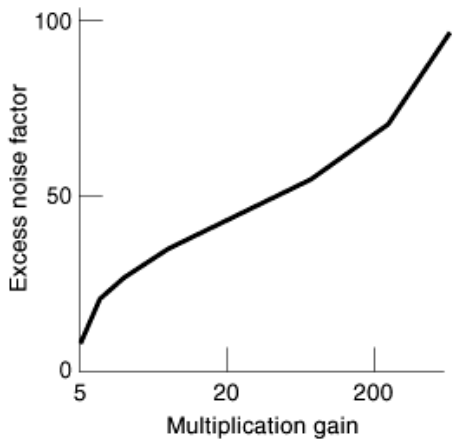

Fig. 17. Excess noise factor versus multiplication gain of the superlattice APD.

avalanche noise current is given by

$$\begin{aligned}\langle i_{ava}^2 \rangle &= \frac{2qI_{ps}M_p^3 B}{1+\omega^2 M^2\tau^2}\left(1+\frac{(1-K)(M_p-1)^2}{KM^2{}_p}\right)+\frac{2qI_{ns}M_n^3 B}{1+\omega^2 M^2\tau^2}\\ &\quad\left(1+\frac{(1-K)(M_n-1)^2}{KM_n^2}\right)\\ &\quad+\frac{2qAB}{1+\omega^2 M^2\tau^2}\\ &\quad\left(2\int_0^L g(x)M(x)^2\,dx+\frac{KM_n^2-M_p^2}{1-K}\int_0^L g(x)M(x)dx\right)\end{aligned}$$

where $K=\alpha_p/\alpha_n$, $M=I/I_s$ is the dc multiplication factor (I and I_s being the output current and the saturation current), τ is the intrinsic time, M_n and M_p are the multiplication factors for electrons and holes, $g(x)$ is the volume generation rate due to optical absorption at any point x, B is the bandwidth, and A is the junction area.

The excess noise factor $F(M)$ is the factor by which the noise exceeds that of an ideal current multiplier. It depends on the nature of the primary excitation (electron injection, hole injection, or mixed injection) and on the junction profile. When the avalanching is initiated by the most highly ionizing carriers, the excess noise factor is given by (Fig. 17)

$$F(M)=M\left|1-(1-K)\left(\frac{M-1}{M}\right)^2\right|$$

It increases with M.

The other noise factors, such as shot noise and Johnson noise, are same as in the p–i–n diode except that the multiplication factors M and $F(M)$ will be involved.

The vertical structure and the need for a complicated material system make the APD difficult to integrate monolithically with a preamplifier. Moreover, APDs are very sensitive to temperature fluctuation and are

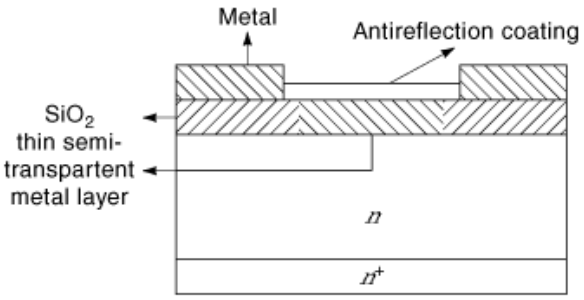

Fig. 18. Metal–semiconductor photodiode.

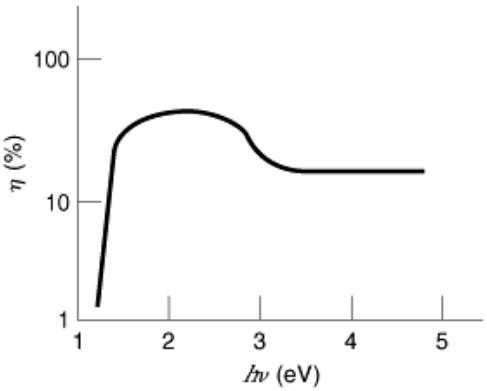

Fig. 19. The quantum efficiency of a Au–Si photodiode.

not very attractive for photonic communication, due to the requirement of a high, precisely temperature-compensated reverse bias voltage.

Metal–Semiconductor (Schottky Barrier) Photodiode. The metal–semiconductor photodiode is a majority carrier device and has large efficiency and bandwidth. It has a mesa-shaped configuration as shown in Fig. 18. The metal film is very thin ($\approx$ 100 Å to 300 Å), and an antireflection coating is used. The most efficient mode of operation of the diode is under the conditions $h\nu > E_g$ and $V < V_B$, the avalanche breakdown voltage. With a transparent or semitransparent metal region, the photons are absorbed in the semiconductor region, and the excess electron–hole pairs generated move in opposite directions and are collected at the terminals. This photodiode is useful in the visible and ultraviolet wavelength range. The quantum efficiency of a Au–*n*-Si Schottky photodiode is shown in Fig. 19 with 107 Å Au and $N_D = 8 \times 10^{21}$ m^{-3}. The quantum efficiency is almost constant for impurity concentrations varying from 10^{21} m^{-3} to 10^{23} m^{-3}.

Metal–Semiconductor–Metal Photodetector. For monolithic integration, the MSM PD is much more attractive than the conventional *p–i–n* PD or APD, due to its process compatibility with FET-based technology. MSM PDs can be realized for both short and long wavelengths with small capacitance and high response speed.

An MSM PD consists of two back-to-back interdigital Schottky barrier contacts on a low-doped semiconductor (Fig. 20). When the radiation falls on the photoactive area (interdigital area), electron–hole pairs are generated, which move preferentially in opposite directions with drift velocity due to the external voltage. The symmetric structure of the device allows the electrical signal to be reversed by reversing the external voltage.

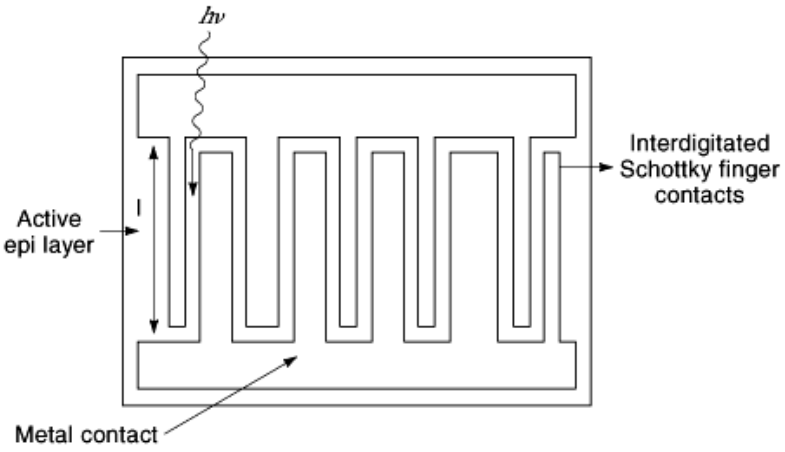

Fig. 20. MSM photodetector structure.

The dark current of the MSM PD is mainly due to thermionic emission of electrons under reverse bias given by

$$J_{\mathrm{d}} = A_n^* T^2 \exp\left(\frac{-q(\phi_{\mathrm{B}n} - \Delta\phi_{\mathrm{B}n})}{kT}\right)$$

where $A*_n$ is the Richardson constant, T is absolute temperature, $\phi_{\mathrm{B}n}$ is the barrier height of the metal–semiconductor junction, and $\Delta\phi_{\mathrm{B}n}$ is due to Schottky lowering.

However, when the conduction band at the anode becomes flat, thermionic emission of holes from the anode also becomes important. The dark current is then written as

$$J_{\mathrm{d}} = A_n^* T^2 \exp\left(\frac{-q(\phi_{\mathrm{B}n} - \Delta\phi_{\mathrm{B}n})}{kT}\right) + A_p^* T^2 \exp\left(\frac{-q(\phi_{\mathrm{B}p} - \Delta\phi_{\mathrm{B}p})]}{kT}\right)$$

The subscript p stands for holes. The flat-band voltage for the Schottky contact, ignoring the two-dimensional effect, is

$$V_{\mathrm{FB}} = \frac{qN_{\mathrm{D}}L^2}{2\varepsilon_{\mathrm{s}}}$$

where L is the length of the MSM junction. The dark current for a semi-insulating GaAs MSM PD is calculated using the simple relation

$$I_{\mathrm{D}} = qn_{\mathrm{i}}sv_{\mathrm{s}}$$

where s is the cross-sectional area and v_{s} is the saturated carrier velocity.

The capacitance of a MSM PD is due to the electrostatic field around the alternately charged parallel metal fingers. It has been calculated by conformal mapping and is given by

$$C = C_0(N-1)L, \qquad \text{where} \qquad C_0 = \varepsilon_0(1+\varepsilon_r)k/k'$$

and L is the length of MSM finger. In this,

$$k = \int_0^{\pi/2} \frac{d\phi}{\sqrt{1-k_F^2\sin^2\phi}}, \qquad \text{where} \qquad k_F = \tan^2\left(\frac{\pi}{4}\frac{L_G}{L_G+L_E}\right)$$

and

$$k' \int_0^{\pi/2} \frac{d\phi}{\sqrt{1-k_F'^2\sin^2\phi}}, \qquad \text{where} \qquad k_F' = \sqrt{1-k_F^2}$$

L_E is the finger width, and L_G is the finger separation. This formula, however, does not take account of the capacitance due to bonding pads and other components.

The photocurrent of a MSM PD is given by

$$I_{ph} = \eta\frac{4\eta_r}{(\eta_r+1)^2}\frac{L_G}{L_G+L_E}I_0$$

I_0 being the primary photocurrent given by $I_0 = qP_{opt}/h\nu$, η_r the reflection coefficient, and η the quantum efficiency.

The dark current, the photocurrent, the responsivity, and the quantum efficiency of a GaAs MSM PD are shown in Fig. 21. The dark current saturates at higher bias voltage and changes with the contacting metals. The photocurrent increases linearly with optical power density. The responsivity first increases with incident optical power density and becomes constant at higher power density. The quantum efficiency also increases with bias voltage and attains a constant value at high bias voltage (> 2 V).

The equivalent circuit of a MSM PD is shown in Fig. 22, where C_p is the parasitic capacitance, and C_{pd} is the diode capacitance. A bandwidth 50 GHz and above can be obtained at 1.3 μm to 1.6 μm. $In_{0.53}Ga_{0.47}As$ epitaxially grown on semiinsulating (SI) GaAs can be used. A thin surface layer of $In_{0.52}Al_{0.48}As$ is used to enhance the Schottky barrier.

Long-Wavelength Detection

For far infrared (5 μm to 20 μm) detection, small-bandgap materials in the III–V and II–VI groups of compounds are useful. The technique is to use a junction diode with such materials, where band-to-band transition is important. Among these materials, the ternary compounds InAsSb and HgCdTe have been found useful so far. However, the technological process steps for these materials are difficult and require the use of strained semiconductors due to lack of lattice-matched materials. A detectivity $\sim 10^8$ m·Hz$^{1/2}$/W has been obtained with these materials. However, due to their small bandgap, such detectors have large dark current and have to be operated at low temperature.

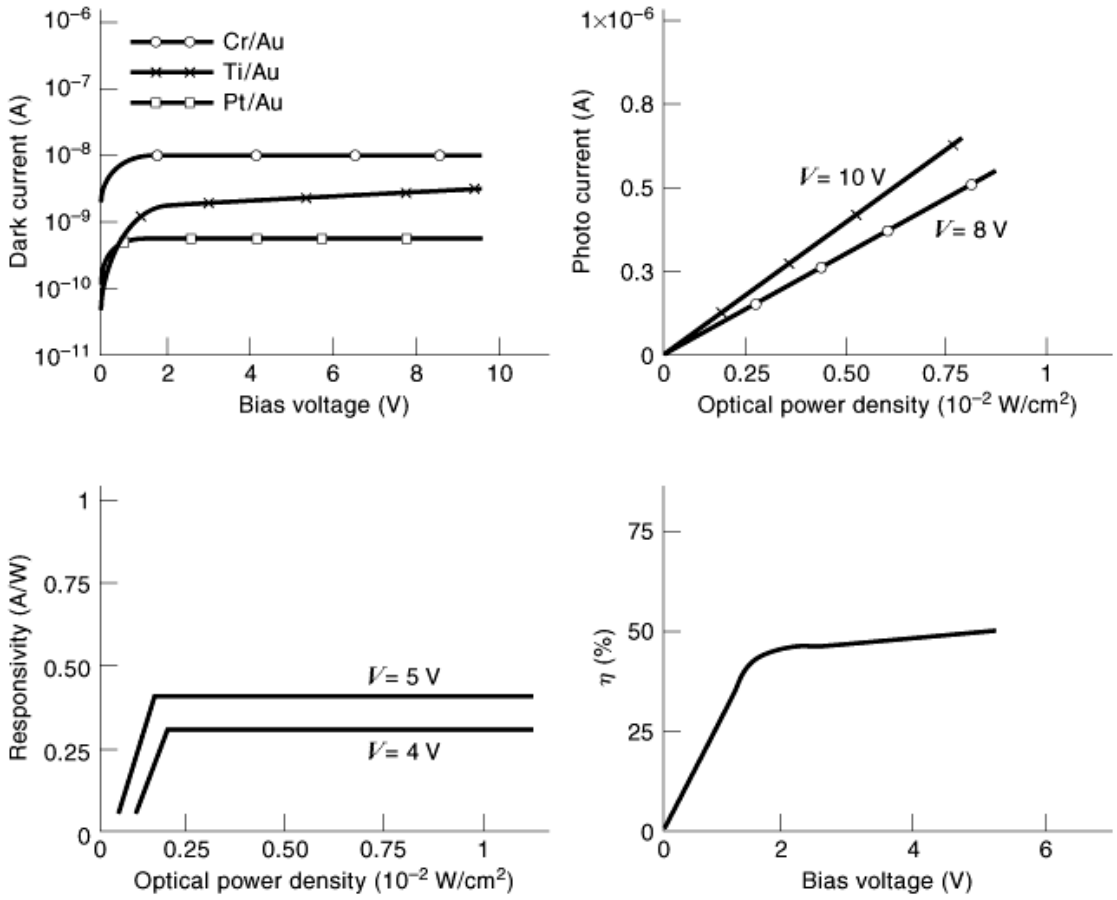

Fig. 21. Dark current, photocurrent, responsivity, and quantum efficiency of a GaAs MSM PD ($L_3 = 2\ \mu$m, $L_4 = 4\ \mu$m).

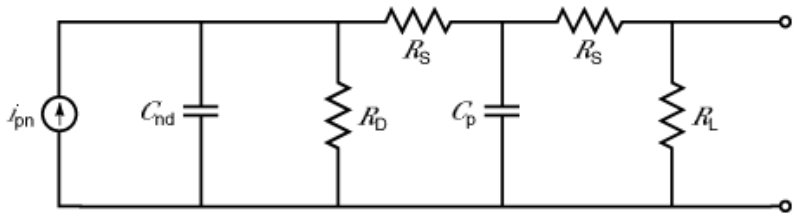

Fig. 22. Equivalent circuit of a MSM PD.

Quantum well infrared photodetectors (*QWIPs*) are very attractive for the detection of far-infrared radiation. The intersubband transition of carriers from the ground state to the first excited state in a wide quantum well and the transition of carriers from a quasibound state to the continuum in a narrow quantum well due to the absorption of photons are responsible for the detection of far-infrared radiation.

Pseudomorphic $In_xGa_{1-x}As/Al_{0.4}Ga_{0.6}As$ MQW structures having well width ~100 Å with intersubband energy separation 100 meV to 200 meV show an absorption peak in the range of wave numbers from 1650 cm^{-1} at 8 K to 1550 cm^{-1} at 300 K. In a quasi-type-II superlattice structure such as $InAs/Al_{0.3}Ga_{0.7}Sb$, absorption is allowed with polarization parallel to the direction of the epilayer growth. In intersubband absorption, the photogenerated carriers create the photocurrent by tunneling through the wells. However, in a $In_xGa_{1-x}As/GaAs$ MQW the absorption peak is extended to longer wavelengths, since the transition of carriers due to photoabsorption takes place between the bound state and the continuum outside the well above 20 meV. In this process tunneling is avoided, and by applying a thick barrier the device dark current can be reduced.

Mercury cadmium telluride (*MCT*) (HgCdTe) photoconductor arrays are used for detection of long-wavelength radiation from 3 μm to 14 μm in wavelength. These are operated in either the photovoltaic mode or the photoconductive mode. The typical detectivity of such a photoconductive array $\approx 7 \times 10^8$ $m \cdot Hz^{1/2}/W$ at wavelength 11 μm and 77 K.

Optical Field Effect Transistors

The optical control of microwave devices is of tremendous interest in optical communication system for the following reasons:

(1) Optical detection and simultaneous amplification
(2) Compatibility with microwave monolithic integrated circuits (*MMICs*) and optoelectronic integrated circuits (*OEICs*)
(3) Reduced size and weight
(4) Immunity to interference and good electrical isolation.

The direct optical control in microwave devices also provides gain in amplifiers, phase shifting in phase shifters, and frequency tuning or locking in oscillators. The effect of illumination has been studied in *MESFETs* (metal–semiconductor FETs) and *MODFETs* (modulation-doped FETs) [also called HEMTs (high electron mobility transistors)]. Due to high mobility, the speed of an HEMT is much higher than that of a MESFET.

Optical Effects in Metal–Semiconductor FETs. The schematic MESFET structure with optical illumination is shown in Fig. 23(a). The fundamental physical mechanism of the optical field effect transistor (*OPFET*) is the generation of electron–hole pairs within the semiconductor when photons of energy equal to or greater than the bandgap energy of the semiconductor are absorbed. The device may be illuminated either from the front or from the back. In front illumination, the device may have a transparent or semitransparent Schottky gate (100 Å to 300 Å thick) or may have an opaque gate. Thus the penetration of photons may be through the gate and/or the gaps between the source, gate, and drain of the device. In back illumination, light is incident on the device through the substrate, into which the fiber may be inserted fully or partly [Fig. 23(b, c)]. The excess carrier generation in the active and substrate regions of the device leads to conductivity modulation of the channel region. In addition there are photovoltage drops across the Schottky-gate–semiconductor junction and the channel–substrate junction, which give rise to channel width modulation, significantly increasing the channel current due to the impurity concentration. The photovoltage developed across the Schottky junction is called the *external* photovoltage, and that due to the channel–substrate junction is called the *internal* photovoltage. The photoconductive effect also takes place in the parasitic resistances in series with the active channel. These change the transconductance, the *I–V* characteristics, and the switching characteristics of the device.

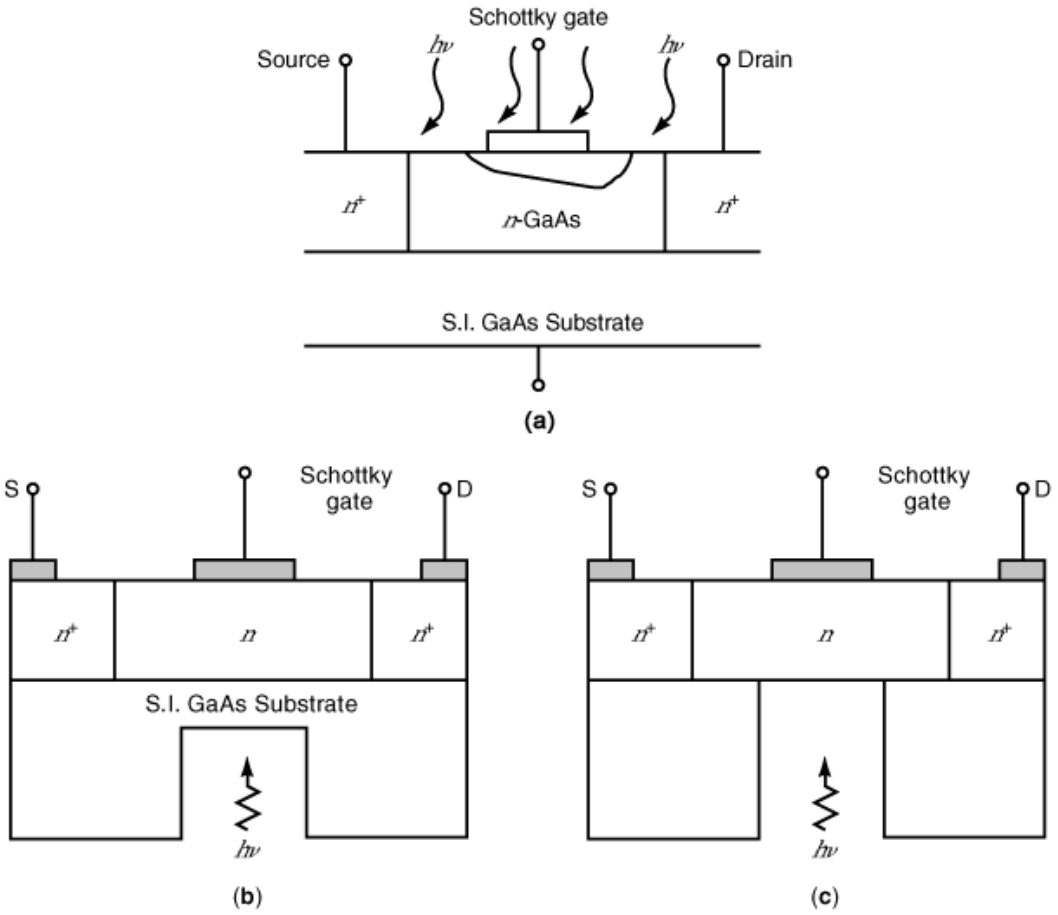

Fig. 23. Schematic structure of a GaAs optical FET.

Several investigations have been carried out on the analytical modeling of a MESFET, assuming both uniform and nonuniform doping profile in the active region. It is observed that an ion-implanted profile gives better performance of the device than constant doping and other profiles. Therefore, an outline of the theory of an ion-implanted OPFET with MESFET structure is discussed below.

The generalized model consists of illuminating the device through the semitransparent or transparent gate and the spacing between source, gate, and drain under front illumination. Commercial MESFETs have an opaque gate, which can be treated as a special case. The drain–source current includes current due to ion implantation and photogeneration. The photogeneration takes place in the (1) gate depletion region, (2) channel region, and (3) active-layer substrate depletion region and can be written as

$$I_{DS} = I_{ion} + I_{dep} + I_{ch} + I_{sub}$$

The ion-implantation profile can be represented by a symmetric Gaussian distribution function as

$$N_{\mathrm{D}}(Y) = \frac{Q}{\sqrt{2\pi}\sigma} \exp -\left(\frac{Y - R_{\mathrm{P}}}{\sqrt{2}\sigma}\right)^2 - N_{\mathrm{A}}$$

where Q is the implanted dose per unit area, R_{P} is the range parameter and σ is the straggle parameter, both in units of length.

The excess carriers generated in the depletion region move by drift and recombination, and those generated in the neutral region move by diffusion and recombination. Hence the dc transport equation can be written as

$$\frac{dn}{dy} - \frac{n}{v_y \tau_n} = \frac{R_{\mathrm{s}}}{a v_y} - \frac{\alpha\phi e^{-\alpha y}}{v_y} \qquad \text{for electrons}$$

$$\frac{dp}{dy} + \frac{p}{v_y \tau_p} = \frac{R_{\mathrm{s}}}{a v_y} - \frac{\alpha\phi e^{-\alpha y}}{v_y} \qquad \text{for holes}$$

in the depletion region and

$$\frac{d^2 n}{dy^2} - \frac{n}{D_y \tau_n} = \frac{R_{\mathrm{s}}}{a D_n} - \frac{\alpha\phi e^{-\alpha y}}{D_n} \qquad \text{for electrons}$$

$$\frac{d^2 p}{d_y{}^2} + \frac{p}{D_p \tau_p} = \frac{R_{\mathrm{s}}}{a D_p} - \frac{\alpha\phi e^{-\alpha y}}{D_p} \qquad \text{for holes}$$

in the neutral or channel region. Here R_{s} is the surface recombination rate, the carriers being assumed to recombine with the surface traps. It is given by

$$R_{\mathrm{s}} = \frac{N_{\mathrm{T}} k_n k_p (n_{\mathrm{s}} p_{\mathrm{s}} - n_{\mathrm{t}} p_{\mathrm{t}})}{k_n (n_{\mathrm{s}} + n_{\mathrm{t}}) + k_p (p_{\mathrm{s}} + p_{\mathrm{t}})}$$

where N_{T} is the trap density per unit area, k_n and k_p are capture factors for electrons and holes, and n_{s} and p_{s} are the surface carrier concentrations for electrons and holes and take the values n_{t} and p_{t} when the Fermi level lies within the traps. Finally a is the active-layer thickness, and v_y is the lateral velocity of carriers, which is nearly equal to the saturated velocity. The above equations consider both surface and bulk recombination.

The equations are solved by applying the following boundary conditions:

$$\text{at} \quad y = 0, \quad n = \alpha\phi\tau_n; \qquad \text{at} \quad y = y_{\mathrm{dg}}, \quad n = \alpha\phi\tau_n e^{-\alpha y_{\mathrm{dg}}}$$

and so on. The photoresponse characteristics are obtained from the current generated due to photoabsorption. The excess electron concentration within the gate depletion region is obtained as

$$N_{\mathrm{dep}} = \frac{\alpha\phi\tau_n}{1 + \alpha v_y \tau_n} \exp(-\alpha y) - \frac{R_{\mathrm{s}} \tau_n}{a}$$

In deriving the above equation, the constant associated with the exponentially increasing function is set equal to zero on physical grounds. The corresponding charge and current in the channel are obtained using the relation

$$\begin{aligned} Q_{\text{dep}} &= \int_0^{y_{\text{dg}}} n_{\text{dep}}\, dy \\ I_{\text{dep}} &= \frac{q\mu z}{L} \int_0^{y_{\text{dg}}} n_{\text{dep}}\, dy \end{aligned}$$

where y_{dg} is the extension of the depletion region in the channel from the surface and is expressed as

$$y_{\text{dg}} = \left(\frac{2\varepsilon}{qN_{\text{de}}} \left[\phi_{\text{B}} - \Delta + V(x) - V_{\text{gs}} \right] \right)^{1/2}$$

in which ϕ_{B} is the metal–semiconductor work function difference, Δ is the position of the Fermi level below the conduction band in the neutral region, $V(x)$ is the channel voltage, V_{gs} is the gate–source voltage, and N_{de} is the equivalent constant doping for the ion-implantation profile.

With regard to the photovoltaic effect, the photovoltage is developed across the Schottky junction and the channel–substrate junction due to the flow of holes. This reduces the depletion width, because it acts as a forward bias. The photovoltages are calculated using the relations

$$V_{\text{op1}} = \frac{kT}{q} \text{In} \frac{J_p(0)}{J_{\text{s1}}} \quad \text{and} \quad V_{\text{op2}} = \frac{kT}{q} \text{In} \frac{J_p(a)}{J_{\text{s2}}}$$

where $J_p(0)$ and $J_p(a)$ are the hole current densities crossing the surface and the n–p junction, V_{op1} and V_{op2} are the external and internal photovoltages, and J_{s1} and J_{s2} are the saturation current densities in the Schottky junction and n–p junction respectively. The electron density generated in the neutral channel region is given by:

$$\begin{aligned} n_{\text{ch}} = {} & \alpha\phi\tau_n \exp\left(-\alpha y_{\text{ds}} + \frac{y_{\text{ds}}}{L_n} \right) \exp\left(\frac{-y}{L_n} \right) \\ & + \frac{R_{\text{s}}\tau_n [\exp(y_{\text{ds}/L_n}) - 1] e^{-y/L_n}}{a} \\ & + \frac{\alpha\phi\tau_n}{D_n\tau_n\alpha^2 - 1} \left[\exp\left(\frac{1}{L_n} - \alpha \right) y_{\text{ds}} - \exp(-\alpha y) \right] \end{aligned}$$

The electron concentration generated in the channel–substrate depletion region is given as

$$n_{\text{sub}} = \frac{\alpha\phi\tau_n}{1 + \alpha\phi\tau_n} e^{-\alpha y}$$

The corresponding charge density and channel current are obtained using the relations mentioned above. The gradual-channel approximation is used for the calculation of current for long- or medium-channel devices.

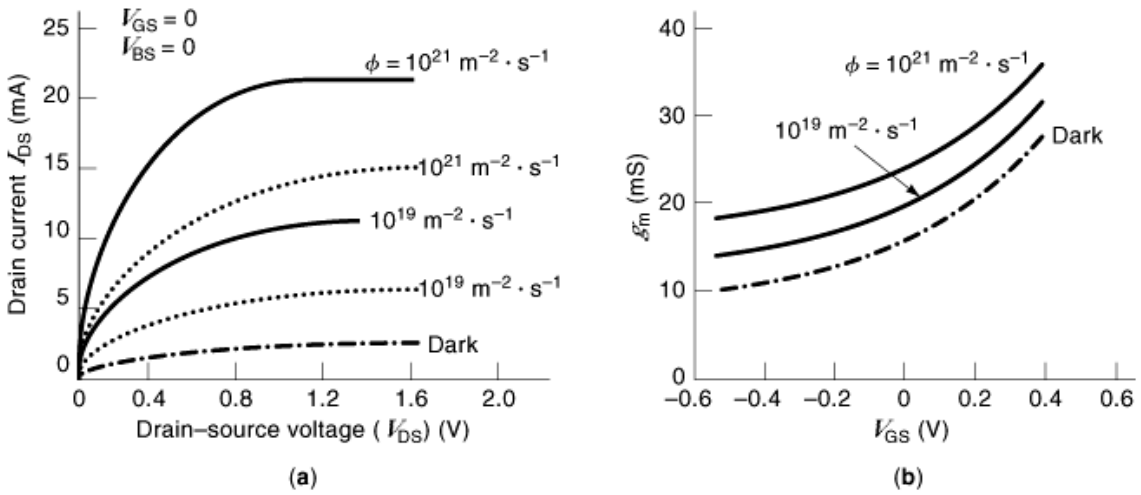

Fig. 24. (a) I–V characteristics and (b) transconductance for an ion-implanted GaAs OPFET: solid curves, generalized model; dashed curves, opaque-gate model.

Figure 24 shows the characteristics and the transconductance for the generalized model of the ion-implanted GaAs OPFET. It also shows the characteristics for an OPFET with an opaque gate. The generalized model show higher current and transconductance than the opaque-gate model.

The radiation flux density has a significant effect on device characteristics. The switching model of the OPFET shows that the gate–source and gate–drain capacitances of the device do not change with flux density, but the transconductance and channel conductance change appreciably. Thus the cutoff frequency of the OPFET when used as an amplifier increases with radiation flux density according to

$$f_T = \frac{g_m}{2\pi(C_{gs} + C_{gd})}$$

The transient response of the ion-implanted GaAs OPFET shows that when the light is turned on, different electrical parameters of the device reach their steady-state values within 10 ps to 20 ps, depending on the absorption coefficient of the material (and thus the wavelength of operation). However, with the light turned off, the electrical parameters reach their dark values in a longer time, $\approx$ 250 ps. For the first case, it is the optical relaxation time, defined as $1/\tau_{op} = \alpha v_y + (1/\tau_p)$, that controls the changes, whereas for the second case, the controlling parameter is the photovoltage developed across the junction, which varies linearly with time.

The scaling of OPFETs is also important for device integration. The experimental results on the effect of illumination on MESFETs are in good agreement with the theoretical observations.

Optical Effect in Modulation-Doped FETs. The MODFET, or HEMT, has created revolution in the field of microwave devices. The device can be used up to a frequency of 400 GHz with a very low noise figure, $\approx$ 0.15 dB. A digital IC with MODFETs made of AlGaAs/GaAs heterostructures has a speed of a fraction of a picosecond. The device can be easily fabricated by MBE. It is thus of interest to study the optical effects in this device.

Figure 25(a, b) show the schematic structure of an optically illuminated MODFET. In Fig. 25(a) illumination falls on transparent or semitransparent Schottky gate, and in Fig. 25(b) it is absorbed through the spacings between source, gate, and drain, the gate being opaque to radiation. The generalized model for the MESFET is

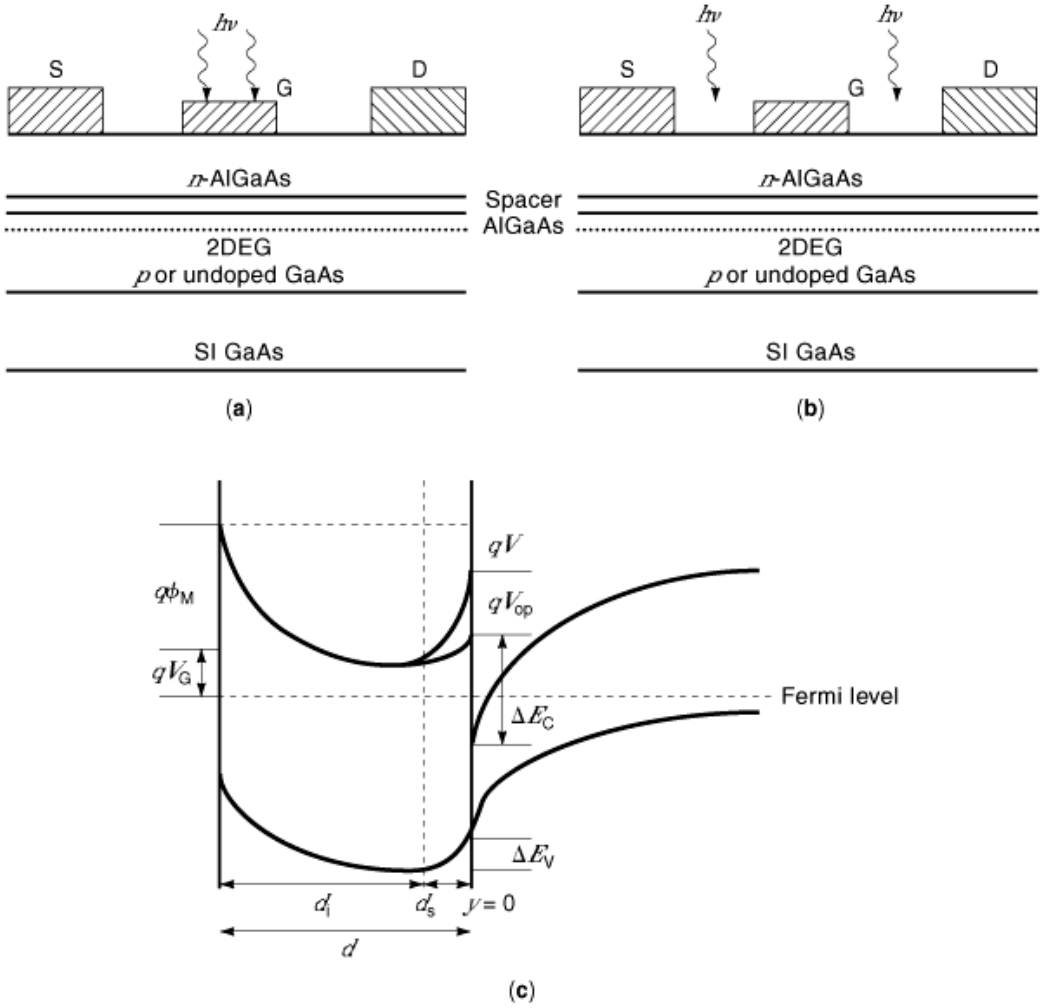

Fig. 25. (a) MODFET with transparent or semitransparent gate. (b) MODFET with opaque gate. (c) The energy band diagram for an AlGaAs–GaAs MODFET.

not applicable here. In a MODFET, the radiation falling through the transparent or semitransparent Schottky gate gives rise to a photovoltage across the Schottky junction, which reduces the depletion width of the active region. So to maintain the complete depletion of the active layer (which is normally assumed in the theoretical analysis) an equal amount of negative gate voltage has to be applied, which degrades the performance of the device. On the other hand, the opaque-gate model of the MODFET implies an enhanced optical effect, which in fact is observed in commercially available MODFETs. For the transparent or semitransparent Schottky gate, the metal thickness has to be reduced significantly (100 Å to 300 Å), which increases the gate parasitic resistance and reduces the speed of the device. A two-dimensional analytical model for an optically illuminated GaAlAs/GaAs MODFET with realistic carrier-velocity field dependence in the active region requires solving Poisson's equation in two dimensions:

$$\frac{\partial^2 V(x,y)}{\partial x^2} + \frac{\partial^2 V(x,y)}{\partial y^2} = \frac{\rho(y)}{\varepsilon}$$

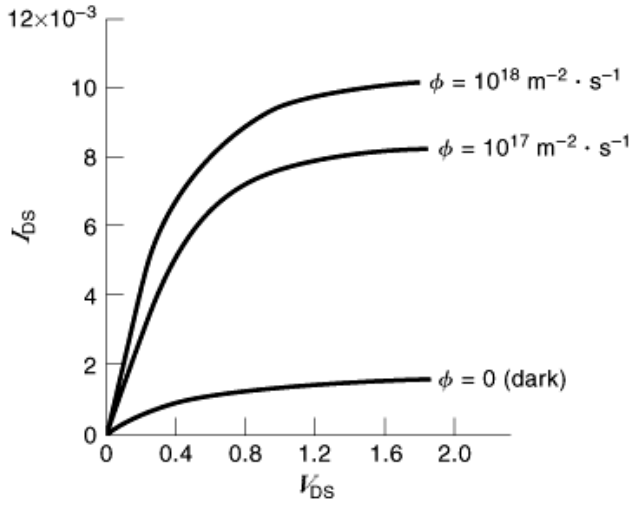

Fig. 26. *I–V* characteristics of MODFET in dark and under illumination.

where $\rho(y)$ is the charge density of the n-AlGaAs layer and is given by $\rho(y) = q[N_D(y) - n + p]$, in which $N_D(y)$ is the ionized donor concentration and n and p are the densities of excess electrons and holes generated by photoabsorption. As shown in the EB diagram in Fig. 25(c), the photovoltage developed across the heterojunction enhances the CB edge discontinuity in the MODFET, thereby enhancing the sheet concentration of the two-dimensional electron gas in the quantum well of the device. The velocity–field relation for electrons in n-AlGaAs is given by

$$v_n(x) = v_s\left(1 - e^{\mu E/v_s}\right)$$

where v_s is the scattering-limited velocity, μ is the low-field mobility, and E is the applied field. Using a variable transformation, the two-dimensional Poisson's equation is converted into Laplace's equation and is solved with the appropriate boundary conditions. Since the two-dimensional theoretical expressions are complicated, the sheet concentration per unit area of the two-dimensional electron gas (2DEG) is presented in one dimension as

$$n_s(x) = \frac{q}{q^2 d + \varepsilon a}[V_G - V_{OFF} - V(x)]$$

where $a = 0.125\times10^{-16}$ V·m for AlGaAs, $V(x)$ is the channel potential, and V_{OFF} is the offset voltage given by

$$V_{OFF} = \phi_M + \frac{E_F - E_C}{q} - V_{op} - \frac{qN_D d^2}{2\varepsilon} - \frac{q\phi\tau_n}{\varepsilon\alpha}e^{-\alpha d}(1 + \alpha d - e^{-\alpha d}) - \frac{qR_s\tau_p d}{2\varepsilon}$$

The drain current is obtained using the relation

$$I_D = qn_s z V(x)$$

where z is the channel width.

Figures 26 and 27 show the *I–V* characteristics and transconductance for an illuminated MODFET obtained from the two-dimensional calculation, along with corresponding dark values. The ratio of the drain

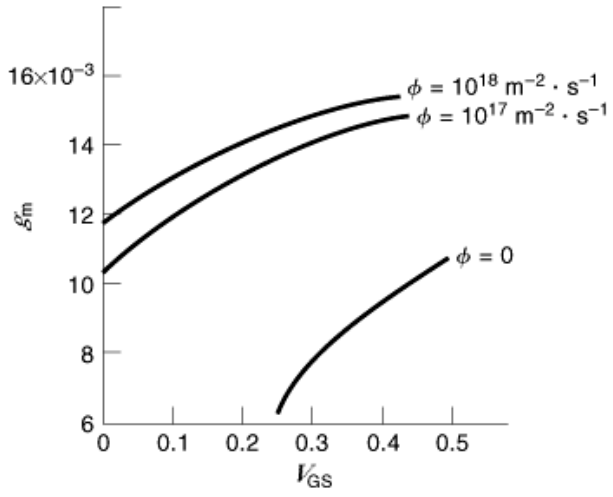

Fig. 27. Transconductance versus v_{GS} for MODFET.

current under illumination to that in the dark is larger than 10, indicating a large gain when the device is used as an amplifier with optical control. The transconductance also increases significantly.

Application of the OPFET. An OPFET can be illuminated by a laser diode made of III–V semiconductors, which leads to the integration of OPFET and laser diode (*LD*) or light-emitting diode (*LED*) on a single MMIC chip. This combination can perform multiple circuit functions, such as switching, amplifier gain control, mixing, phase shifting, etc. Further, simultaneous detection and amplification by an OPFET makes it useful in OEICs for application in communication and superfast computers.

Optoelectronic Switch

Double Heterostructure Optoelectronic Switch. The double heterostricture optoelectronic switch (DOES; also called digital optoelectronic switch) was proposed a decade ago. The basic physical structure and the EB diagram of the device are shown in Fig. 28(a, b).

It is a multilayer structure, where the substrate is a heavily doped p-type wide-bandgap semiconductor of either AlGaAs or InP, followed by an epitaxial layer of n-type narrow-bandgap semiconductor (either GaAs or InGaAsP), which acts as an active layer, thus forming a p–n heterojunction. On the active layer a thin barrier layer of n-doped wide-bandgap semiconductor ($\approx$ 300 Å) is formed, along with a heavily doped p^+ layer (charge-sheet layer, $\approx$ 40 Å) at the interface with the thin layer. The charge sheet may be formed either at the narrow-bandgap or at the wide-bandgap semiconductor surface, both being at the interface of the n–n heterojunction. This charge sheet gives the device for its unique electrical and optical characteristics. A metal emitter on the barrier layer completes the DOES structure. In comparison with the double heterostructure (DH) LED or the laser, it is observed that in the DOES the heterojunction provides both electrical and optical confinment in the active region. The strongly inverted surface at the n–n heterostructure is basically an open-source bipolar inverted-channel field-effect transistor (*BICFET*). In the neutral active region, photons are generated due to radiative recombination.

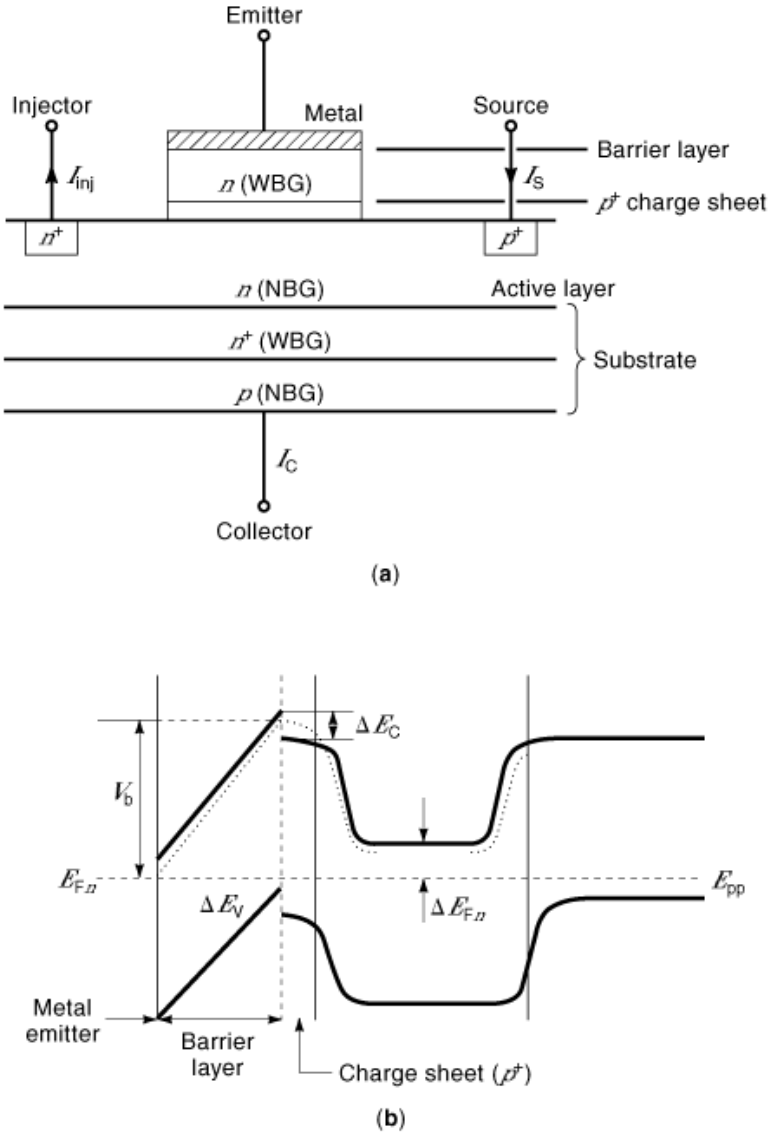

Fig. 28. (a) Basic physical structure of DOES. (b) Energy band diagram of DOES at equilibrium [after Simmons et al. (1)].

The I–V characteristic (Fig. 29) of the device shows three different regions: (1) a high-impedance off state, (2) a low-impedance on state, and (3) a differential negative-resistance region (*DNRR*) connecting the off and on states.

The internal-optical-efficiency–current characteristic (Fig. 30) shows that when the device is in the on state the light intensity increases with increase in current. The transitions from the on to the off state and vice versa are governed by the terminal current and the voltage. Thus, for digital application the device performs the switching operations for both electrical and optical conditions; the electrical and optical output states are determined by the electrical input states.

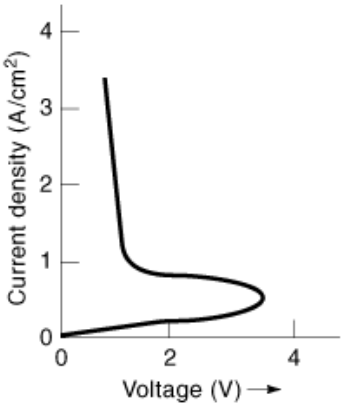

Fig. 29. Typical I–V characteristic of DOES.

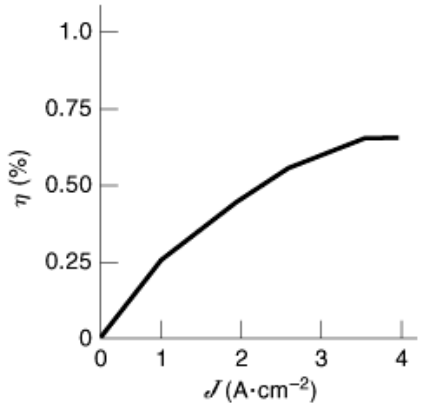

Fig. 30. Internal optical efficiency versus current density for DOES.

DOESs can be fabricated with two, three, or four terminals. The physical structure of a four-terminal DOES is shown in Fig. 28(a). In the three-terminal case, the third terminal is either the source or the injector. When the source is activated, the emitter is grounded. For the four-terminal case either emitter or collector is grounded.

The DOES has wide applications. It has been demonstrated that a pair of parallel-coupled DOESs can be used for very low-power differential optical switching. For an optical pulse width of 200 ns switching was achieved using an optical power input of 20 μW. Since the DOES operates on differential inputs, it is tolerant to background noise and input light instability. The device is attractive for optical neural networks and optical digital computers.

An optical inverter has been constructed with a two-terminal DOES capacitively coupled to a three-terminal DOES (Fig. 31). The three-terminal self-aligned DOES has also been demonstrated for use as a memory cell. There may be several other applications of DOESs. In the OEIC the DOES is compatible with HFETs and BICFETs.

Self-Electro-optic-Effect Device. Self-electro-optic-effect devices (SEEDs) show four modes of operation: (1) optical stability, (2) electrical stability, (3) simultaneous optical and electronic oscillation, and

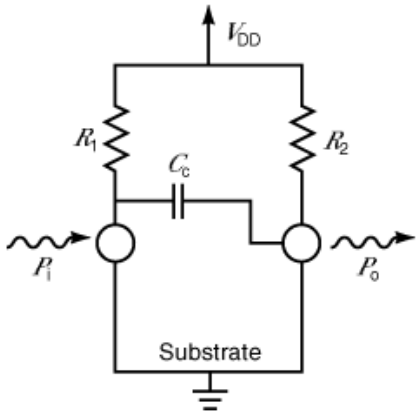

Fig. 31. Optical inverter using DOES; R_1 and R_2 are bias resistors.

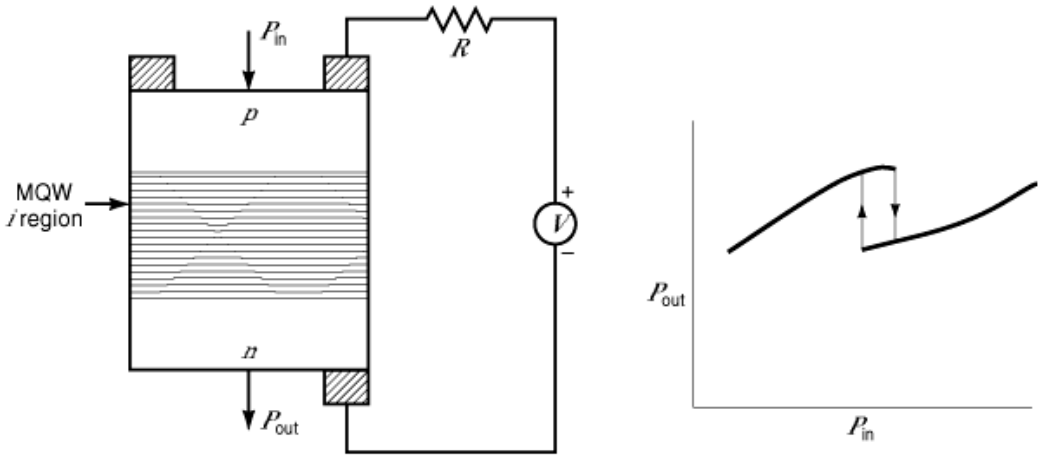

Fig. 32. Basic SEED circuit and its switching characteristics.

(4) self-linearized modulation and optical level shifting. Using a CW laser as a light source, all these operations can be observed at room temperature. The multiple-quantum-well structure (*MQWS*), with alternate layers of GaAs and AlGaAs, shows exciton absorption peaks near the optical absorption edge. When an electric field is applied perpendicular to the quantum well layers, the whole absorption edge moves to lower photon energy, which is not observed in normal semiconductors. This is due to sharp resonances resulting from the transitions between heavy-hole-to-electron (*e–hh*) and light-hole-to-electron (*e–lh*) subbands. This phenomenon is known as the quantum-confined Stark effect (*QCSE*). For a 100 Å quantum well the separation between these resonances is $\approx$ 10 meV. When an MQW PD is incorporated in the *i* region of a *p–i–n* photodiode and a reverse bias is applied, the photocurrent exhibits negative differential resistance (*NDR*). The QCSE and NDR together can be exploited to develop a number of photonic switching and logic devices. The SEED is one of the most important devices based on these two effects. The basic SEED circuit with a series resistor is shown in Fig. 32 along with the switching action.

The SEED principle is that the photocurrent flowing through the circuit influences the voltage across the modulator, which in turn influences the absorption of light in the modulator and hence the photocurrent. The

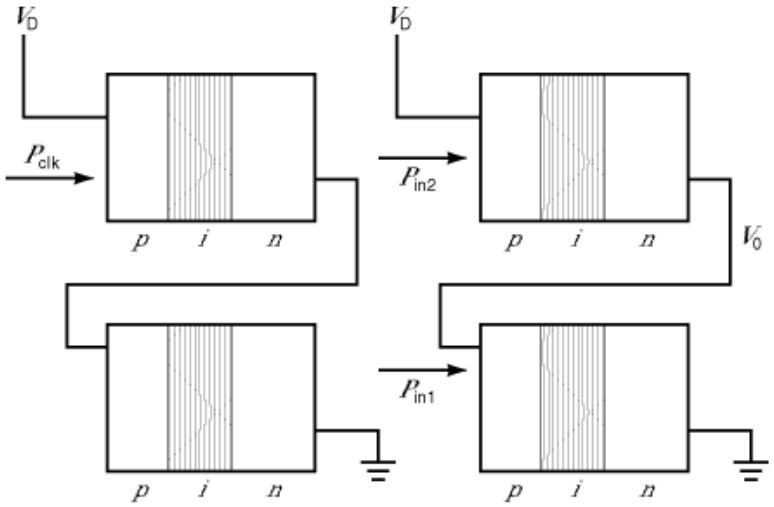

Fig. 33. SSEED flip-flop.

photonic switching can be understood from the characteristics of the device. The MQW p–i–n diode is reverse biased, and when light of energy lower than the hh resonance is incident on it, the hh peak is shifted to lower energies. If the energy coincides with the low-absorption region between the hh and lh resonances, most of the light is transmitted. So light is transmitted when the input power is low, and the output power increases in proportion to input power. The photocurrent increases with the intensity of light, thereby increasing the voltage drop across the series resistance in the circuit. As the applied bias is constant, the voltage across the diode decreases, which shifts the hh absorption peak to higher energies, so that the transmission decreases. When the input power increases further, the output power increases again and the diode changes its state. So the phenomenon leads to completely photonic switching.

The behavior of the SEED depends on the nature of the electronic circuit and the type of feedback. With positive feedback, bistability and oscillation can be obtained. Under negative feedback, self-linearized modulation, linear light modulation, optical level shifting, etc. can be obtained.

System Application of Self-Electro-Optic-Effect Devices. A prototype optical signal processing system can be realized by using symmetric SEED (*SSEED*). The device can work as optical set–reset latch or as a differential optical logic gate such as NOR, OR, NAND, or AND. In both cases, the device has time-sequential gain and provides signal timing regeneration. It is insensitive to optical power supply fluctuations and gives input–output isolation.

Figure 33 shows a cascaded SSEED set-reset (S-R) flip-flop, and Fig. 34 shows casaded SSEED differential logic gates. The incident power (P_{in}) on the second stage is related to the clock power (P_{clk}) of the first stage by

$$\begin{aligned} P_{in1}(t) &= T[V_1(t)]P_{clk}(t)T_{opt}F_{in}/F_{out} \\ P_{in2}(t) &= T[V_0 - V_1(t)]P_{clk}(t)T_{opt} \end{aligned}$$

where $T[V_1(t)]$ and $T[V_0 - V_1(t)]$ are the optical transmissions and reflections from the MQW diode in the first stage, F_{in} and F_{out} are the fan-in and fan-out of the second- and first-stage devices respectively, and T_{opt} is the transmission of the optics interconnecting the devices. From the knowledge of the switching time (Δt) of the

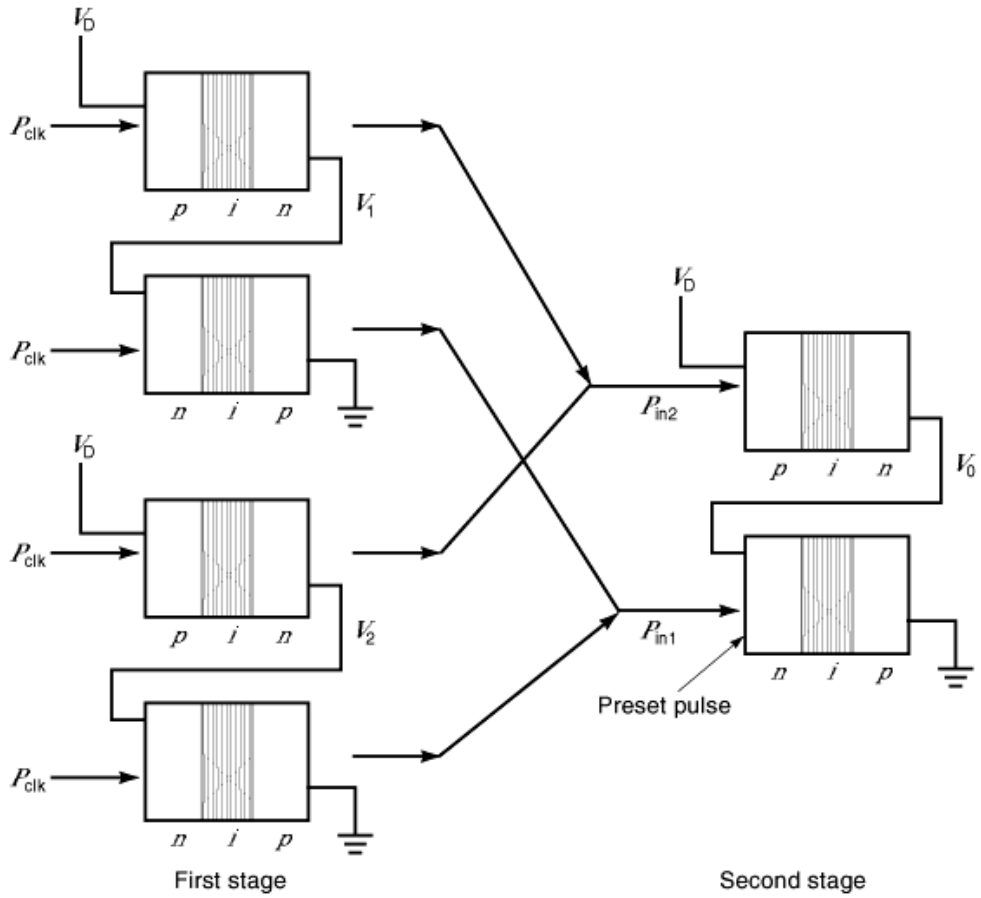

Fig. 34. Cascaded SSEED differential logic gate [after Leutine et al. (2)].

SSEED, one can calculate the bit rate using the relation

$$\text{bit rate} = \frac{1}{2\Delta t}$$

SEED optical oscillators have also been realized at 110 MHz having optical-pulse rise time 2 ns. Oscillation frequencies as high as 2 GHz have been obtained. A SEED heterojunction bipolar transistor (*HBT*) can be operated as a programmable flip-flop memory element or a tunable thereshold logic gate.

Light-Amplifying Optical Switch. A light-amplifying optical switch (*LAOS*) consists of a heterojunction phototransistor (*HPT*) in series with a LED (or a LD) in a single chip. It switches the device from the low-current state through the region of NDR when a voltage greater than the breakover voltage is applied. This NDR characteristic of the LAOS is due to optical feedback and/or electrical feedback and can be controlled by varying the feedback coefficient and the Early-effect coefficient of the transistor.

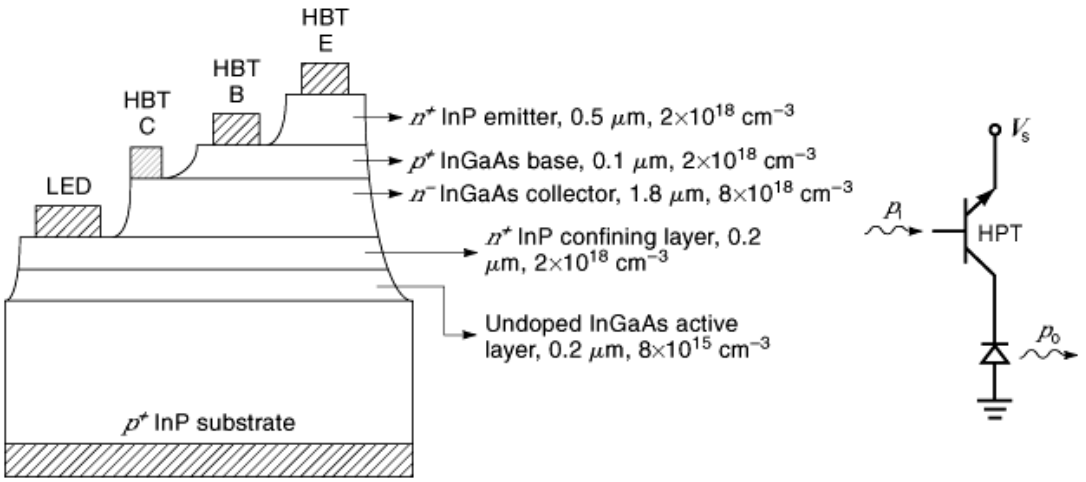

Fig. 35. Physical structure of a LAOS and its equivalent circuit [after Feld et al. (3)].

A simple LAOS structure with HPTs and LEDs based on the InGaAs/InP system is shown in Fig. 35 along with its equivalent circuit. A similar structure has also been proposed earlier with HPTs and LDs. The device is vertically integrated with epitaxial layers of AlGaAs/GaAs or InGaAs/InP grown by either liquid phase epitaxy (LPE) or MBE. Since the input light power is detected by the HPT, the LAOS has a wide spectral response, in addition to high optical gain and switching speed.

The characteristics of the LAOS at small applied voltages are similar to the characteristics of a HPT shifted by the voltage drop across the LED. At high voltages the device switches from a low-current to a high-current state through NDR. The device operation is explained as follows: the input light is applied at the base of the HPT, which generates electron–hole pairs in the base region. The resulting current is increased by the transistor current gain. It flows through the LD or LED, and if it is higher than the LD or LED threshold current, a part of the LED output current is fed back (optical feedback) to the base of the HPT. The electrical feedback is achieved by hole injection from the cladding layer of the LED to the collector side of the HPT. The EB diagram in Fig. 36 shows the processes of optical and electrical feedback in the LAOS device. The equivalent circuit of a LAOS with feedback processes, Early effect, and parasitic resistances is shown in Fig. 37.

With optical feedback, the diode current I_D is given by

$$I_D = I_C + \delta V_{CE} I_B + \frac{V_{CE}}{R_L}$$

where I_C is the collector curent, and I_B is the base current. The second term represents the Early-effect current source. Also,

$$I_c = \beta^2 (I_{inj} + I_{op})^2$$

where $I_c = \gamma I_D$, γ being the optical feedback coefficient, and I_{inj} is the injected current from emitter to base of the HPT. The I–V characteristics of the LAOS are shown in Fig. 38 for both electrical and optical feedback.

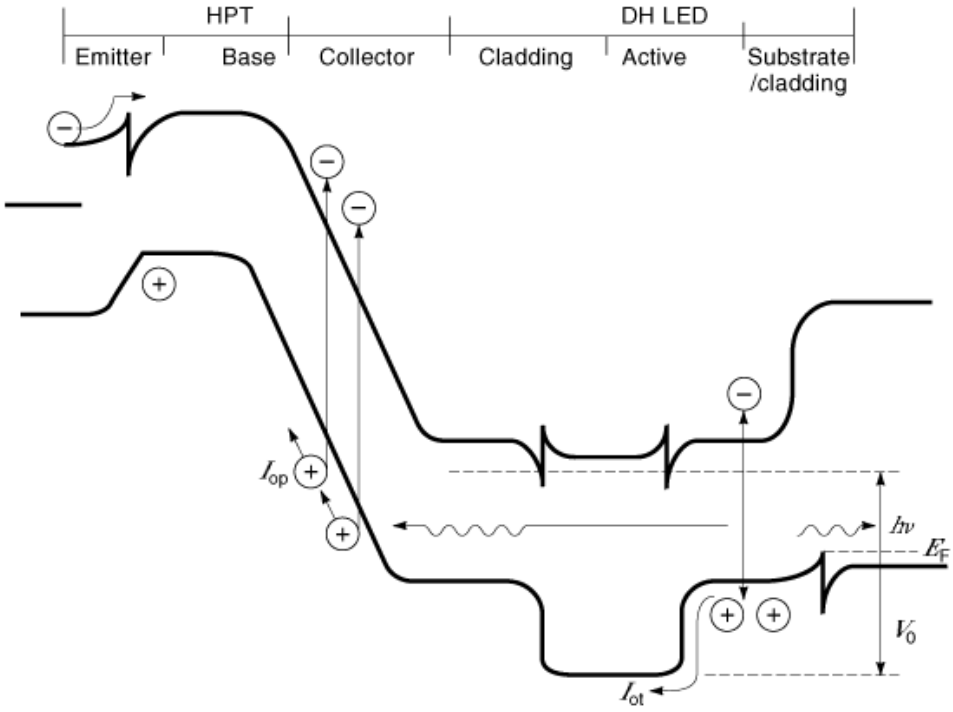

Fig. 36. Band diagram of LAOS, indicating electrical and optical feedback processes [after Feld et al. (3)].

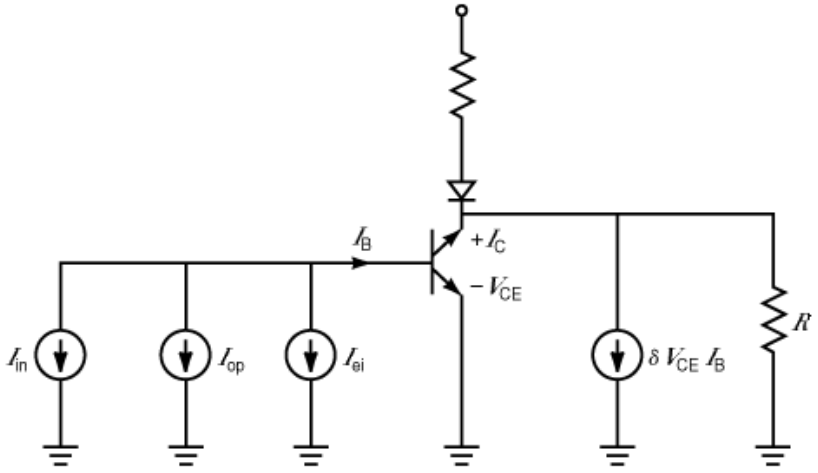

Fig. 37. Equivalent circuit of LAOS with Early effect, leakage, and series resistances.

Switching action takes place at the proper bias voltage of the HPT. The switching voltage is a strong function of the space charge recombination current.

Recently a LAOS with GaAs OPFET and LED has been suggested in which the breakover voltage decreases as the radiation flux density increases.

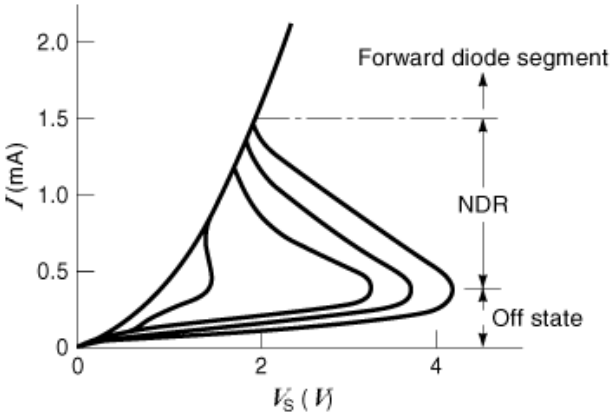

Fig. 38. LAOS characteristics due to both electrical and optical feedback.

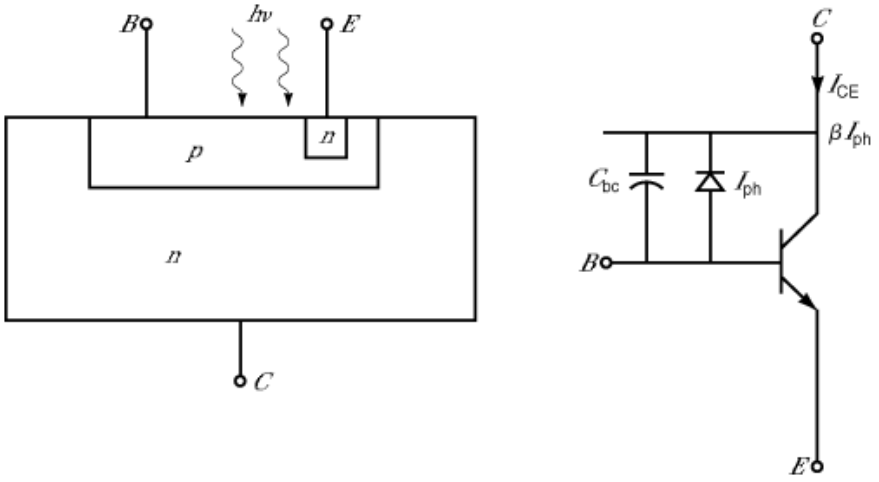

Fig. 39. A typical bipolar phototransistor structure and its circuit model.

Phototransistor

A phototransistor is a bipolar device that works both as a detector and as an amplifier due to its internal gain. Sometimes the base is floating and the optical signal acts as the base current.

A bipolar phototransistor together with its circuit model is shown in Fig. 39. It has a larger base–collector junction than the conventional bipolar transistor, which acts as the light-connecting element and is repesented by a parallel combination of a diode and a capacitor. The device gives high current transfer ratio ($\approx 50\%$), which makes it useful in optoisolator applications.

The band diagram of a HPT is shown in Fig. 36. The wide-bandgap emitter enhances the current gain and acts as a window to optical radiation, so that the photoabsorption takes place in the neutral base region and the base–collector depletion region. The base and collector operate as a reverse-biased photodiode, and the HPT operates in the common-collector configuration. Under the floating base condition, the photogenerated carriers contribute a photocurrent I_{ph} in the collector. In addition there are holes generated in the base and

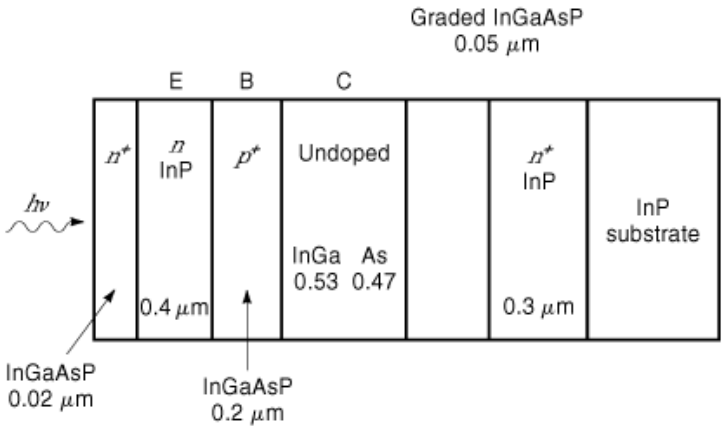

Fig. 40. Schematic structure of a InGaAs/InGaAsP/InP HPT for long-wavelength detection.

holes injected from the collector into the base. These together lower the base–emitter barrier, allowing injection of electrons from the emitter. The collector current in a phototransistor thus is given by

$$I_{CE} = (1 + h_{fe})\, I_{ph}$$

where h_{fe} is the common-emitter gain. The optical gain G_{op} of the phototransistor is given by

$$G_{op} = \frac{h\nu}{q} \frac{I_{ph}}{P_{in}}$$

where P_{in} is the incident optical power. Under certain assumptions G_{op} may be obtained as

$$G_{op} = \eta\beta_T \left[1 + e^{-\alpha W_b} \left(1 - e^{-\alpha(X_c - W_b)}\right)\right]$$

where η is the quantum efficiency, β_T is tthe current gain of the phototransistor, X_c is the edge of collector depletion region, and W_b is the base width. Considering that the absorption of photons in the collector is limited to the base–collector depletion region and the base is thin, so that $W_b << L_e$ (the electron diffusion length), the current gain of a phototransistor is given by

$$\beta_T = \frac{h\nu}{q\eta} \frac{I_{ph}}{P_{in}}$$

G_{op} in a phototransistor may be from $\approx$ 100 to 500. The floating-base devices are fabricated as mesa diodes with large areas. Due to minority carrier storage, the response speed of a phototransistor is poor, and the modulation bandwidth is less than 1 GHz. A typical long-wavelength HPT is shown in Fig. 40, where the emitter is of InP, the base of InGaAsP, and the collector of $In_{0.53}Ga_{0.47}As$.

Phototransistors are also made of silicon. A conventional Si bipolar junction transistor (BJT) and MOSFET can be used for light detection and amplification. The Si bipolar phototransistor has a larger collector–base

junction, which degrades the high–frequency performance of the device. The silicon bipolar phototransistor can give a higher current transfer ratio when it is integrated with a second transistor called a photo-Darlington. However, the large collector–base capacitance and the feedback effect degrade the gain and response characteristics of the composite structure.

The silicon MOSFET is useful as an infrared sensor. The p-substrate of the device is doped with a shallow accepter (boron) and a deep acceptor (indium, whose energy lies more than 0.16 eV below the valence band). The indium center can be in either a neutral state or a negatively charged state, depending on whether the hole occupies the state or not. With a negative gate voltage and infrared radiation of wavelength 2 μm to 7 μm falling on the device, there is a threshold voltage shift given by

$$\Delta V_T = 2\sqrt{q\varepsilon\Delta}\left(\sqrt{N_A + N_i} - \sqrt{N_A}\right)\Big/ C_{ox}$$

where Δ is the potential difference between the quasi Fermi level and the intrinsic Fermi level, N_A is the acceptor concentration, N_i is the ionized indium concentration due to photoabsorption, and C_{ox} is the oxide capacitance per unit area. The shift in threshold voltage modulates the channel conductance, resulting in a change in the drain–source current. The infrared silicon MOSFET can be integrated into large-scale imaging arrays and storage (memory) elements.

Optical Waveguides

Optical waveguides are devices used for guiding light confined in a film on a suitable substrate. A laser is a resonant cavity. With suitable choice of different materials of required refractive indices, the light can be confined within the core material (film). Depending on the design and materials, waveguides can perform a wide range of operations such as modulation, switching, multiplexing, filtering, and generation of optical waves.

The optical waveguide is a basic component in integrated optics. It can be planar, strip, periodic, or rectangular. It can be symmetric or asymmetric.

A planar waveguide consists of a film of refractive index n_f deposited on a substrate of refractive index n_s with a cover of refractive index n_c (shown in Fig. 41), where $n_f > n_s, n_c$. For symmetric structures $n_s = n_c$, and for asymmetric structures $n_s \neq n_c$. Where air is the core, $n_s > n_c$. The refractive index varies along the x direction, and so the light is confined in the x direction and can be diffracted in the yz plane.

A strip waveguide consists of materials with high refractive index surrounded by materials of lower indices. The light is confined along both the x and y directions and propagates along the z direction (Fig. 41).

A periodic waveguide is one in which the thickness, refractive index, or both vary periodically along the direction of propagation (Fig. 41). Many important functions can be realized with these waveguides, such as distributed Bragg and feedback laser structures, filters, mode converters, polarization transformers, input-output couplers, etc.

A rectangular-core waveguide is one in which both transverse and lateral confinement is possible. In a planar waveguide there is only transverse confinement, so that the light wave is confined near the surface of the substrate and core and propagates in the plane parallel to them. The rib and channel waveguides used in integrated optics are rectangular-core waveguides.

Mode of Propagation. Transverse electric (TE) and transverse magnetic (TM) modes are the two important modes of propagation in optical waveguides. The characteristic wave equations and the dispersion relations can be obtained using Maxwell's equations by considering the plane wave approximation. For a

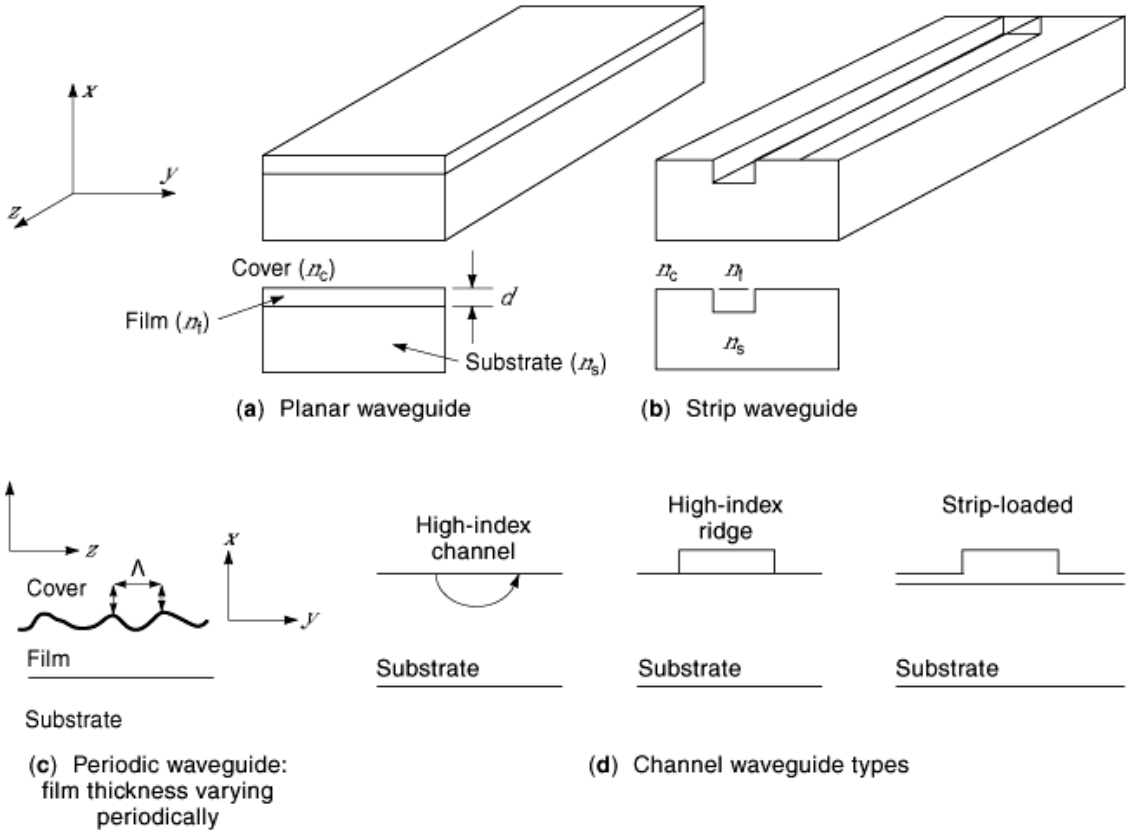

Fig. 41. Different waveguide types.

dielectric medium with no charge and conduction current, Maxwell's equations can be written as

$$\nabla^2 \boldsymbol{E} + \omega^2 \mu \varepsilon_0 \varepsilon_r \boldsymbol{E} = 0$$

and

$$\nabla^2 \boldsymbol{H} + \omega^2 \mu \varepsilon_0 \varepsilon_r \boldsymbol{H} = 0$$

where $\boldsymbol{E}$ and $\boldsymbol{H}$ are the electric and magnetic field vectors, ω is the angular frequency of the propagating wave, μ and ε_r are the permeability and permittivity of the dielectric medium, and ε_0 is the permittivity in vacuum. Assuming that both $\boldsymbol{E}$ and $\boldsymbol{H}$ may be represented by

$$\begin{aligned} \boldsymbol{E}(r,t) &= \boldsymbol{E}_r e^{j(\omega t - \beta z)} \\ \boldsymbol{H}(r,t) &= \boldsymbol{H}_r e^{j(\omega t - \beta z)} \end{aligned}$$

and the interfaces are perfect conductors, the transverse electric and transverse magnetic field components are given by

$$\frac{d^2E_y}{dx^2} - (k_0^2 n_\ell^2 - \beta^2)E_y = 0$$

$$\frac{d^2H_y}{dx^2} - \left(\frac{1}{n_\ell^2}\frac{dn_\ell^2}{dx}\right)\frac{dH_y}{dx} + (k_0^2 n_\ell^2 - \beta^2)H_y = 0$$

where z is the direction of wave propagation, n_l is the refractive index of the media with l = f,s,c,. . ., β is the propagation constant, and $k_0 = \omega\sqrt{\epsilon_0 \mu} = \omega/c = 2\pi/\lambda$ is the wave number in free space. In the above equations E_y, dE_y/dx, H_y, and $(1/{n_l}^2)\, dH_y/dx$ are continuous. Once E_y is known, H_x and H_z can be calculated using the relations

$$H_x = \frac{\beta}{\omega\mu}E_y, \qquad H_z = \frac{1}{\omega\mu}\frac{dE_y}{dx}$$

and once H_y is known, E_x and E_z can be calculated from the relations.

$$E_x = \frac{\beta}{\omega\varepsilon_0 n_\ell^2}H_y, \qquad E_z = \frac{1}{\omega\varepsilon_0 n_\ell^2}\frac{dH_y}{dx}$$

E_y and H_z are tangential components and are continuous across the interfaces.

The refractive index profile for the planar wave-guide is abrupt. The refractive index may be graded also, depending on the fabrication method. The graded index profile $n(x)$ is represented as a Gaussian profile given by

$$n(x) = n_s + (n_f - n_s)\exp\left(-\frac{(x-w)^2}{L_D^2}\right) \qquad \text{for} \quad x < w$$

where w is the guide width and L_D is the diffusion length of carriers in the material.

For an asymmetric guide where $n_s \neq n_c$ and $n_f > n_s > n_c$ and with an abrupt refractive index profile, the equation for propagation characteristics is obtained in terms of the normalized propagation constant and normalized waveguide parameter and is given by

$$\tan\left[V(1-p)^{1/2}\right] = \begin{cases} \dfrac{P^{1/2} + (P+a)^{1/2}}{(1-P)^{1/2} - [P(P+a)/(1-P)]^{1/2}} & \text{for TE mode} \\ \dfrac{L_2 P^{1/2} + L_2(P+a)^{1/2}}{L_1 L_2(1-P)^{1/2} - [P(P+a)/(1-P)]^{1/2}} & \text{for TM mode} \end{cases}$$

where a is the asymmetry parameter, P is the normalized propagation constant, and V is the normalized waveguide parameter, defined as

$$a = \frac{n_s^2 - n_c^2}{n_f^2 - n_s^2}, \qquad P = \frac{(\beta/k_0) - n_c^2}{n_f^2 - n_s^2}$$

and

$$V = k_0 W (n_f^2 - n_s^2)^{1/2}$$

L_1 and L_2 are defined as

$$L_1 = \left(\frac{n_s}{n_f}\right)^2 \quad \text{and} \quad L_2 = \left(\frac{n_c}{n_f}\right)^2$$

For a symmetric waveguide the difference between the propagation constants for the TE and TM modes becomes small as $L \to 1$ and two modes become degenerate. When $P = 0$, this gives the cutoff condition $\beta/k_0 = n_s = n_c$, leading to the cutoff frequency

$$V_c = m\pi \quad \text{for} \quad m = 0, 1, 2, \ldots \qquad \text{for TE and TM modes}$$

If the angle of incidence of the light in the waveguide is such that the electric field vector makes an angle $\pi/4$ at $z = 0$, then the wave is linearly polarized, becomes circularly polarized after propagating a distance z_0, and again becomes linearly polarized after propagating a distance $2z_0$ along the waveguide. Thus, due to the excitation of both TE and TM modes, there is a change in the state of polarization. Coupling of power from one mode to another mode is known as *mode conversion*; it can be used for TE–TM converters, wavelength filters, etc. A waveguide that suports only one type of polarization is known as a single-polarization single-mode (*SMSP*) waveguide.

For symmetric waveguides, $n_s \neq n_c$, so $a \neq 0$. However, for the cutoff condition $\beta/k_0 = n_s$, we have $p = 0$, which leads to the cutoff frequency

$$V_c = \begin{cases} \tan^{-1}\sqrt{a} + m\pi & \text{for TM mode} \\ \tan^{-1}\sqrt{a/L_2} + m\pi & \text{for TE mode} \end{cases}$$

Since $n_f > n_s > n_c$, we have $L_2 < 1$, so

$$V_c^{\mathrm{TM}} > V_c^{\mathrm{TE}}$$

that is, the cutoff frequency for the TM mode is larger than for the TE mode.

For $m = 0$,

$$\tan^{-1}\sqrt{a/L_2} > \tan^{-1}\sqrt{a}$$

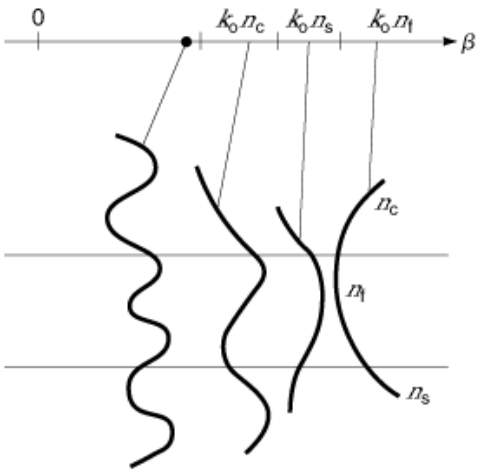

Fig. 42. Modal solutions in β space.

There will be only TE mode, and this is the absolute case of SPSM. When $V_c > V_c^{TE}$, there is no guide mode in the system.

The modal solution in β space is shown in Fig. 42. The essential features of the diagram are:

(1) For $\beta > k_0 n_f$, the field amplitudes are infinite at large distances from the guide, which is unrealistic.
(2) When $k_0 n_f > \beta > k_0 n_c$, there are a discrete set of guided modes. Inside the guide, they vary simultaneously and decay exponentially outside. Thus there is mode confinement and guiding of waves in the film.
(3) When $k_0 n_s > \beta > k_0 n_c$, the solutions vary exponentially in the cover and cosinusoidally in the guide and substrate. Since they fully penetrate the substrate, they are called *substrate modes*.
(4) When $k_0 n_c > \beta$, the solutions are cosinusoidal in all three layers. Under this condition the field patterns are known as *radiation modes*, because the guide radiates power into the cover and substrate regions.

The number of confined modes depends on the values of the refractive indices of the layers and the thickness of the film region.

Metal-Clad Waveguides. Metal-clad waveguides are efficient polarizers and are used in rotation sensors, directional couplers, etc. There exists large differential attenuation between TE and TM modes. The metal cladding is also used for applying electric or magnetic fields to the optical waveguide.

The cross section of a metal-clad waveguide is shown in Fig. 43. The attenuation characteristic as a function of buffer layer width is given in Fig. 44. Depending on the refractive index and width of the buffer, the attenuation passes through a resonance peak for the TM mode, while for the TE mode the attenuation decreases, first slowly and then rapidly, with increase in width.

Periodic Waveguides. In periodic waveguides, either the thickness or the refractive index or both vary periodically along the direction of propagation. Some important devices, such as distributed Bragg and distributed feedback lasers, mode convertors, input–output couplers, and wavelength filters in integrated optics, can be realized with periodic structure waveguides.

If the surface of a planar waveguide is corrugated by etching through a patterned mask, we get a phase grating for the guided wave. The resulting changes in thickness of the guide layer give rise to periodic variation

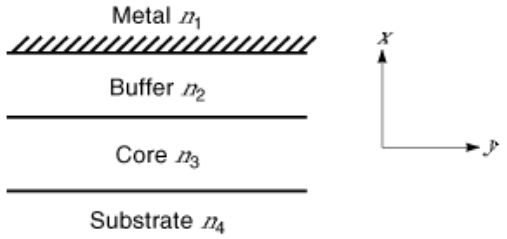

Fig. 43. Metal-clad waveguide.

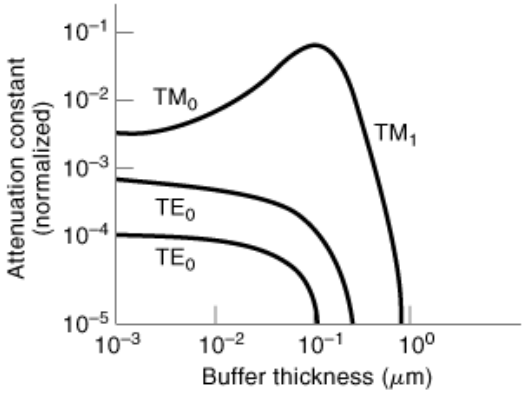

Fig. 44. Attenuation constant versus buffer thickness for a metal-clad waveguide.

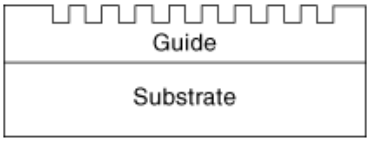

Fig. 45. A corrugated grating waveguide.

of the effective refractive index (Fig. 45). Other applications of periodic waveguides are input–output couplers and mode converters.

Channel (Rectangular-Core) Waveguides. Channel waveguides are three-dimensional waveguides. The substrate is planar, but arrangement is made to confine the field in both x and y directions. The cross sections of three different types of channel guides; are shown in Fig. 41(d).

A *buried* channel guide is one in which the guide is just below the surface of the substrate. Diffusion is used for fabrication of such a guide; for example, titanium metal can be diffused into lithium niobate ($LiNbO_3$) in the form of a well-defined strip, and the guide then placed in a furnace at about 1050°C for 8 h. This is called the Ti:$LiNbO_3$ process. The change in refractive index due to this process is typically $\Delta n \approx 0.01$. Ion implantation may also be applied in the formation of channel guides He^+ implantation has been found reasonably successful in $LiNbO_3$.

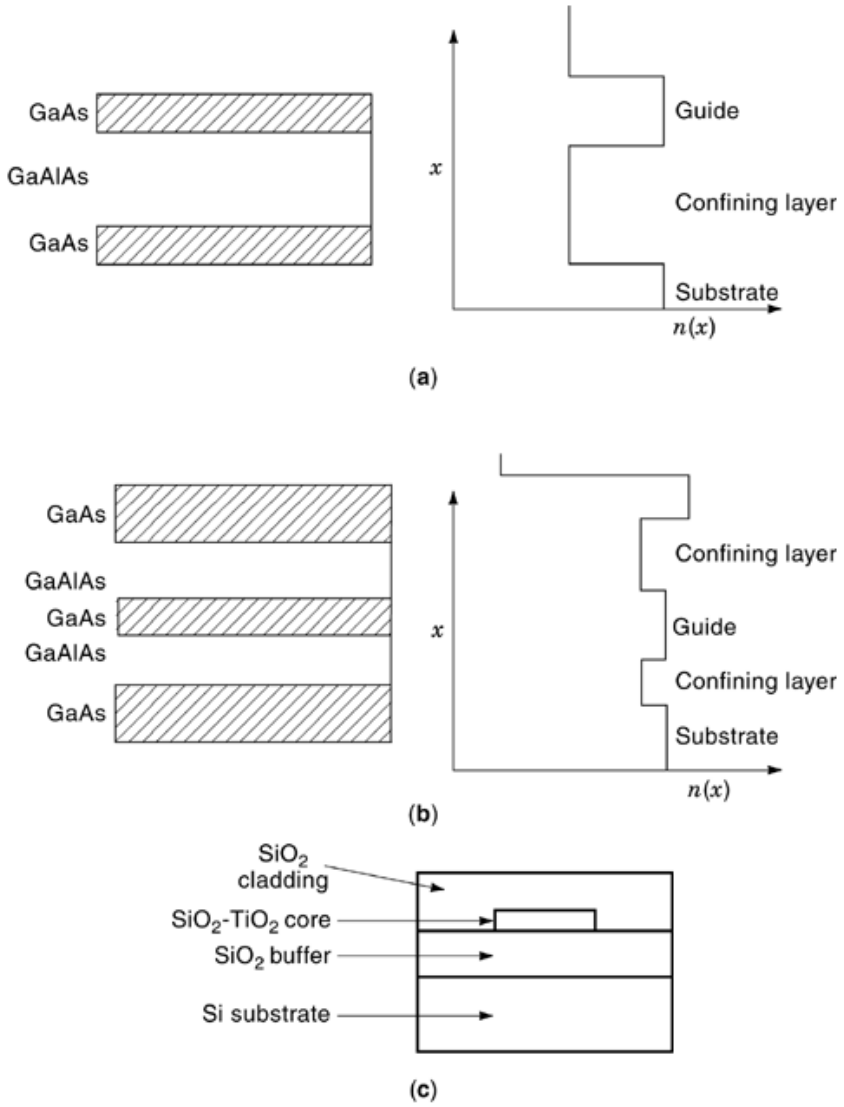

Fig. 46. GaAs–GaAlAs planar waveguide: (a) single heterostructure, (b) double heterostructure, (c) silica-on-silicon waveguide.

A *ridge waveguide* (Fig. 46) is a step-index structure, also fabricated from a planar guide. Total internal reflaction takes place at the side of the guide, and a larger index difference is possible in a ridge waveguide than in a buried channel guide.

A ridge waveguide can be made of semiconductor materials. There may be different combinations of heterostructure materials using III–V compound semiconductors. The GaAlAs/GaAs system is one common combination, GaAlAs being lattice-matched to the GaAs substrate on which it is grown. For $Ga_{1-x}Al_xAs$, where x is the mole fraction, the refractive index n varies nearly linearly with x from $n = 3.57$ for $x = 0$ to

$n = 3.36$ for $x = 0.35$ (near infrared region). The change in refractive index between layers due to change in x yields the necessary guiding layer. Etching is done to form the narrow rib or ridge structure [Fig. 46(a)].

Similarly, a double heterostructure planar guide also may be grown, which has a low-index confining layer of GaAlAs on both sides of the guide [Fig. 46(b)]. This is used in laser structures, as the difference in bandgap between the two materials provides both carrier and optical confinement.

The refractive index also varies with carrier concentration, as

$$\Delta n = -q^2\lambda^2 N_D/8\pi\varepsilon n m^* c^2$$

where N_D is the donor density and n is the free electron density. Undoped GaAs may be grown on the top of a n-doped substrate to form a planar homostructure planar guide. However, increased doping concentration will lead to additional propagation loss.

Siliconoxynitride, Porous Silicon, and Silicon-on-Insulator Waveguides. Ridge guides may be made with amorphous Si materials, which are promising for VLSI technology. Silicon oxynitride ($n \approx 1.5$) is grown on a SiO_2 buffer ($n = 1.47$), which in turn lies on a Si substrate. The SiO_2 here acts as a spacer. In the strip-loaded guide two-dimensional confinement is achieved in a three-layer structure where a strip is formed on a planar layer and substrate. Due to the loaded strip, the effective index becomes larger than in the adjacent surroundings.

Siliconoxynitride (*SiON*) can have a wide range of refractive indices, varying from 1.45 (SiO_2) to 2.0 (Si_3N_4). This allows SiON to be used for various optical integration schemes. $LiNbO_3$ and III–V semiconductors are useful for high-speed electro-optic devices, but SiON can be used for passive and thermo-optically or opto-optically driven devices. For waveguide layer deposition, plasma-enhanced chemical vapor deposition (*PECVD*) and low-pressure chemical vapor deposition (*LPCVD*) are used.

Special-purpose waveguide structures using SiON include electro-optic modulators, adiabatic TE–TM mode splitters (polarization splitters), second harmonic generators (SHGs), and linear and nonlinear Mach–Zehnder interferometers (MZIs).

Porous silicon (*PS*) is another attractive silicon material that has important applications in optical waveguiding. The refractive index of PS varies with the porosity, and the degree of porosity is dependent on the anodization parameters. With the resulting ability to control the refractive index, PS is used for optical waveguiding either as a cladding layer between the silicon substrate and the guiding layer or as a guiding layer itself. The losses are large when PS is used as a cladding layer. It is more attractive for use as a guiding layer, because of its lower losses ($\approx$ 4 dB/cm) and greater degree of flexibility in waveguide design. PS as a waveguide can cover wavelength ranges from visible to infrared. It is thus very promosing in OEICs for developing components like splitters and couplers.

There are also silicon-on-insulator (*SOI*) waveguides and Si–$Si_{1-x}Ge_x$ waveguides (where x is the mole fraction and $x \leq 0.15$). SOI waveguides are made with a thick silicon guiding layer for better mode matching with optical fiber. Since there is a large contrast in refractive index between the Si core and the SiO_2 and air cladding layers, SOI waveguides are basically multimode. The large index contrast produces significant TE–TM waveguide birefrigence. SOI waveguide has also been used in polarization-insensitive, arrayed waveguide grating (AWG) demultiplexing.

The Si–$Si_{1-x}Ge_x$ slab waveguide is a single-mode waveguide. With the development of ultrahigh-vacuum chemical vapor deposition (*UHV CVD*) it is possible to produce $Si_{1-x}Ge_x$ waveguides in large numbers in a single growth. $Si_{1-x}Ge_x$ waveguides are cheaper than SOI waveguides, and in them one can fabricate monolithically such components as p–i–n photodetectors and optical modulators. A strained $Si_{1-x}Ge_x$ waveguide is capable of guiding waves in the range of 1.31 μm to 1.55 μm. However, the technology for $Si_{1-x}Ge_x$ waveguides is still in the development stage.

Silica-on-Silicon Waveguides. Silica-based planar lightwave circuits (*PLCs*) are currently of much interest because of their low insertion loss and their high reproducibility and reliability. Also, hybrid integration is possible with silica-on-silicon (*SOS*) PLCs. They are attractive for application in wavelength division multiplexing (*WDM*), directional couplers, splitters, optical switches, etc. SOS waveguides can be fabricated by applying techniques like CVD, flame hydrolysis deposition (*FHD*), or electron beam deposition (*EBD*).

The structure of the waveguide is shown in Fig. 46(c). It is a combination of three layers deposited on a silicon substrate. The device is a single-mode planar silica waveguide. Different dopants like Ti, B, Ge, or P are used for variation of the refractive index. The core is made of SiO_2–TiO_2. For optical confinement the refractive index of the core is slightly higher, and $\Delta n = 0.7\%$ over the cladding layer. A Ge-doped layer shows a higher refractive index. The buffer layer has the same refractive index as the cladding layer. This isolates the fundamental mode from the silicon substrate and prevents leakage through the silica–substrate interface. To produce the waveguide pattern in the resist material, photolithography is used to produce a mask for subsequent reactive ion etching (*RIE*). Lastly the cladding layer of SiO_2 is deposited on the waveguide. The core and cladding layer thicknesses are 3 μm to 8 μm.

SOS planar waveguides have tremendous prospects in optical fiber communication systems and integrated optics.

Optical Amplifiers

Optical amplifiers are used to amplify an optical wave during its transmission through a fiber. They are placed at regular intervals along a fiber link to obtain linear amplification of the transmitted optical signal. They are also used as preamplifiers in optical receivers, as optical gain blocks, and as optical gates, pulse shapers, and routing switches, when used in a nonlinear mode.

There are two types of optical amplifiers, namely, the semiconductor laser amplifier (*SLA*) and the fiber amplifier. Both types provide high gain over different spectral bands.

Semiconductor Laser Amplifier. The SLA has both linear and nonlinear modes of operation and is basically the same as the conventional laser in structure. However, in the SLA, the facet reflectivities are reduced by 60% to 70% from those in the laser mode, which reduces the optical feedback. There are the resonant or Fabry–Perot amplifier (*FPA*), biased below oscillation threshold; the traveling-wave amplifier (*TWA*), a single-pass device; and the injection lock laser amplifier (*ILLA*), designed to oscillate at the incident signal frequency. The devices provide high internal gain ($\approx$25 dB to 30 dB) with low power consumption. They are compatible with single-mode fiber. The optical gain of these amplifiers depends on the frequency and the intensity of the incident signal. The amplifier cavity gain of a SLA is given by

$$g(f) = \frac{(1 - R_1)(1 - R_2)g_0}{(1 - \sqrt{R_1 R_2}g_s)^2 + 2\sqrt{R_1 R_2}g_s \sin^2 \theta}$$

where R_1 and R_2 are the facet reflectivities, g_s is the single-pass gain, and θ is the single-pass phase shift given by

$$\theta = \frac{\pi(f - f_0)}{\delta f}$$

f_0 and δf being the Fabry–Perot resonant frequency and the free spectral range of the SLA.

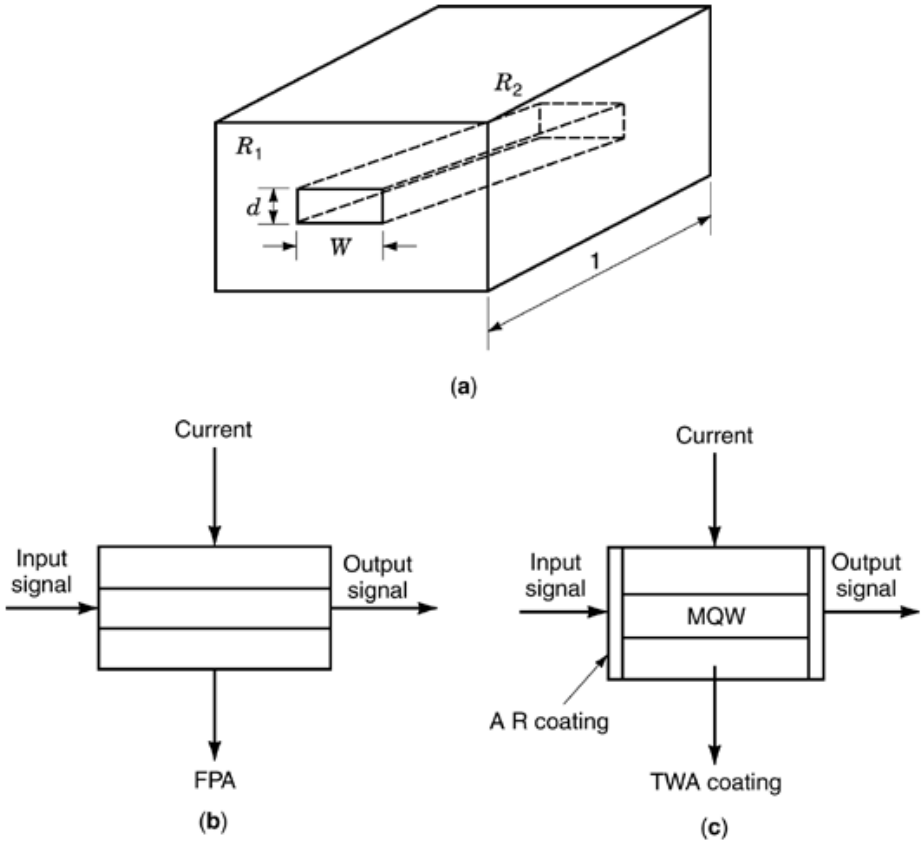

Fig. 47. (a) Semiconductor laser amplifier, (b) Febry-Perrot amplifier structure, (c) Traveling wave amplifier structure.

The schematic structure is shown in Fig. 47(a), where w, d, and l are the active region width, thickness, and length respectively. The facet reflectivities are R_1 and R_2 at the input and output ends. The device is same as the conventional laser with gain or index guiding. In FPA operation R_1 and R_2 are 30% and the device is biased below normal lasing threshold current. For TWA, antireflection coating using silicon oxide or silicon nitride is applied to the facets to reduce the reflectivities at the ends by a factor of 10^{-3} to 10^{-4} [shown in Fig. 47(b, c)]. An ideal TWA is supposed to have zero reflectivities. However, in practice, residual reflectivities $\sim 10^{-4}$ remain at a wavelength of 1.5 μm, and such a device may be referred to as a *near-traveling-wave amplifier* (*NTWA*). The FPA can have a gain around 30 dB when operated at a wavelength of 1.3 μm to 1.5 μm. The gain–bandwidth product is about 40 nm for an InGaAsP laser amplifier; for a MQW amplifier it is larger than 200 nm. The SLA has a typical noise figure $\approx$7 dB. The coupling loss for the SLA is about 3.5 dB/facet. So the actual maximum gain of a wideband SLA is around 20 dB.

The FPA is used for nonlinear applications such as pulse shaping and bistability, due to its dependence on bias current, temperature, and signal polarization. The TWA is superior to the FPA in that it is less sensitive to fluctations in bias current, temperature, and polarization of the signal. Also, its reduced reflectivity increases the lasing threshold current.

A typical output light characteristic of a SLA as a function of current is shown for different facet reflectivities in Fig. 48(a), which indicates that a decrease in facet reflectivity increases the lasing current significantly.

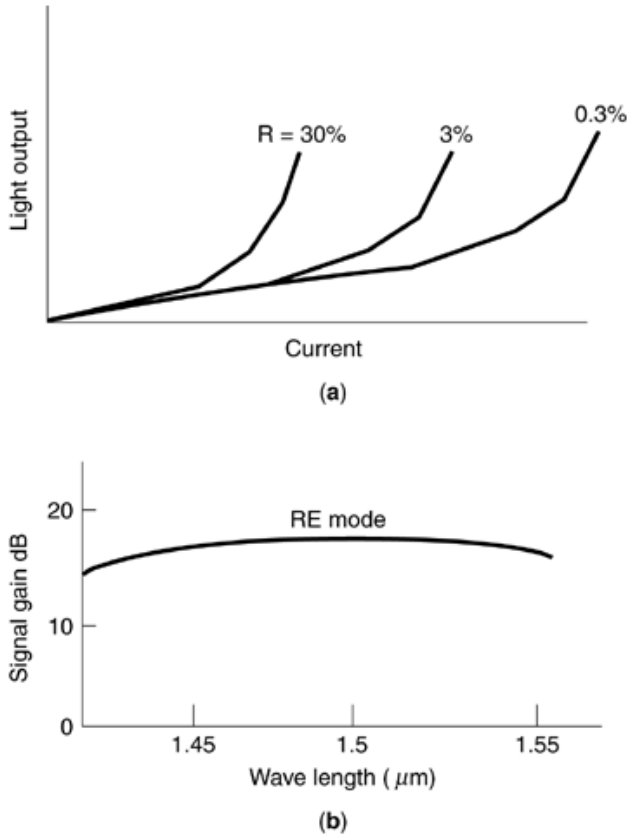

Fig. 48. (a) Output light characteristics of SLA. (b) Gain versus wavelength of SLA.

Wide spectral bandwidth ($\approx$ 50 nm to 70 nm) is obtained in the TWA with high-quality antireflection coating. However, the narrow spectral width of the FPA results in noise filtering. A typical plot of amplifier gain versus wavelength is shown in Fig. 48(b) for the TE mode with facet reflectivity 10^{-4}. The gain modulation or peak–trough ratio, which depends on the facet reflectivities, should be small (less than 3 dB). Several channels can be amplified simultaneously by the optical amplifier if the carrier frequency lies within the passband of the amplifier. However, due to nonlinear effects, there is interchannel cross talk. Two such important phenomena are cross saturation and four-wave mixing (FWM). The noise power is also a function of the facet reflectivity.

Fiber Amplifier. With the advent of single-mode fiber, the fiber amplifier plays a significant role in communication systems. There are three types of fiber amplifiers, namely, the rare-earth-doped fiber amplifier, the Raman amplifier (RA), and the Brillouin amplifier (BA). The fiber amplifier covers a wide range of wavelengths from visible to far infrared (up to 2.8 μm). Rare-earth-doped fiber amplifiers may be doped with ions like erbium, neodymium, thulium, holmium, yitterbium, and samarium. Amongst them, the erbium-doped fiber amplifier (*EDFA*) is most attractive because of its good amplification at 1.55 μm wavelength, where the attenuation curve exhibits a minimum. The Raman and Brillouin amplifiers are based on scattering of photons from higher energy to lower energy, resulting in an optical phonon in the case of a RA and an acoustic phonon in the case of a BA.

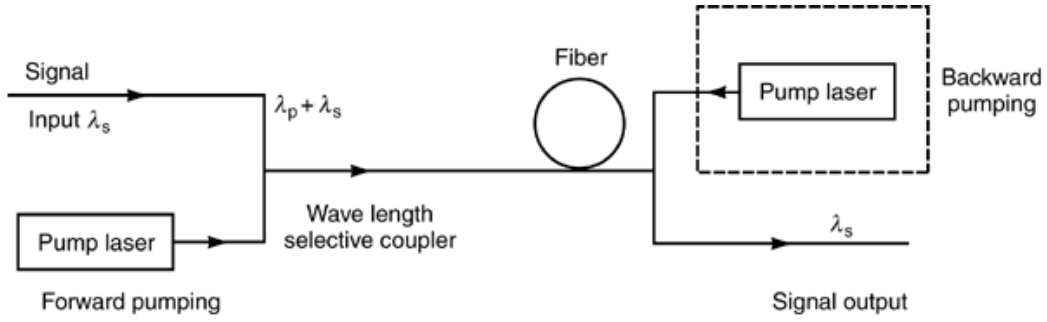

Fig. 49. Schematic of erbium doped fiber amplifier.

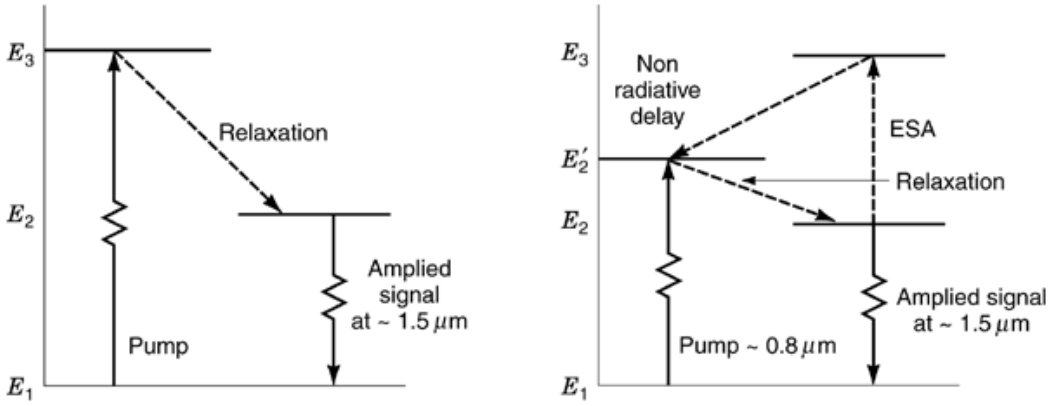

Fig. 50. (a) 3-level lasing scheme with Er^{3+} doping. (b) Excited state absorption.

Fiber amplifier technology has progressed rapidly in recent years. It can be spliced into the system fiber with a low loss, in contrast with the high coupling loss of the SLA.

Rare-Earth-Doped Fiber Amplifier. Though different rare earth ions can be used for doping the fiber to be used as an amplifier, most interest has been centered on the EDFA, because of its convenient optimal wavelength. It has high gain (of the order of 30 dB to 40 dB) with low noise and sufficiently high optical power (from 50 mW to 100 mW). The basic EDFA consists of a pump laser along with sufficient length of erbium-doped fiber and wavelength-selective coupler, which combines the pump and signal wavelength, as shown in Fig. 49.

Practical pump wavelengths of importance are 807 nm, 980 nm, and 1480 nm. When pump and signal are at the same end of the amplifier, they propagate along the fiber in the same direction, and when the two are at opposite ends of the fiber amplifier, they propagate in opposite directions. The amplification depends on the material gain. Thus the optimum fiber length is strongly dependent on input signal and pump power, material doping, and pumping wavelength and may be from a few meters to 100 m. With low doping the length may extend to the order of kilometers.

The gain of the EDFA is limited by the excited-state absorption (*ESA*) phenomenon shown in Fig. 50(a, b) for an Er^{3+}-doped Si fiber laser. The three-level lasing scheme provided by Er^{3+} doping is shown in Fig. 50(a), and the ESA phenomenon in Fig. 50(b), where electrons decay nonradiatively at the intermediate

level, reducing the pumping efficiency. The effect of ESA is improved by the following means:

(1) Codoping the Er^{3+} silica fiber with other materials like phosphorus pentoxide.
(2) Pumping the fiber amplifier at a wavelength that does not cause population at the excited state. ESA is present at ≈ 0.8 μm pump wavelength, but efficiency is improved at wavelengths 0.98 μm, and 1.48 μm.
(3) Using another glass as a host in place of silica, such as fluorozincronate multimode fiber with Er^{3+} doping, which is pumped at 0.488 μm, resulting in gain at 1.525 μm.

Forward pumping results in lower noise and lower light-to-signal conversion efficiency η than backward pumping. For example, in the case of forward pumping the noise figure is ≈ 4 dB to 5 dB with $\eta \approx 40\%$ to 50%, while for backward pumping it is ≈ 6 dB to 7 dB at $\eta \approx 60\%$ to 70%. From the performance point of view EDFA is competitive with the SLA in bandwidth, gain, and power. Further, it shows some additional advantages over the SLA: (i) lower noise figure, (ii) reduced cross talk in the presence of several wavelengths, (iii) compatibility with remote optical pumping, and (iv) greater stability. However, large size and difficulty with integration are two weak points of EDFA.

An EDFA codoped with Yb^{3+} as a sensitizer at 1.5 μm wavelength has the advantage over the ordinary EDFA that the pump absorption band is broader (from 800 nm to 1080 nm). Using a 3 W AlGaAs laser diode, the maximum small-signal gain is 47 dB, a fall of only 4 dB. Such a high-power optical amplifier, used with a single transmitter, can serve 20,000 subscribers.

In contrast with these pumped amplifiers, the distributed EDFA (*DEDFA*) uses Er^{3+} doping throughout the transmission fiber, which is useful in long-haul soliton communication systems. In an all-optical transmission system based on distributed amplifiers one can use 100 km separation between the amplifiers, as opposed to 30 km for lumped amplifiers. The bit error rate (*BER*) is reduced by 4 dB by transmitting through DEDFA over 9000 km, in comparison with lumped amplifiers.

Raman Amplifier. Stimulated Raman scattering (*SRS*) is the source of amplification in a fiber RA. This causes energy transfer from the pump to the signal. Standard single-mode optical fiber can be used for Raman amplification. However, special fiber designs are used to enhance the performance of the amplifier. The Raman shift is obtained by injecting a high-power laser beam into undoped or doped optical fiber, utilizing the vibrational spectrum of the core material. Raman amplification can occur at any wavelength if a suitable laser is available as a pump. The RA exhibits self-phase-matching between pump and signal, and also has a high speed of response and large gain–bandwidth product (GBW). The latter is an attractive feature of the RA for use in WDM systems.

Both forward and backward pumping are possible in RAs, as in EDFAs. The gain of a RA for a 100 km single-mode fiber is $\approx$5 dB at 1.55 μm wavelength with a pump power of 100 mW. The gain of an RA can be estimated theoretically using the relation

$$G_{\mathrm{RA}} = \exp\left(\frac{g_{\mathrm{RA}} P_{\mathrm{P}}}{k} \frac{1 - \exp(\alpha_{\mathrm{p}} L)}{\pi \alpha_{\mathrm{P}} r_{\mathrm{eff}}^2}\right)$$

where r_{eff} is the effective core radius, g_{RA} is the gain coefficient, k is the polarization scrambling factor ($k = 2$ for conventional single-mode fiber under complete polarization scrambling), α_{P} is the transmission loss in the fiber, and L is the fiber length. $\mathrm{P_p}$ is the pump power.

Continuous amplification along the fiber is possible in the RA, and hence the signal is never too low. Also, it is bidirectional and offers high stability. The RA is insensitive to reflections, and the spectral range of its gain can be chosen continuously over all the optical wavelengths of interest. Also, the saturation optical power is large, as it is pump-power-dependent. A Raman power amplifier with a short length (a few kilometers) of a given fiber and of optimum wavelength can be made with an optimum pump power. However, a RA needs a high laser pump power ($\approx$ 100 mW to 200 mW), higher than that of EDFA and SLA.

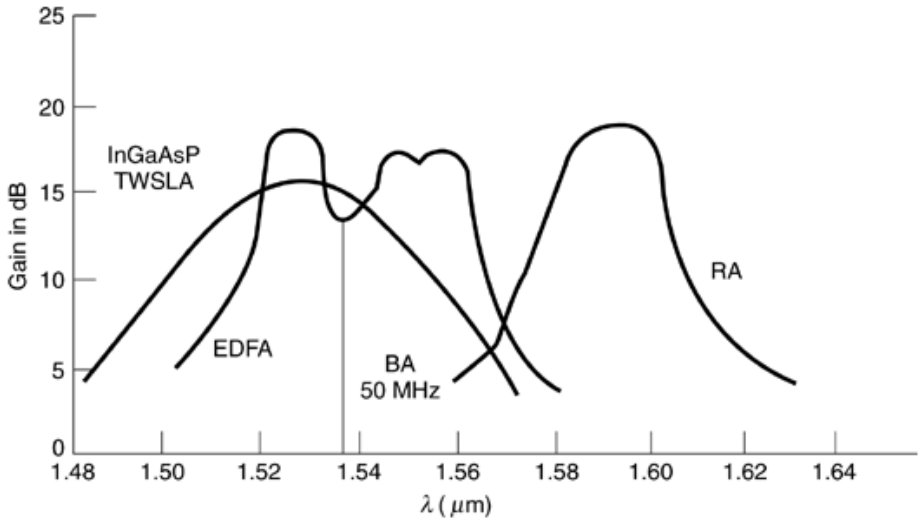

Fig. 51. Typical gain versus wavelength for different optical amplifiers.

Brillouin Amplifier. The BA is based on stimulated Brillouin scattering, which involves emission of acoustic phonons. A pump photon, through the Brillouin scattering mechanism, creates a signal photon and excites an acoustic photon. The pump beam is scattered by the acoustic wave moving through the fiber at the speed of sound. In the BA the amplification occurs in back pumping. The gain spectrum is very narrow, with bandwidth less than 100 MHz. The available bandwidth is due to the thermal distribution of phonons in the core material of the fiber. The ratio of the pump to the signal frequency in stimulated Brillouin scattering is three orders of magnitude less than in SRS. For 5 mW pump power, a gain in the BA of the order of 25 dB can be obtained.

Due to its extremely narrow bandwidth, the BA has restricted applications. It requires narrowband lasers (100 MHz) for both signal and pump.

A typical gain-versus-wavelength spectrum for the three fiber amplifiers, along with a semiconductor laser amplifier, is shown in Fig. 51. The figure shows a large GBW for the EDFA and RA, and a smaller one for the SLA. The BA has very small GBW compared to other three amplifiers. The wavelength varies from 1.50 μm to 1.60 μm for all the amplifiers. A comparison of optical amplifiers is given in Table 2.

Multiplexing

Multiplexing is an important aspect of communication systems. It is the process by which several transmitting signals are combined at the transmitting end and also separated at the receiving end (demultiplexing). The parameters utilized for distinguishing one signal from the other in transmission and reception are the time, frequency, space, and wavelength of the signal. The corresponding multiplexing systems are called time division multiplexing (*TDM*), frequency division multiplexing (*FDM*), space division multiplexing (*SDM*), and WDM. The TDM and FDM systems are commonly used in microwave and digital communication. SDM is not popular for technical reasons. In optical communication, WDM, optical TDM (*OTDM*) and optical FDM (*OFDM*) are commonly employed.

Wavelength Division Multiplexing. The scheme for WDM is shown in Fig. 52. A number n of peak optical signals with wavelengths $\lambda_1, \lambda_2, \lambda_3, \ldots, \lambda_n$ are being transmitted together with the help of a multiplexer

Table 2. Comparison of Optical Amplifiers

Parameter	Value			
	EDFA	RA	BA	SLA
Electrical bias current (mA)	>100	>500	< s50	50
Operating wavelength (μm)	1.525–1.565	Subject to pump	Any (subject to pump)	Any
Unsaturated device gain (dB)	>20	5–15	>25	>20
Pump power (mW)	20–50	100–200	<10	NA
Pump wavelength (μm)	0.82,0.92, 1.4–1.5	Stroke shift below signal	Stroke shift below signal	NA
Bandwidth (nm)	10–40	20–40	0.001	20–50
Coupling loss (dB)	<1	<1	<1	5–6
Saturated Output	A few mW	Limited by pump power	Limited by pump power	A few mW
Polarization sensitivity	A few dB	0	0	0
Noise	Low	Very low	Very low	Low
Directions	Bidirectional	Bidirectional	Unidirectional	Bidirectional

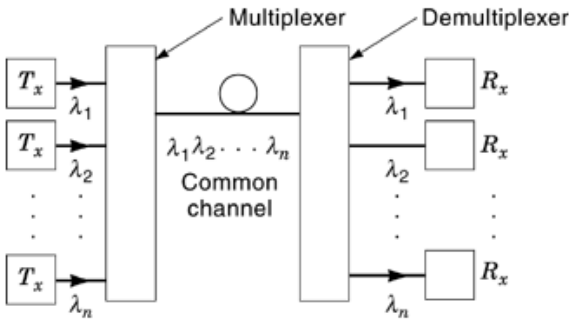

Fig. 52. Schematic diagram for basic principle of wavelength division multiplexing.

through a single optical fiber. These wavelengths may be derived from a set of lasers and are modulated. The multiplexer consists of a set of optical filters arranged in cascade. These filters may be optical directional couplers or mode conversion filters or Bragg gratings. Thus all the n channals are combined into a single output without any loss of power and transmitted through the fiber. At the receiving end, the demultiplexing system consists of similar components and separates the wavelengths of the channel.

The directional coupler filter is made of two dissimilar parallel dielectric waveguides in close proximity. These are structurally similar but differ in core diameter and width and in refractive index. Their shape also

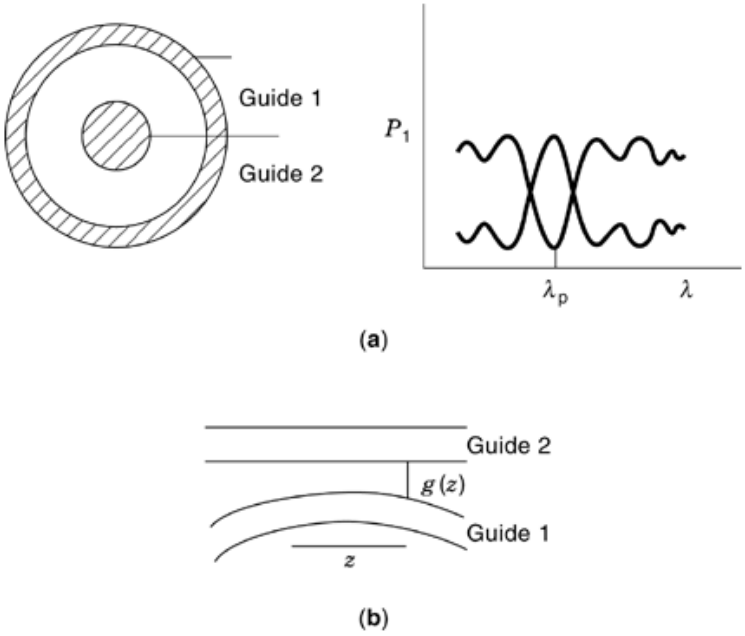

Fig. 53. (a) Cross section of a coaxial fiber coupler and plot of dispersion characteristics. (b) Directional coupler with tapered coupling.

may be different. The optical directional coupler may consist of both passive and active devices. A typical coaxial fiber coupler is shown in Fig. 53 along with a typical filter response. The coupler works as a bandpass filter and cross-couples significant power only in the vicinity of the synchronous wavelength λ_p. The typical filter bandwidth is around 100 Å using Ti:$LiNbO_3$ devices. The sidelobes in the simple directional coupler filter may be suppressed by using tapered coupling, where the interguide separation varies with distance (shown in Fig. 53).

Mode conversion filters and Bragg grating filters are also used in WDM systems. The grating filter is made by creating periodic corrugation on the surface of a planar waveguide as shown in Fig. 45. The optical path between the grooves is $n_{\text{eff}}\lambda_g$, where n_{eff} is the effective index and λ_g is the groove wavelength. We have

$$n_{\text{eff}}\lambda_g = m\lambda_0$$

by Bragg's law, where m is an integer and λ_0 is the free-space wavelength.

TE–TM mode conversion is also achieved using grating couplers. The filter operation in a mode conversion device depends on the difference in dispersion in two modes, as in the dissimilar-guide directional coupler. Better wavelength selection (around 10 Å) in Ti:$LiNbO_3$ can be obtained in this case, due to the larger differences in the slopes of the two dispersion characteristics with orthogonal modes. A typical mode conversion filter is shown in Fig. 54; it uses periodic electrodes for coupling.

However, the small substrate–waveguide refractive index difference for $LiNbO_3$ devices, combined with inherent etching problems, has limited the development of Ti:$LiNbO_3$ waveguide filters. The InGaAsP/InP grating waveguide is very promising, where the corrugation is done through a photoresist mask using UV beams and etching. A filter bandwidth as small as 6 Å has been obtained in this system. In glass waveguides, in a 1 cm long grating filter, a filter bandwidth as small as 0.1 Å has been achieved.

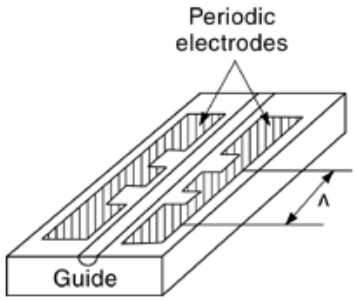

Fig. 54. TE–TM mode conversion filter.

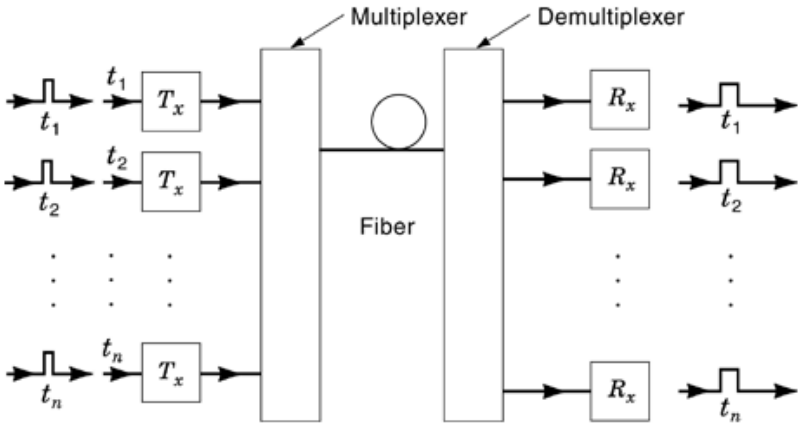

Fig. 55. A simple optical time division multiplexing system.

Since WDM is asynchronous, each user has access to the common channel instantaneously. The process is efficient, as the total wavelength required is approximately n times that of the individual channals.

Optical Time Division Multiplexing. In OTDM, all the users communicate on the same carrier wavelength in specific time slots allowed to them. Channels 1 to n transmit information through a multiplexer, which interleaves the time slots of each channel with uniform overall data rate. At the receiving end the signals are seperated out by a demultiplexer. Synchrony is maintained between transmission and reception. The simplifying and redirecting of data are done in the same sequence as the original interleaving process (Fig. 55).

Channel waveguide switches are used for multiplexing and demultiplexing in an optical time division communication system. The MZI switch on a $LiNbO_3$ substrate is used. The electro-optic property of $LiNbO_3$ is employed in interferometric intensity modulation. A MZI comprises two Y junctions dividing equally the input optical power (Fig. 56), which arrives at the second Y junction without any loss and in phase when no voltage is applied at the electrode. However, with the application of a potential a differential phase change is created between the signals in the two arms, giving rise to interference in the output waveguide. So the phase modulation is converted into intensity modulation. A phase shift π between two arms gives rise to a off state, while the case without voltage at the electrodes represents the on state.

The MZI used for OTDM is a modified version of the one described above. In this case the output is a hybrid X junction instead of a Y junction. It behaves as a 3 dB coupler and functions as a two-way switch. One

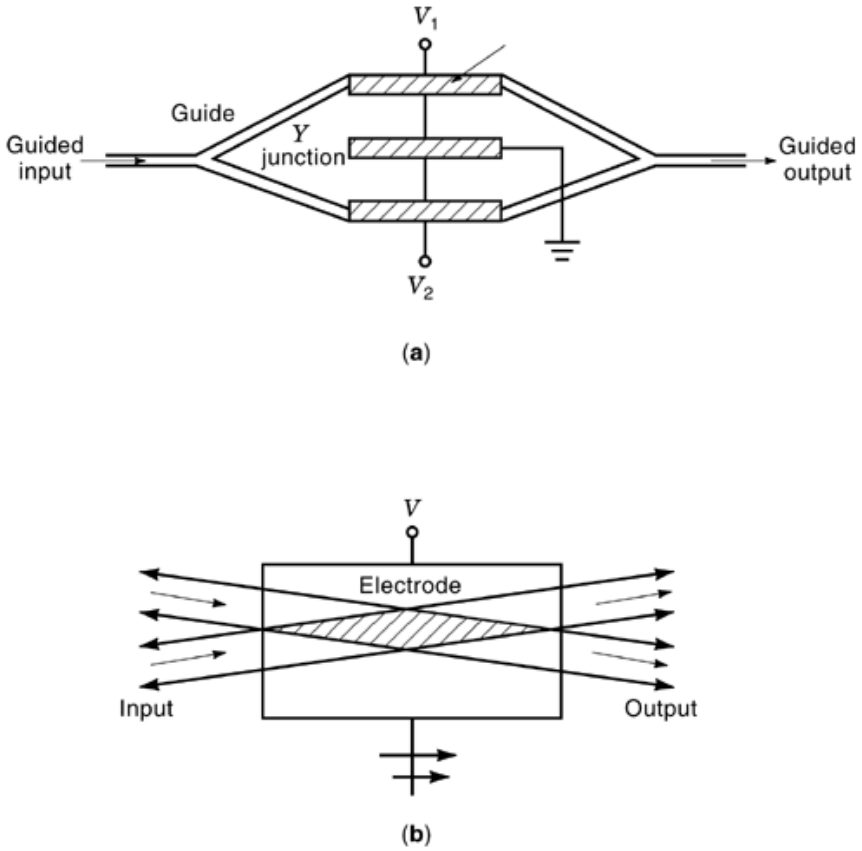

Fig. 56. Mach–Zehnder interferometer using Y junction and X switch.

gets an output from one arm of this switch when the driving voltage is close to zero, and from the other arm when the phase shift between the arms is close to $\pm\,\pi$ rad.

16 Gbit·s^{-1} transmission over 8 km has been demonstrated, in which the optical multiplexing and demultiplexing ratio is 1 : 4 with a baseband channel rate of 4 Gbit·s^{-1}. The system is referred to as a four-channel OTDM system. Also, 10 Gbit·s^{-1} direct intensity modulation and transmission over 100 km has been demonstrated. This uses a high-speed MQW *DFB* (distributed feedback) laser diode and a back-illuminated GaInAs APD.

Optical Frequency Division Multiplexing. Up to 100 or even more different optical channels (carriers) can be simultaneously transmitted in a single fiber by applying OFDM. A tunable local laser along with a good sharp IF filter may be used to select different optical channels at the coherent receiver end. In this system, the best transmission capacity means the largest possible number of closely spaced optical channels and the highest possible rate of each channel. This coherent multichannel transmission is used for medium distances, say 50 km, and so the receiver sensitivity is not a critical parameter; rather, the receiver selectivity is more important. The receiver is a tunable frequency-shift keying (*FSK*) or duplex phase-shift keying (DPSK) heterodyne system, which is used for coherent multicahnnel communication (*CMC*) (Fig. 57).

In WDM it is not possible to use the overall fiber bandwidth effectively. The channel selection is made by a number of optical filters that have broad bandwidth, and only a limited number ($\approx$ 10) of carriers

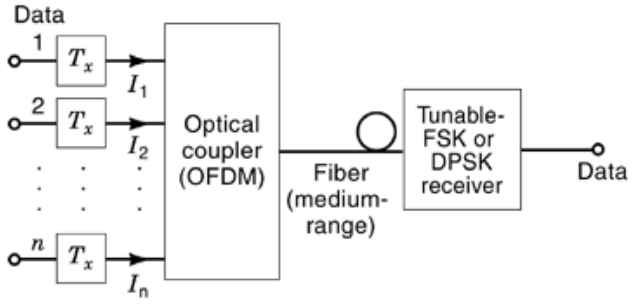

Fig. 57. OFDM with FSK or DPSK heterodyne receiver.

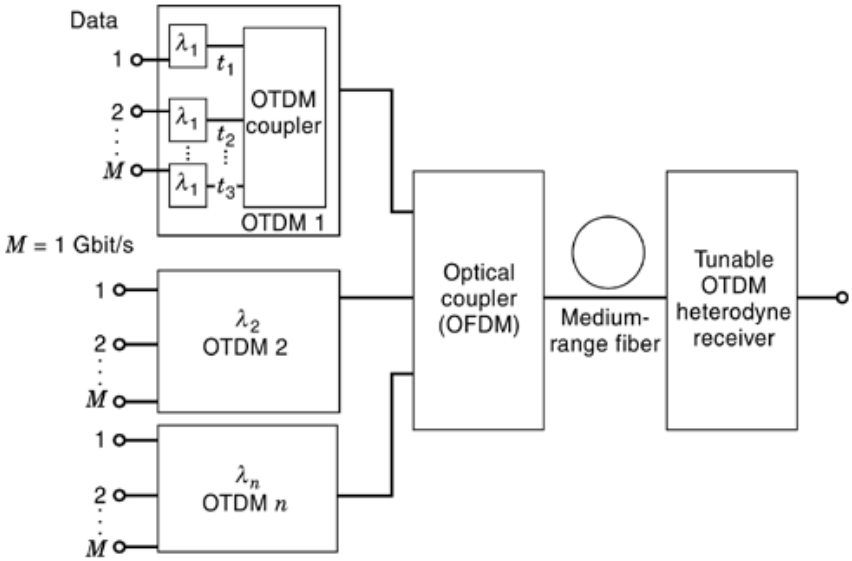

Fig. 58. Multigigabit (1 Tbit/s) data transmission with OFDM and OTDM.

with large channel spacing can be transmitted simultaneously. However, CMC systems with OFDM can use the large fiber bandwidth efficiently. In CMC systems, very high-bit-rate signals (up to terabits per second) can be transmitted in conjuction with OFDM and OTDM. A schematic block diagram is shown in Fig. 58.

Dense Wavelength Division Multiplexing. For high-bit-rate transmission from 2.5 Gbit/s upward, the dense wavelength division multiplexing (*DWDM*) system is used. DWDM is an advance on classical WDM. The latter can transmit a limited number of wavelengths (usually two) through a single-mode fiber. In DWDM the transmission capacity increases by a factor $n = 4$, 16, 32, 64, or 128, depending on the configuration.

Since DWDM systems are used for long transmission links, optical amplifiers have to be used at many points. The optical window used today is 1550 nm to 1610 nm. The reference frequency for DWDM transmission is 193.10 THz with channel spacing 100 GHz.

System Integration

System integration involves integration of electronics and optical components and interconnects. Optics provides several advantages, such as large bandwidth and parallelism. But it does not give input–output isolation as in electronic systems. So optoelectronics (integration of systems using both optical and electronic devices) is accepted today. Further, interconnects are very important in the process of integration, because at very high frequencies (above 1 GHz) the propagation delay due to the *RC* time constant is an important consideration and leads one to prefer information transfer through photons, for which fiber can be used as interconnnects. Optical interconnects provide immunity to mutual interference and cross talk. The large bandwidth of optical fibers ultimately leads to reduction in system size and power and to large fanout.

Two types of integration techniques have been practiced—hybrid and monolithic. In hybrid integration, different discrete devices on separate chips (functional blocks) are interconnected. Hybrid integration lacks compactness and has large parasitic effects.

In monolithic integration two methods are used—vertical integration and horizontal integration [Fig. 59(a)]. In vertical integration, the devices are grown on a conducting layer with a proper isolating layer. However, in this process the coupling between different layers is greater, resulting in larger parasitic effects and inferior performance at high bit rates. In horizontal integration different device components are fabricated on a semiinsulating substrate using regrowth. This is compact and effective in present OEIC systems.

Monolithic Optoelectronic Integrated Circuit Receiver

The monolithic OEIC receiver is of current interest due to its potential application in high-speed optical communication. A block diagram of a photoreceiver system is shown in Fig. 59(b).

The first two blocks together are called the *front-end photoreceiver* (*FEPR*). The integration of FEPRs, has been carried out successfully, and different circuit configurations have been developed. The MSM FET, *p–i–n* junction-FET/MESFET/MODFET, APD FET, and *p–i–n* HBT are successfully operated front-end photoreceivers applied for high-bit-rate reception of optical signals. The technologies used are MBE, organic metal vapor epitaxy, MOCVD, etc., along with the usual liquid- and vapor-phase epitaxy.

The materials are III–V components based on GaAs or InP technology. Below the fabrication process steps and the preformance of a typical monolithic MSM FET front-end photoreceiver are discussed.

In the process flow chart [Fig. 59(c)], the preamplifier components such as MESFETs, Schottky diodes, and feedback resistors are fabricated on an *n*-GaAs layer, and the MSM photodetector is fabricated on the undoped GaAs layer after selectively etching the n^--GaAs. Five masking levels are employed for the fabrication.

(1) The starting material is n–n^- SI GaAs.

(2) The mesa islands are formed using a $NaOH$–H_2O_2 GaAs etchant. This is followed by low-energy B^+ implantation (energy 50 keV, dose 5×10^{11} cm^{-2}) to improve the mesa isolation.

(3) The NiAuGeNi ohmic contacts are formed by resistive or e-beam evaporation and alloying at 430° C for 45 s in N_2 ambient.

(4) The MESFET gates and Schottky contacts of the level-shifter diodes are made, and gate recessing is carried out to control the saturation current of the FET. This is followed by Ti and Au evaporation (300 Å and 1500 Å) and liftoff.

(5) The n^--GaAs layer is selectively etched using wet etching to expose the *n*-GaAs layer for a MSM PD, which is fabricated at the interconnect level using Ti and Au evaporation (300 Å and 2000 Å) and liftoff.

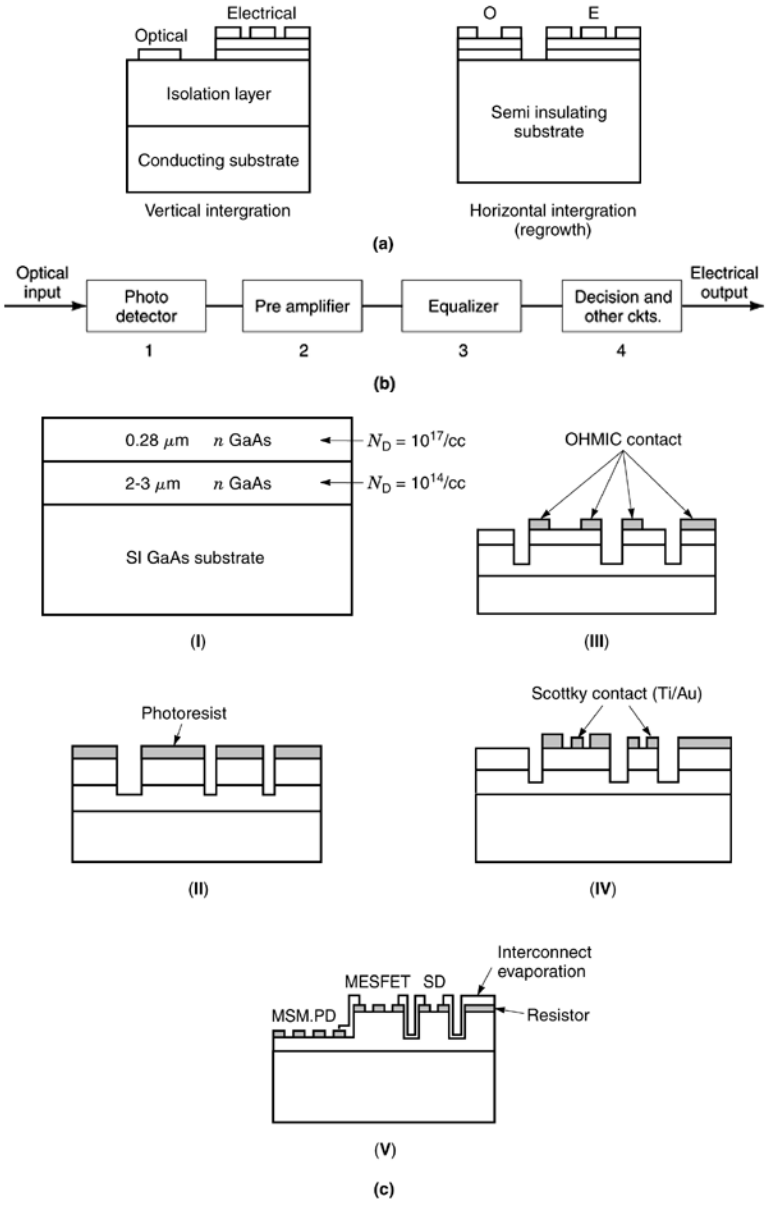

Fig. 59. (a) Vertical and horizontal integration. (b) Block diagram of a photoreceiver system. (c) Different steps for monolithic OEIC receiver.

Wideband monolithic optical receivers generally employ a transimpedance in buffered FET logic (*BFL*) configuration. A common-source amplifier stage is integrated with a source-follower–level-shifter stage. Passive resistors or MESFETs can be used as load to the preamplifier. The BFL configuration with active load is shown in Fig. 60(a). The transfer function, upper cutoff frequency and open-loop voltage gain of the receiver comprising

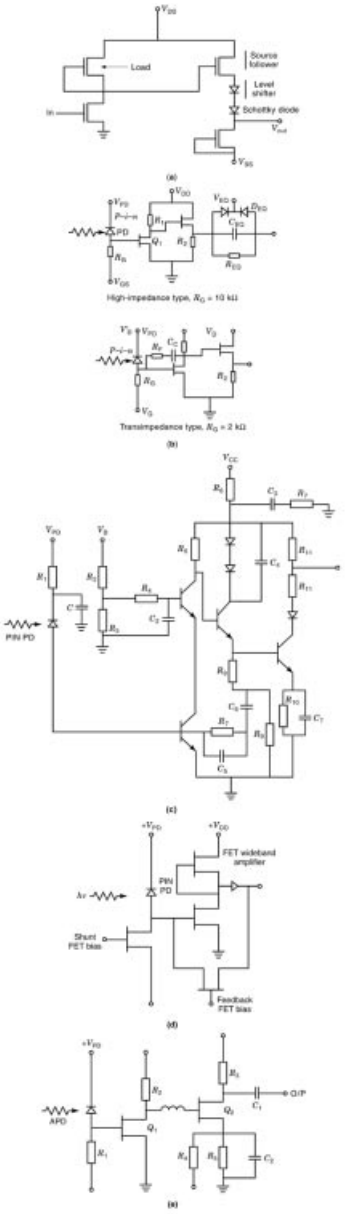

Fig. 60. (a) Buffered FET logic. (b) *p–i–n* MODFET photoreceiver. (c) PIN-HBT photoreceiver circuit. (d) PIN-FET photoreceiver circuit. (e) APD-FET photoreceiver circuit.

the transimpedence preamplifier and BFL circuit can be estimated using the following equations:

$$
\begin{aligned}
H(j\omega) &= \frac{V_{\text{out}}}{I_{\text{in}}} = \frac{R_{\text{T}}}{1 + j\omega C_{\text{T}} R_{\text{T}}/G} V_{\text{out}} \\
f_{\text{c}} &= \frac{G}{2\pi C_{\text{T}} R_{\text{T}}}, \quad G = G_{\text{amp}} G_{\text{buff}} \\
G_{\text{amp}} &= g_{\text{mcs}}\, R_{\text{load}} = \frac{G_{\text{mcs}}}{g_{\text{dcs}} + g_{\text{dload}}} \\
G_{\text{buff}} &= \frac{g_{\text{mcs}} R_{\text{s}}}{1 + g_{\text{mcs}} R_{\text{s}}}
\end{aligned}
$$

where g_{mcs} and g_{dcs} are the transconductance and output conductance of the common-source FET respectively, G is the gain factor, R_T and R_s are the total resistance and source metal resistance, C_T is the total input capacitance, and g_{dload} is the FET output conductance acting as load.

The mean squared total input noise current of the OEIC receiver is contributed by the PD, feedback resistor, and FET and is given by

$$\begin{aligned}\langle i_T^2 \rangle &= 2qI_{ph}I_{p1}B + \frac{4kT}{R_F}I_{p2}B + 2q(I_g + I_D)I_{p2}B \\ &\quad + \frac{16\pi^2 kT\Theta_m}{g_m}(C_T B)^2 \left(f_0 I_f + I_{p3} + \sum_{r=1}^{n} \frac{I_r A_T}{\tau_T} \right)\end{aligned}$$

In this the first term is the noise due to the photocurrent I_{ph}, the second is due to feedback resistance in the transimpedance amplifier, and the third is due to the gate leakage current I_g and photodiode dark current. I_D. The last term is due to flicker noise, channel conductance noise, and noise due to trap centers present in the channel and the buffer regions. I_{p1}, I_{p2}, and I_{p3} are the Personik integrals, and I_f and I_r are the $1/f$ noise and the trap integrals. τ_T is the trap emission time constant. A_T and Θ_m depend on the trap density and materials. F_0 is the noise corner frequency. For low noise, one needs low gate leakage, low dark current, and low total input capacitance. At higher bit rates and frequencies the channel conductance noise is important.

The sensitivity of the receiver is calculated using the relation

$$\eta P = Q\frac{hc}{q\lambda}\sqrt{\langle i_T^2 \rangle}$$

where η is the quantum efficiency, P is the output power, and Q is a parameter dependent upon the BER. For BER $= 10^{-9}$, Q is 6. The signal-to-noise ratio of the photoreceiver is given by

$$\text{SNR} = \frac{M^2 I_0}{2\sqrt{\langle i_T^2 \rangle}}$$

where m is the modulation index for the modulated carrier and I_0 is the dc photocurrent corresponding to a dc input power level P_0.

An InP-based front-end photoreceiver with p–i–n MODFET has also been fabricated. The MODFET is used because it has lower noise figure and noise temperature than other FETs. Further, the InGaAs/InAlAs/InP MODFET is superior to the GaAlAs/GaAs MODFET because of its larger CB edge discontinuity ($\Delta E_c = 0.5$ eV), higher mobility ($> 10^4$ cm^2/V·s), and higher carrier peak velocity in the InGaAs layer. A cutoff > 200 GHz, maximum oscillation frequency > 400 GHz, and noise figure < 1.5 dB with gain > 6.5 dB at W band are typical.

The photoconductor is an InGaAs p–i–n diode. The p–i–n PD and the InGaAs/InAlAs/InP MODFET are grown in horizontal integration using the organo metallic vapor-phase epitaxial (OMVPE) technique. The equivalent circuits of p–i–n MODFET high-impedance and transimpedance receivers are shown in Fig. 60(b). The sensitivity is -30.4 dBm for the high-impedance type and -27.1 dBm for the transimpedance type. The receiver is suited for operation at 1.2 Gbit/s. It shows a leakage current of 10 μA. The dynamic range of the receiver is larger than 23 dB.

A monolithic p–i–n HBT transimpedance photoreceiver has been fabricated using InP/InGaAs heterostructures grown by chemical beam epitaxy (CBE). Implemented with single epitaxial growth, the OEIC

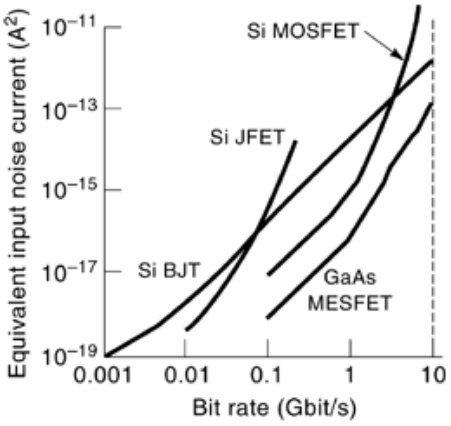

Fig. 61. State-of-the-art performance comparison of Si JFET, Si MOSFET, and GaAs MESFET photoreceivers.

receiver has 3.8 GHz bandwidth with 400 Ω transimpedance. The receiver sensitivity is -18.8 dBm for transmission of 5 Gbit/s at 1.5 μm wavelength. A typical OEIC *p–i–n* HBT receiver is shown in Fig. 60(c). The circuit has a *p–i–n* PD and a transimpedance HBT amplifier followed by a 50 Ω output buffer. The HBT has a cutoff frequency higher than 100 GHz. The power dissipation is 150 mW at supply voltage of 5 V.

The *p–i–n* FET and APD–FET OEIC receivers are also of commercial interest in optical communication systems. The two receiver circuits are shown in Fig. 60(d) and 60(e) respectively. The monolithic *p–i–n* FET optical receiver using a GaAs MESFET and III–V compounds for the PD has been designed for application in the 1.1 μm to 1.6 μm wavelength range. The high-impedance receiver, with 1 MΩ bias resistor, attains its saturation level at an input optical power of 0.5 μW, or -0.33 dBm; for the transimpedance receiver, with 1 kΩ bias resistor, the corresponding power is 0.5 mW, or 3 dBm.

A high-resistivity APD–FET receiver designed to operate at a transmission rate of 8 Gbit/s in the wavelength range 1.3 μm to 1.5 μm has been designed. The receiver used a hybrid GaAs MESFET high-impedance front-end configuration and a InGaAs/InGaAsP/InP APD with 60 GHz gain–bandwidth product. The sensitivity of the receiver is -25.8 dBm for a BER of 10^{-9}.

The high-impedance front-end receiver has a poor dynamic range compared to its transimpedance counterpart. For a transmission rate of 1 Gbit/s the dynamic range is 20 dB to 27 dB for the high-impedance receiver, while it is 30 dB to 39 dB for the transimpedance one.

The *p–i–n* JFET photoreceiver has been realized using InP-based III–V compounds such as InGaAs/InP for use in the wavelength range 1.3 μm to 1.5 μm. The receiver circuit uses six junction FETs (JFETs), five level-shifter diodes, a feedback resistor, and the *p–i–n* PD. The feedback resistor is 300 Ω, and the JFET gate length is 2 μm. The JFET has a cutoff frequency of 3 GHz and a transconductance of 52 mS/mm. The receiver has a gain of 6 dB. A state-of-the-art performance comparison of Si JFET and GaAs MESFET receivers for transmission rates from 1 Mb/s to 10 Gb/s is shown in Fig. 61.

An alternative to the conventional photoreceiver for high-sensitivity and high-speed operation is the use of optical amplifiers (semiconductor laser amplifier, fiber amplifier) as preamplifiers. A schematic block diagram for a SLA *p–i–n* photoreceiver is shown in Fig. 62(a). It needs a filter because of the SLA's bandwidth limitation ($\approx$ 30 nm to 40 nm). A comparison of the SLA *p–i–n* receiver with the APD receiver is given in Fig. 62(b). It shows a significant improvement of the SLA *p–i–n* receiver over the high-performance APD receiver at transmission rates higher than 2.4 Gbit/s. Futher improvement is observed when an EDFA is used (sensitivity is improved by 10.5 dB).

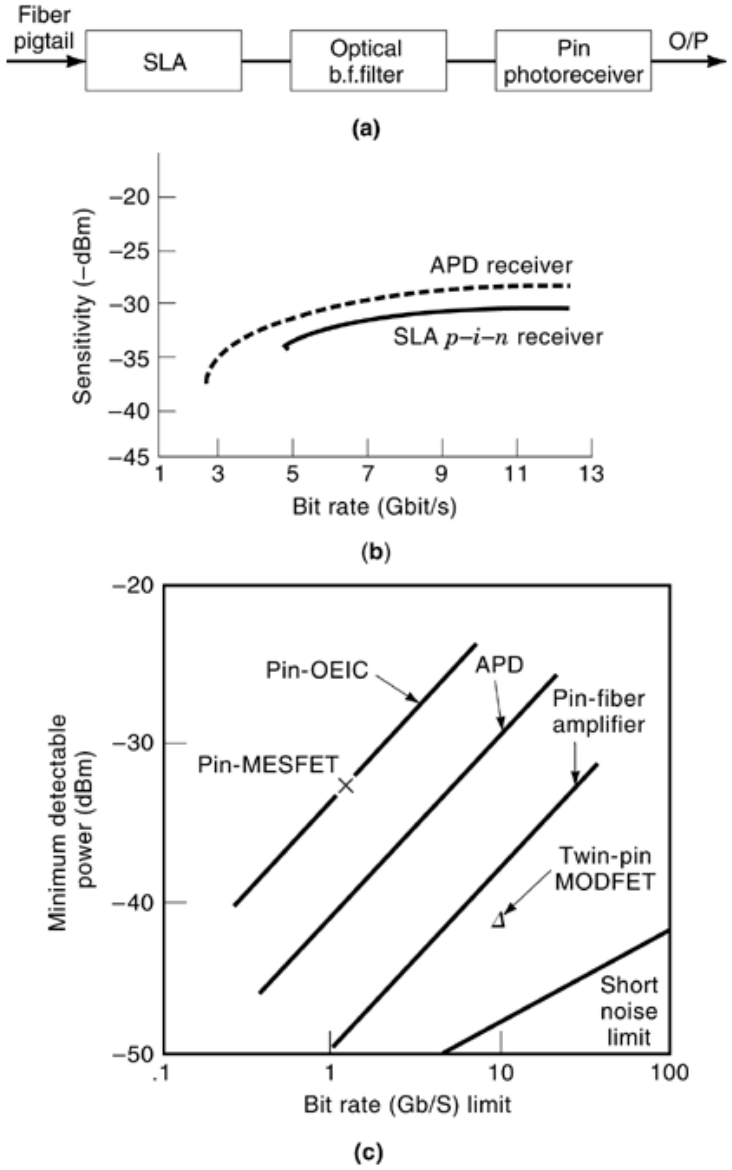

Fig. 62. (a) Block diagram of a SLA-pin photoreceiver. (b) A comparative study of SLA-pin and APD receiver. (c) Overall comparison of different front-end photoreceiver systems.

An overall comparison of different front-end receiver systems is presented in Fig. 62(c). It shows the minimum detectable receiver power (dBm) versus bit rate (Gbit/s) for different devices and technologies. The highest bit rate as well as the lowest detectable power is obtained for the fiber-amplifier *p–i–n* receiver system. The *p–i–n* HEMT filp chip (*FC*) OEIC receiver is equally attractive and has tremendous prospects.

A Monolithic IC Transmitter. The fabrication of OEIC transmitters is more complicated than that of OEIC receivers. An OEIC transmitter consists of a light source, which is high-power LED or LD, along

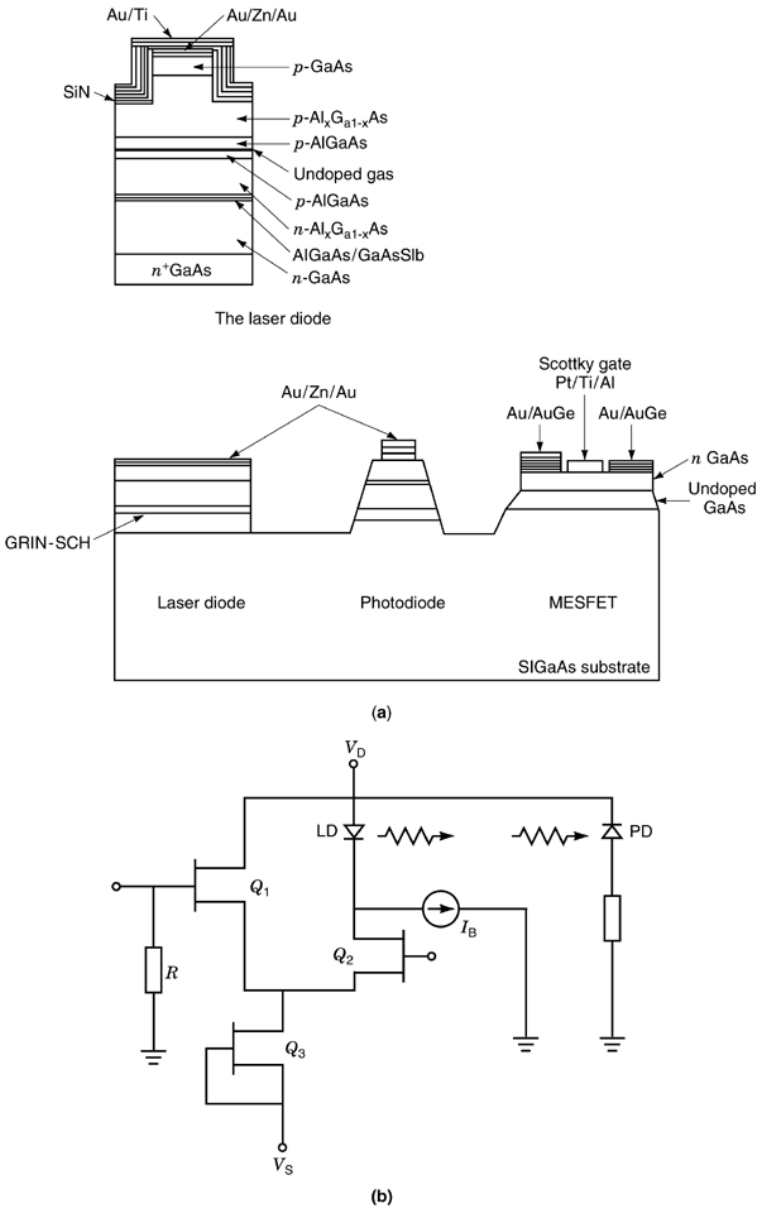

Fig. 63. (a) A cross-sectional view of an integrated transmitter. (b) The OEIC transmitter drive circuit.

with driver circuitry. The processing steps for the associated circuitry of the laser structure are difficult. The electrical and optical confinements in a laser diode are in the lateral dimension. The optical cavity consists of two end mirrors in an edge-emitting laser. Heat sinking for the whole chip also becomes important.

The cross section of an integrated transmitter is shown in Fig. 63(a). The transmitter consists of a laser diode, which may be a single quantum well (*SQW*) or MQW graded-refractive-index separate-confinement heterostructure (*GRIN SCH*) device. Such a LD results in lowest threshold current and good optical confinement.

This is followed by a monitoring photodiode and MESFET. The processing steps are two or three steps of MBE, ion-beam etching, and microcleaving of laser facets.

The GaAs MESFET is used as driver circuit in connection with a PD in a feedback circuit along with the constant-current differential laser. The drive circuit is shown in Fig. 63(b). In a similar type of integration using a GRIN SCH SQW laser and four recessed-gate GaAs MESFETs, a CW threshold current of 15 mA and rise time of 400 ps for operation at 2 Gbit/s has been realized. Further, a more complex transmitter with a MQW laser with photodiode and 12 MESFETs has been fabricated, showing a rise time less than 200 ps.

OEIC transmitters have also been realized on conductive substrates in which a HBT has been integrated with Be-implanted injection laser. A *p–n–p* phototransistor was integrated with a buried heterostructure (*BH*) laser. The collector and base of the transistor are of GaAs, and the emitter of GaAlAs, which is transparent to 850 nm radiation. The electrical connections for the laser cathode and collector are made through the conductive substrate, and the base is connected to it by deep Zn diffusion. The phototransistor responsitivity was 50 A/W to 75 A/W at a collector current of 15 mA to 20 mA.

There has also been realized an InP-based OEIC transmitter for 1.3 μm to 1.6 μm wavelength application, using GaInAsP. A BH laser and a driving circuit consisting of three HBTs have been integrated on an *n*-InP substrate. The fabrication involves growing the active region followed by burying a heterostructure using an etching process. The epilayers of the transistor and the BH laser are grown by LPE. Cleaving is used for the laser facets. The threshold current of the laser is around 20 mA to 30 mA at 1.6 GHz. The HBT acts as both photodetector and drive circuit.

System Integration on a Silicon Chip. Optoelectronic system integration has also been carried out on a silicon chip—for example, waveguides, photodetectors, and VLSI CMOS circuits in one chip. The optical waveguide may be made of silicon nitride or silicon oxynitride deposited on an optical insulating oxide film. Monolithic integration of optical structures and VLSI CMOS circuitry on a silicon chip has been developed with the SWAMI-LOCOS technique, which allows smooth and stepless surfaces. The fabricated test chip developed may contain curvatures, Y branches, couplers, splitters, mirrors, interferometers, etc. as parts of optical components, and photodetectors, amplifiers, logic circuits, etc. as parts of microelectronic circuits. The waveguides and MZIs may be coupled to photodetectors and phototransistors for electro-optical signal transformation.

Optical Computing. An all-optical computing system is the aim of optoelectronics and the OEIC. Parts of the system such as parallel processors, serial-to-parallel converters, shift registers, and switches can be integrated individually, possibly with monolithic input/output devices.

Further alternative nonlinear materials are under investigation for implementation of more complex optical subsystems. Sol–gel reactions, polymers, and organic insulators such as strontium barium niobate, bismuth silicon oxide, and barium titanate are under investigation. Improved material performance will lead to the implementation of all-optical computers.

A simple hybrid optical–electronic microprocessor architecture is shown in Fig. 64(a). The machine, called the *connection machine*, contains a large arrangement of printed circuit boards with 512 processing elements in each of them. The OEIC contains LDs and photodetectors. The switching of interconnecting processes is performed by diffraction gratings. The WDM is used to direct bit streams to the appropriate board.

The AT&T all-optical digital processor has been demonstrated, and a schematic is shown in Fig. 64(b). The processor operates at 10^6 cycles/s. A GaAs/GaAlAs SSEED is used as a bistable switching element. The SSEED offers 10^9 operations/s with a switching energy 1 pJ. An improved version may be made with an InAlAs/InGaAs/InP structure. This will be useful at long wavelengths. The input/output systems utilize fibers and laser beams. Larger device arrays with faster switching along with interconnecting system models will result in superfast all-optical computers.

Future Directions. Tremendous research work is going on in optoelectronics, photonics, and OEICs to meet the new challenges of communication and computation. InP-based OEICs and photonic integrated circuits (*PICs*) on a large scale have already been provided for 16 $\times$ 16 InGaAs/InP imaging arrays consisting

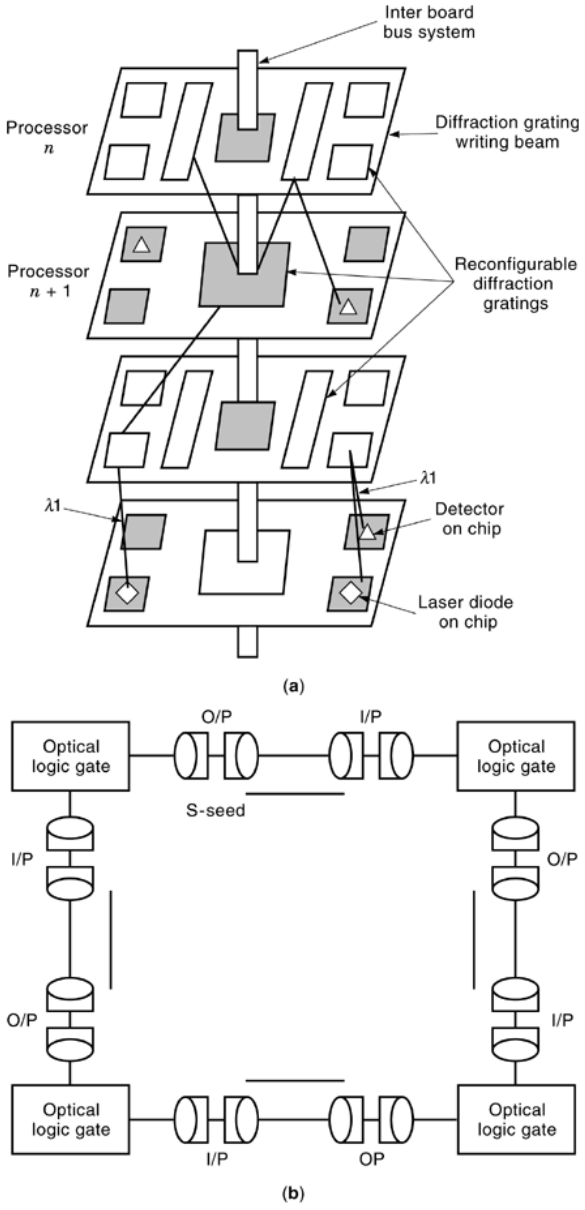

Fig. 64. (a) A hybrid optical/electronic microprocessor architecture. (b) A typical optical processor using SSEED array module optical logic gate.

of 272 JFETs and 256 *p–i–n* detectors. The device yield is over 99%. Realization of large-scale OEICs with more than 500 devices is in progress. The platform integration technology (*PIT*) is based on InP/InGaAs *p–i–n* diodes and JFETs for realization of OEIC receivers such as switchable-photodiode-array transimpedance receivers and heterodyne receivers with balanced photodiodes at the input. These systems can be applied to subcarrier-multiplexed communications, optically controlled phased array radar, low-noise broadband transmission, etc.

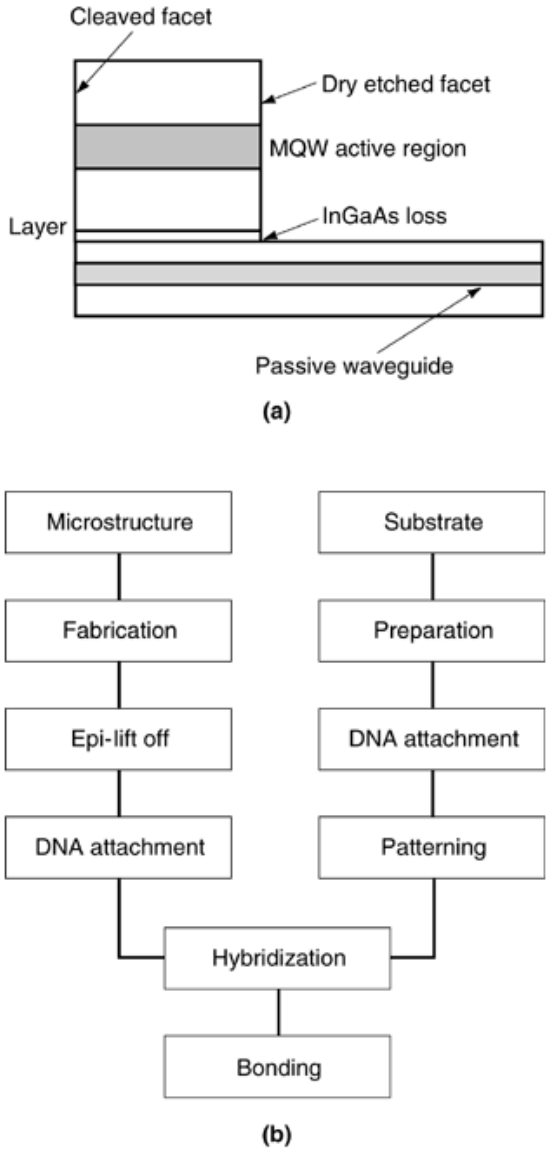

Fig. 65. (a) Twin wave guide structure. (b) DNA flow chart for microassembly.

The PIC is also progressing fast and is used for transmitters. It consists of lasers, semiconductor optical amplifiers (*SOAs*), optical waveguides, modulators, etc. The complex regrowth technique based on MBE is not well suited for such development. A twin-waveguide (*TG*) and an asymmetric twin-waveguide (*ATG*) structure have been developed, where a laser or SOA is defined in the active region by etching down into the cladding layer [Fig. 65(a)]. The ATG structure allows mode selection for SOA in a proper way. A promising application of ATG SOA technology is the Mach–Zehnder configuration of a terahertz optical asymmetric demultiplexer (*TOAD*).

The *p–i–n* FET technology is useful for moderate-speed applications (< 2 GHz) requiring large circuits. However, large-scale InP-based circuits with MODFETs or HBTs are promising for the future development of high-speed optoelectronic LSI. Optoelectronic very large-scale integration (*OE* VLSI) based on hybridization of silicon CMOS VLSI with GaAs/GaAlAs MQW modulators is also in progress. A batch-fabricated CMOS-based OE VLSI smart pixel shuttle has been demonstrated. The largest chips to date are 7 mm $\times$ 7 mm silicon chips with up to 4.5×10^5 CMOS gates and with a 64×68 array of modulators arranged in a 5.5 mm $\times$ 5.5 mm field. The modulator yield of such chips is 100%, corresponding to a device yield of 99.97%. The challenges for the future are to reduce the drive voltages for modulators for compatibility with CMOS and to improve the yield both in hybridizing MQW diodes and in manufacturing them. There must be continued scaling of interconnects for higher speed of I/O technology. In near future the new systems may be cost-competitive with all-electrical solutions.

Yet another milestone is DNA-assisted microassembly, explored recently. For OEICs, different types of hybrid integration technologies include flip-chip bonding, epitaxial liftoff and direct bonding, substrate removal and applique bonding, microrobotic pick and place, and self-assembly methods. DNA-assisted microassembly relies on self-assembly principles. It is based on the use of strong coulombic forces to bring complementary parts together. It utilizes the remarkable selectivity of DNA hybridization to pick and place large numbers of identical devices. One possible process flow for DNA-assisted fluidic microassembly of devices and substrates is shown in Fig. 65(b). DNA-assisted microassembly has the potential to have a major impact on microelectronic and optoelectronic industries by bringing together different materials and devices.

Acknowledgment

The author wishes to thank his research scholars Mr. George K. Abraham and Ms. Nandita Saha Roy for their untiring effort in the typing of the manuscript. Thanks are also due to Mr. Jai Sankar Singh, Mr. Pradeep Kumar Singh, Mr. Manoj Kumar Verma, and Mr. Ashit Raj for their help in the preparation of the manuscript. It is indeed a great pleasure to thank my wife Mrs. Arati Pal and my sons Bikramjit, Arijit, and Debjit for their understanding and cooperation. Thanks are also due to Dr. B. R. Singh, Central Electronics Engineering Research Institute, Pilani, India, and Prof. S. D. Mukherjee, Department of Physical Electronics, Norwegian University of Science and Technology, for their help with some of the support materials. Thanks are also due to various publishers who have kindly permitted me to use some of the materials, including figures, published in their books and journals.

BIBLIOGRAPHY

1. J. G. Simmons G. W. Taylor Theoretical studies of electronic conduction and optical generation mechanisms in the double-heterostructure optoelectronic switch, *IEEE Trans. Electron Devices*, **ED-35**: 1269–1278, 1988. J. G. Simmons R. S. Mand Characterization and application of digital optoelectronics switches (DOES), *Asia Pacific Eng. J. (Pt. A)*, pp. 59–80, 1991.
2. A. L. Leutine D. A. B. Miller L. M. F. Chirovsky Optimization of absorption in symmetric self electrooptic effect devices: A systems perspective, *IEEE. J. Quantum Electron.*, **QE-27**: 2431–2439, 1991.
3. S. A. Feld *et al.* Electrical and optical feedback in an InGaAs/InP light amplifying optical switch (LAOS), *IEEE Trans. Electron Devices*, **ED-38**: 2452–2459, 1991.

READING LIST

C. Baack G. Elze G. Wolf GaAs MESFET: A high speed optical detector, *Electron Lett.*, **13** (7): 193, 1977.
P. Bhattacharya *Semiconductor Optoelectronic Devices*, New Delhi: Prentice Hall of India, 1995.

P. Chakrabarti S. C. Choudhary B. B. Pal A new infra-red avalanche photodiode for long distance fiber optic communication, *Solid State Electron.*, **31**: 331–314, 1989.

P. Chakrabarti S. C. Choudhary B. B. Pal Noise characteristics of a superlattice avalanche photodiode, *Appl. Phys. A*, **48**: 331–334, 1989.

P. Chakrabarti B. B. Pal Effect of optical radiation in a photo-DOVATT, *Appl. Phys. A*, **42**: 311–315, 1987.

P. Chakrabarti B. B. Pal Optical characteristics of a superlattice avalanche photodiode, *Solid State Electron.* **30**: 675–679, 1987.

S. Y. Chou M. Y. Liu Nanoscale tera-hertz metal–semiconductor–metal photodetectors, *IEEE J. Quantum Electron.*, **QE-28**: 2358–2366, 1992.

A. A. A. De Salles Optical control of GaAs MESFETs, *IEEE Trans. Microw. Theory Tech.*, **MTT-31** (10): 812–820, 1983.

D. C. Dumka Photodetector and optoelectronic integrated circuit (OEIC) receivers using III–V compound semiconductor, Ph.D. Thesis, Banaras Hindu Univ., Varanasi, India, 1996.

J. Franz V. K. Jain *Optical Communication Systems*, New Delhi: Narosa, 1996.

U. Hilleringmann K. Goser Optoelectronic system integration on silicon: waveguides, photodetectors and VLSI CMOS circuits in one chip, *IEEE Trans. Electron Devices*, **42**: 841–846, 1995.

W. D. Hillis *The Connection Machine*, Cambridge, MA: The MIT Press, 1985.

A. Husain M. Fallahi (eds). *Heterogeneous Integration: Systems on a Chip, Critical Review 70* Bellingham, WA: SPIE Optical Engineering Press, 1998.

A. L. Leutine *et al.* Logic self electro-optic devices: Quantum well optoelectronic multipost logic gates, multiplexers, demultiplexers and shift registers, *IEEE J. Quantum Electron.*, **QE-28**: 1539–1552, 1992.

H. Matsueda AlGaAs OEIC transmitters, *IEEE J. Lightw. Technol.*, **LT-5**: 1382–1390, 1987.

D. A. B. Miller *et al.* The quantum well self-electrooptic effect device: Optoelectronic bistability and Oscillation and self-linearized modulation, *IEEE J. Quantum Electron.* **QE-21**: 1462–1475, 1985.

S. Mishra V. K. Singh B. B. Pal Effect of radiation and surface recombination on the characteristics of ion-implanted GaAs MESFET, *IEEE Trans. Electron Devices*, **37** (1): 2–10, 1990.

H. Mitra *et al.* Optical effect in InAlAs/InGaAs/InP MODFET, *IEEE Trans. Electron Devices*, **45**: 68–77, 1988.

J. A. Neff Major initiatives for optical computing, *Opt. Eng.*, **26**: 2–9, 1987.

M. J. O'Mahony Semiconductor laser optical amplifiers for use in future fiber systems, *IEEE J. Lightw. Technol.*, **6**: 531–544, 1988.

B. P. Pal (ed.) *Fundamentals of Fiber Optics in Telecommunication and Sensor Systems*, New Delhi: Wiley Eastern, 1992.

B. B. Pal H. Mitra D. P. Singh Enhanced optical effect in a high electron mobility transistor device, *Opt. Eng.*, **32**: 687–691, 1993.

B. B. Pal S. K. Roy Study of frequency response of multiplication gain of a two layer avalanche photodiode; *Proc. IEEE (Lett.)* **62**: 285–287, 1974.

B. B. Pal *et al.* Time dependent analysis of an ion-implanted GaAs OPFET, *IEEE Trans. Electron Devices*, **41**: 491–498, 1994.

S. D. Personick W. O. Flickenstein Communication switching—from operators to photonic, *Proc. IEEE*, **75**: 1380–1403, 1987.

A. F. Salem A. W. Smith K. F. Brennan Theoretical study of the effect of an AlGaAs double heterostructure on metal–semiconductor–metal photodetector performance, *IEEE Trans. Electron Devices*, **ED-41**: 1112–1119, 1994.

J. M. Senior *Optical Fiber Communications*, New Delhi: Prentice Hall of India, 1996.

A. Sharma A. K. Ghatak (eds.) *Photonic-98, Proc. Int. Conf. on Fiber Optics and Photonics*, New Delhi: Viva Books, 1998.

C.-X. Shi High performance undoped InP/$In_{53}Ga_{47}As$ MSM photodectors grown by LP-MOVPE, *IEEE Trans. Electron Devices*, **ED-39**: 1028–1031, 1992.

T. S. Siddeswarappa A new device model for optical feedback in GaAs OPFET light amplifying optical switch (LAOS) using SPICE model, M. Tech. Thesis, Banaras Hindu University, Varanasi, India, 1997.

J. G. Simmons G. W. Taylor Theory of electron conduction in the double heterostructure optoelectronic switch, *IEEE Trans. Electron Devices*, **ED-34**: 973–984, 1987.

R. Simons Microwave performance of an optically controlled AlGaAs/GaAs high electron mobility transistor and GaAs MESFET, *IEEE Trans. Microw. Theory Tech.*, **MTT-35**: 1444–1455, 1987.

B. R. Singh *et al.* Optoelectronic integrated circuit for photonic system, *JIETE (India)*, **38**: 147–162, 1993.

V. K. Singh S. N. Chattopadhyay B. B. Pal Optical controlled characteristics of ion-implanted Si MESFET, *Solid State Electron.* **29**: 707–711, 1986.

S. D. Smith Optical bistability, photonic logic, and optical computation, *Appl. Opt.*, **25**: 1550–1564, 1986.

S. R. Saxena R. B. Lohanl R. U. Khan B. B. Pal Generalized DC model of GaAs optical field effect transister considering ion-implanted profile, *Opt. Eng.*, **37**: 1343–1352, 1998.

A. Suzuki K. Kasahara M. Shikada InGaAsP/InP long wavelength optoelectronic intergrated circuits (OEICs) for high-speed optical fiber communication systems, *IEEE J. Lightw. Technol.* **5**: 1479–1487, 1987.

R. Syms J. Cozrens *Optical Guided Waves and Devices*, London: McGraw-Hill, 1992.

S. M. Sze *Physics of Semiconductor Devices*, New Delhi: Wiley Eastern, 1983.

W. T. Tsang Semiconductor semimetals, in *Light Wave Communication Technology, Vol. 22, Pt.D: Photodetectors*, New York: Academic Press, 1985.

P. Urquhart Review of rare earth doped fiber lasers and amplifiers, *IEE Proc. Pt. J*, **135**: 385–407, 1988.

L. Yang *et al.* High performance Fe:InP/InGaAs metal–semiconductor–metal photodetectors grown by metal organic vapour phase epitaxy, *IEEE Photon. Technol. Lett.*, **2**: 56–58, 1990.

Silicon-based optoelectronics, *IEEE J. Select. Topics Quantum Electron.*, **4**: Nov.–Dec. 1998.

B.B. PAL
Banaras Hindu University